WAVE ENERGY TRANSFORMATIONS IN A COMPLEX REEF ENVIRONMENT; OBSERVATIONS, MODELING AND APPLICATIONS

A THESIS SUBMITTED TO THE GRADUATE DIVISION OF THE
UNIVERSITY OF HAWAIʻI AT MĀNOA
IN PARTIAL FULFILLMENT
OF THE REQUIREMENTS
FOR THE DEGREE OF

MASTER OF SCIENCE

IN

OCEANOGRAPHY

MAY 2023

By
Camilla Tognacchini

Thesis Committee:

Douglas S. Luther, Chairperson
Justin E. Stopa
Philip R. Thompson

*I would like to dedicate my thesis work to the memory of my father, Daniele, who experienced Hawai*ʻ*i's waves in the 80s. I am most grateful to my family, my keiki Kamāli*ʻ*iokekai and Vanina, and my mom, Flavia.*

Mahalo nui to the many people involved in this research project.

Acknowledgements

It’s been wonderful to be part of the NOAA coastal resilience team; mahalo to Prof. Doug Luther, Melissa Iwamoto, Tara Owens, Fiona Langenberger, Martin Guiles, Assaf Azouri, Ning Li, Chip Young and Volker Roeber. Credit goes to the Coastal Hazards Group; Martin Guiles, Assaf Azouri and Ning Li for the modeling work. Thanks to our divers and boat captains. Thanks to the West Maui community for getting involved and the citizen scientists for collecting photos of runup. Thanks to the Ocean office and the CIMAR staff for the support. Thank you to my committee Prof. Doug Luther, Prof. Justin Stopa and Prof. Phil Thompson for the questions, comments and suggestions. A special thanks to my team: Doug, Martin and Assaf thank you for the learning experience and all the fun.

This research was supported under a Coastal Resilience Grant: NOAA-NOS-NRPO-2017-2005159, a University of Hawai‘i at Mānoa Sea Grant project: ‘West Maui Wave Runup Forecasts’, and by the University of Hawai‘i at Mānoa Cooperative Institute for Marine and Atmospheric Research (CIMAR).

Abstract

Wave-driven runup events are severely impacting West Maui's (WM) coastline with episodic inundation and chronic erosion. A combination of background sea level, tides and wave driven components, such as setup and infragravity (IG) wave energy, contribute to the level of runup experienced at the shore. The setup, swash and IG wave responses under different sea and swell forcing conditions are highly variable along the WM coastline, due to complex nearshore bathymetry. Simulating the setup, swash, and IG wave energy responses to large swell events at different locations along the WM coast is necessary for accurate calculation of runup, enabling forecasting of, and community preparation for, these coastal inundation events. The PacIOOS Coastal Hazards Group has implemented a two-dimensional, fully-nonlinear and weakly dispersive, phase resolving numerical wave model (Boussinesq Ocean and Surf Zone; Roeber and Cheung, 2012), using high resolution bathymetry and topography of WM. The model simulates the cross- and along-shore transformations of gravity and IG wave energy for simulation of runup.

The main objective of this study is to validate the model for the WM domain against observations of swell events. Nearshore sea level observations are derived from bottom water pressure records collected at different depths (1-13 meters) and locations along the West Maui coastline, from November 2018 - June 2020. Comparisons between *in situ* observations and co-located virtual stations within the model reveal a high degree of agreement in both the sea and swell and IG period bands, between 8 seconds and up to 10 minutes. Spectral analysis is used in the comparisons to investigate the spatial variability of the wave energy. A series of sensitivity tests using variable model resolutions shows that the choice of a 5 x 5 meter grid is optimal for this domain. Observations and model comparisons are discussed for both a North swell and a South swell event at six different locations along the WM coastline, including two relatively compact arrays. The simulation for the North swell is in better agreement with observations on the northern coast of WM (at Oneloa, Nāpili and Kahana). Similarly, the simulation for the South swell is in better agreement with observations in the southern area of WM (at Puamana and Olowalu). The comparisons reveal the high IG amplitude variability alongshore resulting from complicated IG wave patterns, which are generally well simulated in the model. At both arrays

the comparisons of coherence phase and amplitude of the observations and model reveal the model is simulating well the frequency-dependent, spatial variability of the nearshore wave-driven phenomena that contribute to runup. The few occasions where the simulation is unimpressive suggest that ways to improve the model methodology should be investigated.

Table of Contents

List of Tables

List of Figures

List of Abbreviations

1-D	One Dimensional
2-D	Two Dimensional
BOSZ	Boussinesq Ocean and Surf Zone
CHG	Coastal Hazards Group
Hs	Significant wave height
IG	Infragravity
LIDAR	Light Detection and Ranging
MSL	Mean sea level
NOAA	National Oceanic and Atmospheric Administration
PacIOOS	Pacific Island Ocean Observing System
PSD	Power Spectral Density
SS	Sea and Swell
SWAN	Simulating Waves Nearshore
Tp	Peak period
UH	University of Hawai‘i
WM	West Maui
WW3	WAVEWATCH III

Chapter 1. Introduction

1.1 Wave Runup in West Maui

Episodic coastal inundation events, driven by a combination of gravity wave-driven phenomena, high tides and longer period changes in background sea level, now have a larger impact on Hawaiian shores than tsunamis. These wave-driven events that elevate the shoreline water level are called ‘runup’ events.

Runup events impinging onto WM shores are severely impacting coral reefs, coastal erosion, coastal resources, infrastructure, freshwater aquifers, and the safety of coastal communities (e.g., Storlazzi et al., 2018 and Fiedler et al., 2020). In order for coastal communities to prepare for, and recover from, the increasing impacts of wave runup events, both (i) short-lead-time, spatially variable wave runup forecasts, and (ii) long-lead-time, high-resolution projections of runup amplitudes on top of future sea level rise, are needed. Spatially dependent modeling of the dynamical processes that contribute to wave runup in WM are expected to provide accurate near-term wave runup forecasts & long-term inundation projections. Using a 2-D model is a step forward from solely empirical and 1-D forecast methodologies (eg. Stockdon et al., 2006 and Merrifield et al., 2014).

WM geomorphology is characterized by a variability of fringing reef, sloping beaches, rocky and armored shoreline. The energy transformations of gravity waves breaking over the fringing reef, and mixed reef-slope environments create wave-driven phenomena such as swash, IG wave energy and setup (e.g., Figure 1.1). These processes are important contributors to the level of runup experienced at the shoreline (e.g., Guza and Thornton 1982; Oltman-Shay and Guza, 1985; Merrifield et al., 2014; Pomeroy et al., 2012; Cheriton et al., 2016).

The geography of the Maui Nui Island group (Maui, Molokai, Lanai and Kaho‘olawe islands, Figure 1.2), as well as the shallow bathymetry of the inter-island channels, determine the diffraction, refraction and focusing of swell energy into the WM shores. The northern end of the WM coastline is most impacted by waves originating from northern hemisphere winter storms (North swell) and northeast Tradewind waves (Figure 1.3). Swells from distant southern hemisphere winter storms impact WM from the south (South swell). Short period waves generated from very close Kona storms from the south or hurricanes are not considered here as the runup they produce is dependent on local atmospheric conditions (also not considered here) in addition to the swell.

The complex bathymetry also gives rise to the existence of short-period, alongshore IG modal structure near the shore (e.g., Figure 1.4), as well as longer-period IG modes involving multiple islands, that are known to be excited by tsunamis for instance (e.g., Figures 1.5 & 1.6 from Cheung et al., 2013).

1.2 Background on Nearshore Wave Energy Transformations

Waves from distant storms form groups as they travel across the ocean. The 'surf beat' phenomenon was first described by Munk (1949) and by Tucker (1950). Longuet-Higgins and Stewart (1962) demonstrated how waves that have different frequencies combine into groups. The amplitude-dependent nonlinear mass flux of the waves in the groups causes a depression in the mean sea level, and the resulting wave has a wavelength that corresponds to the short-wave energy envelope of the group. The waves force this bound wave through Stokes second-order interactions. A graphical representation for waves of two different frequencies combining to form a group of waves and the resulting bound wave, taken from Bertin et al. (2018), is shown in Figure 1.7.

As groups of waves shoal and break near the shore, the bound wave is released from the group as a lower frequency 'free' IG wave. The free waves reflect from the shore back out to sea (leaky waves) or can remain trapped along the coast (edge waves). Free edge waves can be progressive or standing; and can create periodic alongshore patterns and resonant oscillations (alongshore normal modes). Eckart (1951) showed a solution for edge waves leading to Laguerre polynomial structures in the cross shore, with highest amplitudes near the shore.

Additional IG wave generation mechanisms have been proposed. The bound wave generation mechanism is important on gently sloping beaches (Battjes et al., 2004). For beaches with steep slopes a time-varying break point mechanism of IG wave generation is important; where the difference in the location of the breakpoint between shorter and longer waves is balanced by wave set-up nearshore (Battjes et al., 2004). After wave breaking, bore on bore capture processes can generate IG wave energy, especially on gently sloping beaches with a wide surf zone (e.g., Bertin et al., 2018).

A seaward sloping bottom with no alongshore variability yields trapped and leaky edge wave modes (e.g., Guza and Thornton 1985). Depending on the characteristics of the forcing, equal amplitude trapped edge waves at the same frequency, but opposite alongshore wavenumbers, can form standing oscillations alongshore (e.g., Bertin et al., 2018) whose nodes/antinodes are not necessarily fixed in the alongshore direction; that is, each different wave forcing can set up a standing mode with nodes and antinodes at dissimilar alongshore locations. These trapped waves all tend to exhibit the characteristic Laguerre function cross shore mode structures found by Eckart (1951).

An offshore deviation in the bottom slope, such as a reef edge, creates a strong reflector that can engender a fixed, cross shore standing mode structure that may or may not dominate over the edge wave mode structure. Furthermore, alongshore variations in geography (e.g., bays and rocky headlands) and bathymetry (e.g., reef and channel systems) permit the establishment of alongshore modal structures whose nodes and antinodes are fixed in space for each frequency no matter what the nature of the forcing.

At long periods for IG waves (periods > 10 minutes), the IG waves depend greatly on the larger scales of variability (order a few km and more) of the geography and bathymetry of the local coast (for an isolated island) or on the interconnected geography/bathymetry of multiple islands or both. These long period coastal modes are known to resonate in response to tsunami forcing (e.g., Figs. 1.5 and 1.6; Cheung et al., 2013).

Modes are found at periods as short as 1-2 minutes. At these shorter periods, the numerical model simulations (Figure 1.4, Azouri et al., 2018) show that the IG structures nearshore, even shoreward of the breaking zone, are a combination of fixed geography/bathymetry mode structure along with a Laguerre function structure right at the shoreline (the latter having an antinode at the shore, and then a node very close offshore, plus often another identifiable antinode beyond that).

The periods of the generated IG waves depend on the beach profile and the characteristics of the incident short waves. IG waves are typically defined as having periods longer than 25 seconds (eg. Bertin et al., 2018, and others). Based on empirical perceptions of affinity groups among the IG waves in the observed frequency spectra (below). We chose the following cutoffs for the definitions of different period bands to be used for WM:

- SS - Sea/ Swell: 5 - 25 seconds
- Near IG: 25 - 250 seconds
  - Near IG-A: 25 - 62.5 seconds
  - Near IG-B: 62.5 - 125 seconds
  - Near IG-C: 25 - 250 seconds
- Far IG: 250 seconds - 90 minutes
  - Far IG-A: 250 - 600 seconds
  - Far IG-B: 600 seconds - 90 minutes
- Tidal Harmonics: 90 – 600 minutes

Free edge waves periodically elevate the sea level in bays, harbors, reefs, lagoons and around insular shelves. Many observations have been made of IG waves on sloping beaches, e.g., Oltman Shay and Guza, 1987; Okihiro et al., 1992; Elgar et al., 1992; and in reef environments, eg. Péquignet et al. 2009, Pomeroy et al., 2012; Merrifield et al., 2014; Azouri, 2016; Cheriton et al., 2016. The largest swells produce the largest amount of runup nearshore (e.g., Guza and Thornton, 1982; amongst others).

The radiation stress caused by the momentum flux of breaking waves (of different frequencies and amplitudes) increases the mean water level and is referred to as wave setup (Longuet-Higgins and Stewart 1962, Longuet-Higgins, 1964, Guza and Thornton 1981). The cross shore profile of wave setup has positive values at the reef flat and negative values (setdown) at the fore reef slope (Figure 1.1). Wave setup in reef environments elevates the nearshore water level during wave events which can increase the excitation of resonant coastal modes (Péquignet et al., 2009).

Other factors that influence nearshore wave energy, such as the effects of tides and background water levels on setup (e.g., Becker et al., 2014), as well the dynamics of the IG waves are topics for future research.

1.3 Research Objectives

This study's principal objectives are as follows:

(1) To validate with *in situ* observations the ability of an operational 2-D hydrodynamical model to simulate the frequency-dependent amplitudes and spatial variability of the nearshore wave-driven phenomena that contribute to runup (e.g., setup, bores/swash, and infragravity waves).

(2) To explore whether, where and when the model vs. data comparison is problematic.

(3) To describe the horizontal structures of the infragravity (IG) wave components of the wave-driven phenomena, because of their unfolding importance to runup along reef-protected coasts (e.g., Merrifield et al., 2014), drawing on the model output for insight, where possible.

In order to validate the model for WM we need nearshore estimates of the frequency-dependent wave energy from observations of sea level heights. The study focuses on a stretch of coastline between Pāpalaua Beach Park in the south and Honolua Bay in the north (Figure 1.2 shows locations of *in situ* gauges). The collected data are analyzed to characterize and quantify the wave-driven phenomena (e.g., setup, swash and infragravity waves) that contribute to wave runup as a function of incident SS energy and direction for different areas of WM. The goal is to compare the analysis of the observed data to a like-minded analysis of hindcast simulations from a 2-D numerical model developed and executed by the PacIOOS[1] Coastal Hazards Group (CHG).

Preliminary model runs were employed to plan the locations of instrument deployments in order to ensure the delineation of the wave energy variability. Deploying instruments in the surf zone was challenging due to the energetic shallow reef environment, sand movements, instrument battery life and COVID-19 travel restrictions (details are provided in section 2.1). Observations of sea level, currents and waves were successfully collected for many locations along the WM coast.

Data inspection, editing and analysis preparation methodologies are reviewed in Section 2.2. The analysis of the observations in section 2.3 focuses on characterizing the spatial

[1] PacIOOS (Pacific Islands Ocean Observing System; www.pacioos.org) is a part of the U.S. Integrated Ocean Observing System (IOOS®).

variability of the power spectral densities in different frequency bands under forcing by major wave events at two arrays: in Kahana and Puamana. Section 4.1 explores the impact of different model grid sizes on the similarity of modeled and observed SS and IG wave power spectral densities, resulting in a choice of model grid size for optimal simulation. Comparisons of model simulations and in situ observations for two major events are detailed in Section 4.2. The model fidelity is examined at five different locations, including the two arrays, for North and South swells.

Chapter 2. Sea Level Observations

2.1 The Field Program

Observations of bottom water pressure (as a proxy for sea level), currents and wave direction were collected from the coastline of WM. Instruments were placed in the nearshore at depths of 1- 14 m along a stretch of coastline spanning 32 km, from Ukumehame Beach Park to Oneloa Bay.

The field experiments started in November 2018 and took place over two winter and one summer seasons. Instruments were deployed during 5 different field trips (Table 2.1) on 5-9 November 2019 (called D1), January 28 - February 1 2019 (D2), February 23-24, 2019 (D3), June 12-18 2019 (D4) and on November 9, 2019 (D5). RBRsolo³ D pressure gauges were deployed at single point locations along the coast and in two arrays. The Kahana array (Figure 1.2) was instrumented throughout the D1-D4 deployment periods. The Puamana array (Figure 1.2) was in the water during the D2-D4 deployments.

The RBRsolo³ D is a compact logger which uses a piezoresistive pressure sensor with a specified accuracy within ±0.05% of the depth range. The clock drift is specified to be within ±60 seconds per year (RBR Instrument Guide, 2022). This study focuses on the bottom pressure observations collected with these sensors.

An Acoustic Wave And Current profiler (AWAC) was deployed at the offshore location (Kahana 5, Figure 1.2) of the Kahana array during the D1 deployment period and at the Puamana array (Puamana 56, Figure 1.2) for the D4 deployment period. Currents were also collected using single-point Aquadopp current meters at Kāʻanapali during the D1 deployment. The sparse current and wave direction data sets are not utilized in this study.

To minimize the disturbance to the reef environment of the instrumentation, we adopted a strategy of placing instruments away from live corals, in sand pockets or areas with coral rubble bottom. Deploying in the nearshore proved to be a challenge as in some locations sand moves seasonally and/or episodically, dislodging or burying the instrument packages. This led to improvements of the deployment packages over time. The instrument packages for the pressure gauge deployments D1 & D2 consisted of a modified sand anchor tube filled with cement at the bottom, with a pressure gauge secured in the tube, a fiberglass mesh to cover the top, vinyl tape to secure the top and a yellow marker rope. The tubes were screwed into the sand, stood vertically and were secured by a fiberglass grate (example in Figure 2.1). Upon recovery of the first and second rounds of deployments, some of the instrument packages were found in place, while some were dislodged and moved. For deployments D3-D5, the instrument packages were improved with the addition of a metal sponge to prevent biofouling, a marker buoy, zinc weights, and an anchor. For the weighted deployments, the sand anchor tube was laid horizontally on the fiberglass grate and secured to the bottom as a result of the attached weights. In some locations, an anchor was added (examples in Figures 2.2 and 2.3). The AWAC was mounted on a metal tripod and secured with an anchor, with a pressure gauge attached to one of the tripod legs. The current meters were laid horizontally and attached to a fiberglass grate held in place by a sand anchor tube, with a pressure gauge in it, screwed vertically into the sand.

Instruments at deeper sites were deployed and recovered by UH scientific divers, with the assistance of the research vessel Aloha Kai, operated by Ultimate Whale Watch & Snorkel. Instruments in nearshore locations, too shallow to reach by boat, were deployed and recovered by snorkeling with the assistance of stand-up paddleboard, kayak, surfboards and body boards.

The lengths of the records vary between 6 and 11 months. Thirty-five pressure records, 4 current records and 2 wave direction records were acquired during the time period between November 5, 2018 and June 7, 2020. Pressure gauge sensors were sampled continuously; D1 sensors were sampled at a frequency of 2 Hz, while D2, D3, D4 & D5 sensors were sampled at 1 Hz. Table 2.1 provides details on each pressure gauge deployment and Table 2.2 shows a timeline of all the data collected.

2.2 Data Preparation

Raw pressure measurements were subject to an editing process which consisted of visually inspecting the data for inconsistencies, trimming the data at the ends, and removing obvious outliers. All data analyses were done using the Python language, including scientific packages Numpy (Harris et al., 2020), Matplotlib (Hunter, 2007) and SciPy (Virtanen et al., 2020).

The atmospheric pressure signal is removed by averaging the air pressure from Kahului and Molokai airports (NWS, NOAA; https://www.weather.gov/). Sea level is derived from the pressure records via the hydrostatic relation, using a water density of 1023.4 kg/m^3 (average of CTD data from 10 meters depth for cruises # 307 & 309, from the Kahe point coastal station, data obtained via the Hawaiʻi Ocean Time-series HOT-DOGS application).

The resultant sea level records are analyzed using techniques of auto- and cross-spectra to generate power spectral density (PSD) and coherence plots; following methods described in Thomson and Emery (2014) and implemented in Azouri (2016). A 10% cosine-taper window is applied to each data segment before spectral analyses to reduce spectral leakage. The auto- and cross-spectra calculations are frequency band averaged, with 50% overlap of the averaging bands and with the number of spectral estimates in each average increasing with frequency. Due to the 50% overlap of frequency band averaging intervals every other spectral estimate is independent. The 95% confidence intervals for each independent spectral estimate are calculated following Thomson and Emery (2014), and for the coherence amplitude function following Thompson (1979); as described in Azouri (2016).

The spectra of sea level are corrected for the expected vertical decay of the gravity wave pressure signal under linear wave theory. The correction primarily affects the high frequency sea and swell band given the 1-14 m depths of our deployed pressure gauges (at 14 m depth, the correction is less than 10% at periods greater than 17 seconds).

The significant wave height (Hs) and peak period (Tp) are derived from the power spectral density (Coastal Engineering Manual, 2002). Both Hs and Tp are calculated hourly for the various period bands (SS, Near IG, Far IG).

The tidal and low frequency signals are removed from the sea level data by applying a Savitzky-Golay filter. Edited, tide removed, depth-corrected sea level data is equivalent to the numerical model's simulated output of sea level heights.

The SS and IG wave periods up to one hour are removed to look at the mean water level in the observations. The wave setup or setdown is calculated as the difference between nearshore and offshore mean sea level.

For the analysis of long period waves (> 10 minutes), a Butterworth filter is applied to the sea level data to remove the high frequencies.

The clock drift of the pressure gauges could not be checked upon recovery because all deployed sensors were recovered with dead batteries. This occurred because of the persistent and significant overestimation of the projected duration of battery life by the ‘Ruskin’ instrument programming software provided by RBR.

According to RBR, the clock drift is +/- 5 seconds per month. Since the absolute drift of each instrument is not available, the relative drift between gauges was calculated and the lag was corrected for each event. The relative drift was identified by estimating the phase offsets of the waves between instruments in an array during an event. This correction has only been applied to the data used in the coherence functions in section 4.2.

2.3 Sea Level Observations and Analyses

2.3.1 Wave Events

The variability of the SS forcing and IG responses along the coast are demonstrated by looking at different wave events that occurred during the study period (Figure 2.4 and Table 2.3). These wave events provide an appropriate sampling of events for which the observed and modeled wave-driven phenomena will be compared in Section 4.2.

The analyses focus on the locations of the arrays which are chosen to represent the north and south of WM. Located in the north of WM are Kahana 5 and Kahana 1, at 9 meters and 1 meter depths respectively. Kahana 1, as the most nearshore and shallowest sensor, provides the best example of the nearshore amplitudes of IG waves compared among the several IG frequency bands and compared with the SS. Kahana 1 has the largest IG wave responses, which often exceed the local SS wave amplitudes, indicating the importance of the contribution of IG waves to coastal wave-driven flooding. Puamana 56 is at 13 meters of depth, in the south of WM. The time period covers from boreal summer to winter, which includes swells coming from both the south and north, respectively.

The wave events with the largest significant SS heights are different for the locations of each array. The northern hemisphere winter storms produce the waves with the largest amplitudes at Kahana 5. Here, the largest four events (N2 - N5) with significant wave heights between 1 and 1.5 meters have a range of incident directions between 324° - 16° and peak periods between 16 and 18 seconds (Table 2.3). The largest Tradewind wave event (N6) from the NE has a peak period of 10 seconds and a Hs of 0.7 meters. The largest wave event from the south (S2) has a direction of 192°, and a significant wave height of 0.8 meters with peak period of 19 seconds.

The most energetic waves to reach Puamana are generated by southern hemisphere winter storms. The four largest wave events (S2 - S4) have incoming directions of 192°-196° and significant SS heights between 0.8 and 1 meter with peak periods of 18-19 seconds. The largest wave events from the north (N1 and N4) both have a max SS Hs of 0.6 meters (at Puamana 55 and 56, respectively; note: the February 10 N1 wave event is not included in the time series in Figure 2.4). The Tradewind wave event N6 is very small at Puamana 56 with Hs of 0.2 meters. Two-day periods of low wave activity (E1 - E4) with Hs below 0.2 meters for both Kahana and Puamana show the nearshore response when there is no swell.

The four major wave events from the south (S1 - S4) have similar Hs values at the two arrays, with a 10-25% reduction in max SS Hs at Kahana with respect to Puamana. This contrasts with the more energetic swells from the north (N2 - N5), which have a max Hs that is 60% larger at Kahana than at Puamana, likely a result of direction-dependent refraction within the interisland channels. The peak periods are longer for the wave events from the south (S1 – S4) compared to the wave events from the north (N2 - N5), at both locations, as is expected due to greater dispersion of the South swells traveling over much longer distances to reach Hawaiʻi from their storm origins.

The longer peak periods of the wave events from the South allow the waves to refract all the way into Kahana while retaining Hs values comparable to those at Puamana. The wave events from the North (N2 - N6) produce the largest significant wave heights at Kahana. In the open ocean (at the buoys) the N2 - N5 have larger Hs than the S1 - S4 events. However, due to their shorter periods the more energetic waves from the north don't refract as well into Puamana and produce lower SS Hs than the events from the south.

The Puamana array is most exposed to the S2 event and less affected by the N4 and N6 events. In general, the wave events from the south are the most energetic at Puamana 56 (S1 - S4 in Table 2.3).

2.3.2 IG Waves

The IG energy in the nearshore increases in response to wave events, regardless of the wave direction impinging on the coastline (Figure 2.4). For example, at Kahana 1, the Near and Far IG bands have high Hs in response to wave events from both the South (S1 - S4) and North (N2 - N6). The waves with the largest Hs offshore, at Kahana 5, produce the most IG wave energy nearshore, at Kahana 1 (Figure 2.4).

As the waves evolve over the shallow reef flat from Kahana 5 to Kahana 1, energy in the SS band is nonlinearly transferred to longer IG periods and to shorter period SS band harmonics via several processes (Section 1.2).

The SS Hs is highest at Kahana 5 (Figure 2.5), which is the most offshore gauge and located on the fore reef slope in the pre-breaking zone. Further inshore near the reef crest, at Kahana 3 (4 meters depth), the waves are breaking, and the SS Hs is reduced compared to offshore.

The SS Hs is less than half of the offshore amplitude at Kahana 9 (3 meters depth) and Kahana 1 (1.5 meters depth). At the two nearshore gauges the tide appears to modulate the SS energy (Figure 2.5).

The nearshore gauge at Kahana 1 has the highest IG PSD amongst the Kahana array sensors (not all are shown here). At this location on the reef flat, the PSD in the SS band is reduced by at least one order of magnitude compared to SS at the offshore location, for all the events.

During wave events (see curves S2, N4, N6 in Figure 2.6) at Kahana 5, the IG PSD increases in periods from 25 seconds up to 9 minutes. For example, the spectral peaks of PSD at 2 and 3 minutes are high during all the events. These peaks at 2 and 3 minutes are also present during weak SS forcing (E1), but with lower PSD values. This suggests these periods are resonant modes of the local bathymetry which are excited during SS events. The spectra for periods above 9 minutes are similar for all the two-day segments for Kahana 5 (Figure 2.6). These results suggest that the long period IG PSD is driven by something else than the swell, as noticed and explored by Azouri et al. (*in prep*). However, at the nearshore gauges, periods up to 120 minutes have elevated PSD during the largest wave events (for example N4 at Kahana 1, Figure 2.7).

The spectral width of the peak of the SS band seems to have an impact on the IG response. At Kahana 1 (Figure 2.7) the long period and narrow banded S2 has low spectral amplitude in the Near IG-A and higher values in longer IG wave periods, while the N4 and N6 events which are broad banded and shorter period have elevated PSD in the Near IG-A. Narrow banded and longer period south swells also have longer wavelengths, which generate longer IG waves with longer periods. In comparison, broad banded, shorter period swells produce shorter period IG harmonics. Azouri (2016) documented a similar dependence on SS PSD of IG PSD in several period bands at the coast of a Hawaiʻi fringing reef environment on Oʻahu that is similar to the northern coast of WM.

The S2 is the largest event for the Puamana array (Figure 2.8). The Puamana 56 and 54 gauges are located pre breaking, while 57, 61 and 62 are in the breaking zone for waves of this scale. The SS Hs during the peak of the swell is higher at the gauges in the breaking zone. The same locations also have high Near IG Hs values. The Far IG is very low (Hs < 0.1 meter), except at Puamana 61 where the Far IG Hs ramps up on July 16 and remains high for about two days.

The variance preserving spectra (Figure 2.9) from a two-day segment of data during the peak of the N4 event shows the IG band is very small compared to the SS band at Kahana 5. In the nearshore at Kahana 1 the SS band is much lower than the offshore, while the IG-A increases. Between 25 seconds - 10 minutes the variance preserving spectra is lower but on the same order as the SS spectra at Kahana 1. The periods above 10 minutes have much less energy than the periods between 25 seconds and 10 minutes. This shows that the periods longer than 10 minutes have small amplitudes and may not be significant contributors to the water level in the nearshore, compared to the shorter periods.

Spectral analyses over long periods of time (weeks) and coherence functions between distant stations (tens of kilometers) reveal the periods and structures of coastal modes at different locations around WM (Figure 2.10 & 2.11). The long period modes are found to be excited by the stronger gravity wave events, as well as tsunamis, but their near ubiquity in time suggests other undetermined energy sources. Some of the peaks in the observed PSD correspond well with the long period resonant coastal modes identified numerically by Munger and Cheung (2008) and Cheung et. al. (2013).

Within the Far IG-B band, a strong PSD peak near 60 minutes is present at stations located all around the WM coast as seen in the PSD plots (Figure 2.10). Another distinct peak at 50 minutes is present at Puamana, while at Kahana that period is energetic but with no distinct peak. At North Lahaina the PSD is not enhanced at the 50 minute period.

The one hour peak is coherent and in phase between Kahana and Puamana (Figure 2.11) as well as between Kahana and Kāʻanapali (also between Kāʻanapali and Lahaina not shown). These coherence plots show that the one hour mode has an antinode that stretches around the entire WM coast. Between Kahana and Puamana, oscillations at 50 minute periods are distinctly separate from the 60 minute oscillations due to their 180 degree phase change compared to no phase change at the 60 minute peak (Figure 2.11).

The 60 minute, in-phase peaks in the PSD along the WM coast are consistent with a mode structure shown in Cheung et al. (2013) for a 75 minute period band. The peaks around 50 minutes in our observations are a good fit with the 52 minute period band of Cheung et al., having high energy at the northern and southern ends of WM with a node at Lahaina. Other observed peaks suggest the existence of normal modes at additional frequencies. However, further analysis of IG periods above 10 minutes is not relevant to the current investigation as their contribution to the total sea level is small. Due to these results the model domains are set up for WM to simulate IG oscillations up to about 10 minutes (see section 3 below).

Chapter 3. Numerical Modeling of The Nearshore Gravity Wave Response

3.1. 2-D Modeling

The philosophy and methodology of the phase-resolving BOSZ numerical wave model (Boussinesq Ocean and Surf Zone; Roeber and Cheung, 2012) applied to WM in this research was described by Guiles et al. (2019) and Roeber et al. (2019), and is detailed in a forthcoming technical report (Roeber et al., 2022). This section provides a brief introduction to the model's general characteristics and the specific setup that is applied to WM. Comparisons of hindcast simulations with field observations (Section 4) provided improvements to the model's setup and demonstrate the level of accuracy of the model applied to the WM domain.

The complex geography (e.g., bays and rocky headlands) and bathymetry (e.g., reef and channel systems) around the WM coastline require two dimensional (2-D) numerical modeling to resolve the complexity of the nearshore gravity and IG wave responses to incident SS waves. Several appropriate phase-resolving wave models have been published, which can be applied in either 1-D or 2-D mode. A study by Azouri et al., (*in prep*) assesses the performance of three of these models in 2-D for simulating gravity and IG wave responses on the North Shore of Oʻahu, which has similar nearshore environments to WM. Of the models used in the study, the BOSZ wave model was selected for the WM domain due to its performance and extensive familiarity to the CHG researchers.

3.2 BOSZ Wave Model Characteristics

BOSZ is a hydrostatic, 2-D, fully nonlinear, weakly dispersive, phase-resolving numerical wave model. BOSZ uses a conservative form of the nonlinear shallow water equations derived from the Boussinesq-type momentum and continuity equations of Nwogu (1993) for modeling dispersive coastal wave processes. The use of conserved variables in the depth integrated Boussinesq equations, allows for a finite volume method to solve for the hydrostatic parts. The mass and momentum equations expressed with conserved variables satisfy the conservation laws across flow discontinuities, which approximates wave breaking. This method overcomes the Boussinesq equations' limitations in modeling wave breaking.

The resulting governing equations allow modeling of shock-related hydraulic processes, which describe waves transitioning over shallow reefs and are important for modeling of bores in shallow lagoons (Roeber & Cheung, 2012). The model's dynamic energy transformations in the surf zone have been validated both in laboratory experiments and with field data from the North Shore of Oʻahu (Roeber & Cheung, 2012).

3.3 BOSZ Model Set Up, Inputs and Limitations

The BOSZ model wavemaker radiates wave energy out from a line source along the offshore boundary of the computational domain. The wavemaker can produce waves that have different energy levels and propagation directions as a function of distance along the wavemaker. Sponge layers at the ocean boundary absorb outgoing wave energy. To cover the WM coastline, we are using two overlapping rectangular domains (Figure 3.1). Both domains have a wavemaker along the main offshore boundary. As well, the utility of side wave makers was tested.

The goal is to realistically model wave conditions that are comparable to field observations from WM. Starting with satellite observations, a series of spectral numerical wind and wave models (GFS; *Environmental Modeling Center*, 2003, WRF; Skamarock et al., 2008, WW3; Tolman, 2014, and SWAN; Booij *et al.*, 1999) result in high resolution, spatially variable, hourly frequency-wavenumber energy spectra as the input to BOSZ. Figure 3.2 details the modeling hierarchy, the direction of information exchange and the grid resolutions for each model.

Spectral wave models like SWAN have a limited ability to model the diffraction into the inter-island channels of the Maui Nui Island group. The quality of the SWAN output near the WM coast improves by including a higher resolution SWAN hindcast (provided by Ning Li of the CHG), which has a 200 x 200 meter grid versus the 500 x 500 meter grid of the SWAN Maui Nui Regional hindcasts that are routinely available from PacIOOS. Because we are using a hindcast of a SWAN forecast of the wave conditions, the timing, amplitudes, periods and directions of the modeled swell components may be inexact compared to the actual conditions.

The spatially variable directional wave spectra from the high-resolution SWAN at 42 virtual gauges (yellow circles in Figure 3.1 along the 40 meter depth contour of each of the BOSZ domains) are used in the BOSZ wavemaker. To avoid the growth of errors due to phase speed inaccuracies of short waves in Boussinesq wave propagation formulations, it is common to truncate the input wave spectrum to eliminate short period waves from the wavemaker, where the cutoff period depends on the depth at the wavemaker (e.g., Roeber et al., 2019). In our case, waves with periods shorter than 7 seconds are excluded from the wavemaker.

The bathymetry and topography are from a USACE 2013 Lidar survey (OCM Partners, 2022) that has been gridded to a 5 x 5 meter resolution. Currently, the model wavemaker requires a constant depth at the grid cells in which it operates. This depth has been set to 40 meters. This requirement has known limitations and could introduce some artificial features in the wave propagation. This has been addressed by the CHG model development team.

The necessary 'background' water level input to BOSZ is from the Kahului Harbor tide gauge (NOAA Tides and Currents, Kahului Harbor HI). The level employed in each experimental simulation is either the water level at the time of the event or the maximum level of the day.

To account for the bottom shear stress in BOSZ we chose a Manning roughness coefficient ($n = 0.035$) appropriate for this type of reef/land environment (Bretschneider et al., 1986). This coefficient was tested on the North Shore (Azouri 2016) and has been utilized in several similar environments (e.g., Roeber and Bricker, 2015). Sensitivity tests of varying Manning coefficients for areas in WM that have different bathymetric features are needed and will be done in the near future.

As grid spacing decreases (thus increasing spatial resolution) the computational expense increases. To determine how model fidelity varies with spatial resolution, and to find a balance between the appropriate spatial resolution and computational time, a set of grid sizes were tested (see Table 4.1). As a result of this testing (Section 4.1), the research version of the model is set up with 5 x 5 meter grid spacing. The model is run for a duration of 140 minutes, which includes a 20 minute spin up time. The two-hour duration of the simulation after spin up allows a wave field to develop with good statistical reliability for periods up to 10 minutes. At each grid cell, at every second, the model computes the free surface elevation along with the u and v velocities.

The size of the domain limits the longest period IG oscillations that can be expected to be simulated well. For example, Cheung et al. (2013) show that an IG mode at 12.5 minutes (Figure 1.6) has an alongshore wavelength along WM that approximately equals the individual WM domain sizes. At longer periods, the modes have larger alongshore scales (Figure 1.5). Therefore, due to the size of the domains, the runtime of the simulations and the frequency cutoff of the wavemakers, the model should be able to accurately simulate waves with periods up to 10 minutes.

How the model represents the observed conditions can only be as good as the quality of the inputs. The bathymetry and topography datasets are ten years old and should be updated to reflect any changes in the coastline, for example sand movements and erosion.

With the model's abilities and limitations in mind, we can assess its performance with this particular setup for WM. In section 4 we compare model simulations of sea surface elevation to observations of sea level collected from the field.

Chapter 4. Model Validation with Observations from West Maui

The objectives of the comparisons between observations and model are to assess the performance of the model at the locations where we have collected observations, by identifying where the model reproduces the energetics correctly and where it doesn't. We use this information to provide guidance for the implementation of the model in our research and practical applications. With confidence in the performance of the model we can explore the spatial variability of the wave energetics beyond the single point observation sites.

The CHG computed simulations of selected wave events (listed in table 4.1). In order to assess the model's performance we compare observed sea surface heights to modeled sea surface heights from various depths, between 1-13 meters, along the WM coastline. Auto-spectra and cross-spectra methods are applied to both modeled and observed data sets to analyze the structure of the wave energy in frequency space.

The model simulates wave breaking and other nonlinear energy transfer of wave energy to higher and lower frequencies. The scales of the 2 domains should allow for the simulation of IG energy of periods up to 10 minutes. The wavemaker's high frequency cutoff is at a cycle per 7 seconds and doesn't take into account any higher frequency wave energy. Any simulated energy at periods below 7 seconds is due to nonlinear transfer of wave energy. Based on the modeling capabilities, we are analyzing the wave energy for periods between 5 seconds and 10 minutes in the following comparisons.

The appropriate model grid size setup to provide good accuracy for simulating the observations is fine-tuned through a series of sensitivity tests. We ran the simulations under the same wave forcing conditions while changing the grid sizes to see how well the model performs at different resolutions. As well, two different tidal heights are explored in the first set of comparisons. The finer the grid size resolution, the more computational resources are required as the number of cells in the domain increases. We use these results to find good compromises between grid size resolution and computational requirements for both research and application purposes.

We settle on the 5x5 meter grid to compare with our observations as our research model. The research model is evaluated at different locations along the coast of WM, at various depths and for both North and South incoming wave directions. With knowledge of our model's abilities and limitations, we can apply it to learn more about the spatial variability of SS and IG wave energy along the WM coastline.

4.1 Model Grid Size Sensitivity Tests

The main goal of the model sensitivity tests is to investigate the simulation accuracy for different model grid spacings. In addition, we test the impact of using the proper tide height on the accuracy of the simulations. We initially evaluate the different grid spacings by visually inspecting the auto-spectra and qualitatively determining how well they agree for different period bands: SS, Near IG-A, Near IG-B, Near IG-C and Far IG-A.

The input wave energy used for these experiments are of a North swell on January 9, 2019 (runs # 1-5, Table 4.1), which had the largest Hs out of the swells recorded during three winter months of the first set of deployments. Model runs #1-5 are done using v1 of the model, without the use of side wavemakers. The model domain 1 (northern domain) is run for a two hour simulation of sea level. Model runs 1 & 3 are run at the maximum tide for that day (h = 0.44 m.), while runs 2, 4, & 5 are run with the actual tide, which was near mean sea level (h = -0.03 m.), details in table 4.1. The comparisons focus on four variations of the modeling grid sizes: 8x12, 10x10, 5x5 and 3x3 meters (cross shore x along shore).

Two examples from representative locations are chosen to identify appropriate model settings. Pressure gauges deployed at Kahana were the most exposed, out of all the available deployments, to the North swell event of January 9, 2019. Observations from Kahana 8, at 4 meters of depth, indicate this gauge is located in the breaking zone, where there is nonlinear transfer of energy in the SS band to longer and shorter period motions. Kahana 11 is located post wave breaking at 3 meters of depth, where the SS energy has dissipated somewhat and has been transferred to higher frequency harmonics as well as longer period IG motions. The two sites located at different depths highlight the differences in the energetics due to wave breaking processes. In Figure 4.1, comparisons of changing tide levels and grid sizes are shown with

Kahana 8 on the left side and Kahana 11 on the right side for the event on January 9, 2019, at 23:00 UTC.

4.1.1 8x12 Meter Grid - High Tide

We start with model run 1, in Table 4.1 with 8 x 12 meter grid spaces, run with the highest tide measured that day. The auto-spectra comparison between the simulation and observations at Kahana 8, in panel a, show the model is overestimating both the peak period and spectral amplitude in the longer SS band periods above 20 seconds. At the same time the shorter period harmonics below 7 seconds are underestimated. It is clear in the auto-spectra comparison from Kahana 11, in panel b, that the model has higher PSD in the SS band. The observations for Kahana 11 reveal the SS PSD is no longer a peak in the spectra by the time it reaches the nearshore site. At both sites the PSD for the Near IG-A, B and C period bands is relatively similar with some frequency disagreement between peaks and troughs.

The comparisons fall apart in the far IG-A period band, with the model not able to simulate these long periods at this grid resolution. The grid resolution may be too coarse to accurately distribute energy via nonlinear transfer in the breaking zone. We see this impact at both the lower frequency sub-harmonics and higher frequency harmonics, which are both in general disagreement.

4.1.2 10x10 Meter Grid - Actual Water Level

Using a 10x10 meter grid and the water level at the time of the swell (run # 2, Table 4.1) we still see there is excess PSD in the modeled SS band both in the breaking and post breaking zones in panels c & d respectively. Some of the excess SS PSD, at periods higher than 10 seconds, at Kahana 11 (panel d) is likely due to the coarser grid size not allowing enough grid space from the breaking zone to the nearshore for the nonlinear energy transfers to be fully developed. Even in the breaking zone, this model run at Kahana 8 in panel c underestimates the PSD at periods below 10 seconds, notably worse than in the 8x12 meter grid in panel a, which is consistent with the idea that the longer (10 m) grid spacing in the cross shore than the 8 meter cross shore grid spacing results in less energy transfer out of the SS band in this 2 hour simulation.

4.1.3 5x5 Meter Grid - High Tide

The 5x5 meter grid (run # 3, Table 4.1) does a better job of simulating the PSD in the SS band in panels e & f, when compared to the 8x12 meter grid. There is improvement in the agreement in the SS band both for the overestimate of the peak PSD seen in the 8x12 simulation, and the nonlinear energy transfer to higher frequencies. The agreement in the Near IG-A and the Far IG-A is also improved. This result suggests that the grid size resolution is directly responsible for the improved model performance. However, at Kahana 11 the agreement in the SS band has not improved much over the 8x12 meter grid. The amount of SS energy that reaches the nearshore has been found to be modulated by the tide, leading to the suspicion that the excess PSD in the SS band in panel f is due to the simulation using the high tide value of the day rather than the actual tide during the peak energy of the swell, which was at mean sea level.

4.1.4 5x5 Meter Grid - Actual Water Level

The 5x5 simulation (run # 4, Table 4.1) with the actual water level matching the time of the highest SS Hs in panels g & h can be directly compared to the 5x5 meter run with high tide as the water level in panels e & f. The first thing that we notice is the reduction in SS band energetics when using the actual water level. This confirms that for the Kahana 11 location the sea level modulates the amount of SS energy that reaches the post-breaking zone. As well, there is improvement in the longer periods of the SS band at Kahana 8, in the breaking zone, with more energy transferred away from the SS band than in previous simulations with the high tide. There is also better agreement in the SS PSD between 8 -15 seconds.

The comparisons for the 5x5 actual water level simulations (run # 4) show higher level of agreement than the previous run #'s 1-3 at all IG bands out to 10 minutes with the general PSD levels and structure in frequency space of the IG spectra being well replicated at both nearshore sites. The excess model PSD in the SS band periods above 20 seconds has decreased but is still present.

4.1.5 3x3 Meter Grid - Actual Water Level

To test whether even smaller grid size would improve simulation accuracy, even though the underlying bathymetry is available only at a 5 meter resolution, we ran a 3x3 meter grid (run

5, table 4.1). The comparisons between model and observations produced similar agreement to the 5x5 meter grid at both sites (panels i & j). This grid size does not replicate the impacts of small-scale features like coral heads and reef channels due to the limitation on the resolution of the bathymetry. However, having more grid cells in the breaking zone is allowing the model to redistribute energy more realistically to the shortest wave periods (<8 seconds). Figure 4.2 reveals the agreement for the modeled mean PSD values improves in the SS and Far IG-A bands but is worse for the Near IG-A, B and C periods, when comparing the 3x3 meter grid to the 5x5 meter grid.

4.1.6 Choice of Grid Size for Research Model

The 8x12 and 10x10 grids can be run in real time, for example for wave forecasting. However, the nonlinear energy transfer in the breaking zone is not as well resolved as in the higher resolution grids. The 5x5 grid offers high resolution and two days running time, which is within our modeling capabilities. The 3x3 grid spacing resolution is not practical, with a computation time of over 1 week, which is too long for the amount of modeling work planned. The best compromise for our research purposes is the 5x5 grid size which runs in a reasonable time at high enough resolution to redistribute SS energy to shorter and longer period motions in the nearshore.

The results of the tests reveal the model is sensitive to both changing grid size and changing water levels. The model simulates energy transfer to higher SS harmonics of periods as short as 7 seconds in the nearshore when it has a grid cell spacing of no more than 5x5 meters. Similarly, energy transfer to IG waves of periods up to 10 minutes is better resolved with the 5x5 meter grid than with the coarser grids. The comparison of the 5x5 meter grids with high sea level vs. the actual sea level reveal the modeled energy transformations are sensitive to changing the tidal water level in the nearshore. The comparisons show the model correctly simulates the modulation of energy by the tide in the post breaking zone in Kahana as seen in the observations. The results confirm IG oscillations with periods up to 10 minutes can be simulated with the 5x5 model. We can now apply the research model for two different wave directions in the different coastal environments of the two computational domains along WM.

4.2 Research Model Simulations and Comparisons with Observations

Two of the most energetic wave events for the north and south directions, N4 and S2, which also had the most distributed observational data coverage, were chosen to be modeled. Model runs were computed for both domains 1 and 2, on the 5x5 grid for the S2 event (runs # 6.1-6.5, Table 4.1), and for the N4 event (runs # 7.1-7.5, Table 4.1). Model version 2 (v2) with side wavemakers is applied to these simulations. The N4 event had an average Hs of 2.7 meters at the PacIOOS Pauwela Wave Buoy north of Kahului Hbr, while the S2 had an average Hs of 1.4 meters at the PacIOOS Lānaʻi Southwest Wave Buoy, during the event. For each event the model is run for five simulations lasting two hours each, without including a 20 minute spin up time. The variability in the SS period band as a function of distance along the WM coastline can be seen in Figures 4.3 and 4.4, with distinct energy fingers refracting into domains 1 and 2, respectively. We compare the modeled spectral estimates at the locations where we have observations available. In addition, the high resolution modeling allows us to explore the spatial variability in maps of band averaged power spectral density for different period bands of the full model output of the N4 event for domain 1, and of the S2 event for domain 2.

4.2.1 Oneloa Bay

The spectra of the observations and model for the S2 event in Figure 4.5 reveals the PSD in the SS period band, peaking at 18 seconds, has a much broader and energetic spectral peak in the model. This results in the model having higher PSD values in the Near IG-A and B bands as well.

At Oneloa the modeling for the N4 event is more accurate; with the modeled PSD for the SS, Near IG-A and B in excellent agreement with the observations. The modeled PSD in the Near IG-C and Far IG-A periods is lower than the observations for both events.

The spectral amplitudes in the Near IG-C and Far IG-A bands, with a peak around 250 seconds, are well replicated by the model for both events. These periods are excited by both swell events, suggesting this is a resonant mode of the bay.

4.2.2 Nāpili Bay

The sensor at Nāpili Bay 2, located at 3 meters of depth in between the rocks of a reef flat, is near the breaking zone. The spectra of the observations in Figure 4.6 for the N4 event, show high PSD peaking in the Near IG-B period band. The spectra are in excellent agreement between model and observations for all period bands except for the Near IG-A period band, which is higher in the model.

4.2.3 Kahana Array

The black curves in Figure 4.7 show the spectra of the observations from the Kahana array for the S2 event (left side) and N4 event (right side). The modeling for the south swell has higher PSD values in the SS period band at the most offshore locations at Kahana 3 and 5. The Near IG-A & B bands also have higher PSD across the rest of the array. The short period harmonics of the SS band are replicated throughout the surf zone. The simulations for the N4 event reveal there is higher PSD in the SS period band with a broader spectral peak than in the observations at Kahana 5, panel b.

Both simulations match the character of the observations for the SS period band PSD at the nearshore sites. As an example, during the S2 event Kahana 11 sees peaks in the spectra around 16 and 8 seconds while the N4 event has no distinct peaks across the whole SS band for the observations or the simulation.

Swells with opposite incoming directions display very different nearshore dynamics at Kahana. The nearshore gauges Kahana 11 and 1 are located 140 meters apart, but not exactly on a line perpendicular to shore. The cross shore array, from Kahana 11 to 1, is located post wave breaking and very close to shore from a depth of 3 meters to 1.5 meters (map in Figure 4.8).

For the N4 event the modeled maps (Figure 4.9) show most of the SS energy is filtered by the shallow reef, resulting in almost none of the SS PSD being admitted past the 2 meter contour towards the shore. The gauges are at an across shore orientation with respect to the incoming north swell which can be seen in the negative phase wrapping in the SS band, which is indicative of propagation of waves between the two stations (Figure 4.8).

The waves from the south refract at an oblique incident angle with respect to the cross shore array, which can be seen in the signature of the constant phase corresponding to the peak of the SS band in Figure 4.8. For this event the high coherence amplitude in the Near IG-A band is associated with positive phase wrapping, which is in the opposite direction when compared to the north swell. In the Near IG-B band there is high coherence with a corresponding 180 degree phase jump indicating modal structures.

During the north swell the IG periods are highly coherent with negative phase wrapping across the Near IG-A, B and C bands; a likely explanation for this is the cross shore propagation of IG waves. The coherence drops significantly in the Near IG-C, this drop in coherence is not fully replicated by the model. The model sees a statistically significant drop in coherence in the Near IG-B instead. Kahana 1 is located where the nearshore Near IG-C PSD is high, while Kahana 11 is located in a node for these periods, which is consistent with the drop in coherence (Figure 4.8).

The setup has the largest values during the N4 event, reaching an average of 8 cm on the reef flat at Kahana 1 (Figures 4.10 & 4.11). The model shows the setup is variable along shore (Figures 4.10 & 4.11). The deeper gauges at Kahana 5 and 3 are located in the area of setdown with negative values close to zero. The comparison between modeled and observed setup is excellent with both matching the cross shore setup profile (Section 1.2).

4.2.4 Kāʻanapali Point

The Kāʻanapali 2 deployment is located near the midpoint of the WM coastline, at 11 meters of depth. The auto-spectra in Figure 4.12 show the contrast between the S2 and the N4 events, in panels a and b respectively. The S2 event, although smaller in amplitude at the offshore buoys, refracts higher energy to this location relative to the N4 event. The character of the two swells is evident in the comparisons; with the model propagating energy at a longer peak period of 18 seconds for the S2 event, and a broader SS band and a peak period of 16 seconds for the N4 swell. The model is refracting both swell energies into this area of domain 1 consistent with the observations. In both cases the spectra of the SS energy is higher at periods of 18 - 25 seconds, consistent with all previous comparisons. The IG PSD at this offshore location doesn't show any peaks. The Far IG PSD in the modeling is much lower than the observation for periods over 250 seconds for both swell simulations.

4.2.5 Puamana Array

The model has higher PSD in the SS band at periods over 20 seconds, as compared to the observations for the S2 event. This can be seen for the four gauges in the auto-spectra comparisons for the S2 event (Figure 4.13). The Near IG bands are also generally somewhat higher in the model, while the Far IG-A is lower with respect to the observations.

The model refracts the N4 event to the Puamana array with good agreement in spectral shape of the SS band but with lower PSD in the peak, as shown in the comparisons with the observations in Figure 4.13 f, h, and j. The PSD in the modeled Near IG-B band does not match the observations and the agreement gets worse at longer periods. Overall, the model is not replicating the amount of observed energy at this location for the N4 event.

The cross shore array at Puamana (Puamana 54 at 5 meters and Puamana 52 at 2 meters depth, separated by a distance of 100 meters) is right in the breaking zone where the modeled South swell shows the highest SS PSD (Figure 4.14). Figure 4.15 (top two panels) reveal high amplitude coherence and phase wrapping in the SS band, which shows waves are propagating between the two sites. The three different coherent peaks in the Near IG-A with corresponding constant phases are indicative of the across shore IG standing wave pattern. At Near IG-B periods and longer there is high amplitude coherence and the two stations are in phase.

The gauges at Puamana 57 & 61 display constant phase in the SS band (bottom two panels, Figure 4.15), as they are positioned along the 4 meter contour. The coherent peaks, with various phase relationships, reveal IG wave structures with high variability between the two gauges in the Near IG-A band. The stations are coherent and in phase at longer IG periods. Figure 4.14, panels b-e, shows the IG PSD is confined to depths up to 5 meters near the shore, with the longshore array located close to regions of high PSD for all the IG period bands.

The sensors at Puamana 56 and 52 are located in the setdown for the model run (Figure 4.16). In Figure 4.17 both model and observations show Puamana 52 is located in the setdown. Based on the modeled maps the region of highest setup in the model is between the breaking zone and shore and none of our gauges are located in the setup zone for this event.

4.2.6 Olowalu

The pressure gauge at Olowalu is located at 2 meter depth where the SS PSD in Figure 4.18 peaks at 18 seconds and has distinct peaks at shorter period harmonics, near 8 and 6 seconds. The SS PSD is overall higher in the model, and so is the Near IG-A & B PSD. The PSD in the Near IG-C and Far IG-A bands is closer to the observations. The model replicates the shape of the observed spectra in frequency space but has higher PSD in the SS, Near IG-A & B bands.

4.2.7 Discussion of model validation

The comparisons at six different locations along the WM coast demonstrate the model is reasonably well simulating the dynamics in different wave regimes and in different reef environments. The model does a much better job at replicating PSD levels in the observations for the N4 compared to the S2 event. The model is in better agreement with the observations in the north of WM at Oneloa, Nāpili and Kahana for the N4 event; and in the south of WM at Puamana and Olowalu for the S2 event.

The best agreement between model and observations is for the N4 event at Oneloa and Nāpili (Figure 4.19). At both Kahana and Kāʻanapali the modeled energy for the N4 event in the SS band is higher than the observations. The highest disagreement is for the N4 swell at Puamana and Oneloa (there is no data for this event from Nāpili), where the SS band is almost as energetic as the observations but the IG periods are not showing the same PSD levels.

The modeling for the S2 event has higher PSD in the SS band, which results in elevated PSD in the IG bands. The longer period of the SS forcing in the model compared to the observations at most gauges indicates the source of higher energy is from the SWAN input spectra. More model runs with different input spectra are needed to test the sensitivity of the model.

The model reaches its limit in the Far IG-A period band, which is well replicated only at Nāpili 2 and Kahana 5. The model does not have enough PSD in the Far IG-A for the other locations as compared to observations (Puamana, Oneloa, Kāʻanapali, Kahana 1, 3, 9 and 11).

The two swells (S2 and N4) produce distinct IG responses in the nearshore at Kahana. The modeled coherences reveal remarkable agreement with the observations for both the N4 and

S2 events at Kahana, indicating the model is correctly replicating the nearshore wave energy transformations at different depths for opposite incident swell directions. The two cross shore arrays show the signature of both propagating and standing waves in the IG wave periods.

The cross shore standing wave pattern of IG waves can be seen in the modeled maps for both arrays. The spatial scale of the IG features increases with period, consistent with IG wave theory (e.g., Guza and Thornton, 1985; Azouri 2016). However, the two locations have very different IG wave responses which largely depend on the local bathymetry.

At Kahana the IG wave periods display complex patterns of PSD across the reef flat which extend from the shore and out to 10 meter depths. There is a high level of variability in the distribution of setup and IG energy along shore, which requires 2D bathymetry and would not be fully resolved by using 1D models.

At Puamana the IG energy is confined to the breaking zone with regular along shore patterns of highs and lows. Here both the IG energy and the setup are confined much closer to shore (< 5 meter depths). The gently sloping offshore bathymetry has an IG wave response with distinct cross shore standing wave patterns. In comparison to the complex IG energy patterns seen at Kahana, the more regular patterns of IG waves at Puamana are similar to IG waves seen for example in studies at Duck beach NC, which have uniform along shore bathymetry (Sheremet et al., 2001).

The differences in the nearshore responses to swell events observed between the two arrays are both due to the features of the bathymetry and the characteristics of the swell, which require additional model runs of different wave events to tease out.

Chapter 5. Conclusions

The observational sea level data sets acquired under the field program capture the seasonal variability of the nearshore wave energy for many different areas along the WM coast. The comparisons between model and observations prove to be vital in providing the information necessary for the correct implementation of the model for the two WM domains. The model is evaluated for two swell events at six different locations along WM, including two arrays.

Long period (10 - 60 minutes) coastal modes influence the sea level variability along the coast; but they do not appear to be significant components of runup variability (on the order of 1-2 cm). Modeling these periods is beyond the current capabilities. A larger model domain encompassing the entire Maui Nui Island group could be applied to simulate the variability of these periods driven by wave events. Such a large domain executed at the necessary spatial resolution will require one or two orders of magnitude speed enhancement of the numerical code, a task currently underway in CHG.

The model is able to reproduce nearshore wave energy in periods between 7 seconds and 10 minutes. Experimenting with grid sizes allowed us to find a grid size that produces results which compare well with the observations, while not being too computationally expensive. Some of the simulations are in remarkable agreement with the observations; for example, the swell from the north (N4) at Oneloa and Nāpili. The simulation for the South swell event (S2) however needs to be improved by refining the input spectra to BOSZ.

Direction, period and amplitude of the waves determine how much wave energy reaches a specific location along the coast. The spectral shape of the swell impacts which IG waves exist nearshore. The largest IG energy occurs in response to the largest wave forcing. Resonant modes of the local bathymetry can be excited by swells from different incident directions, as seen in various locations for the North and South swell events. Periods of low SS forcing reveal the resonant modes which are excited during wave events. During strong SS forcing the nearshore IG bands are filled with energy at periods up to 120 minutes.

Distinct along shore edge wave patterns dominate in places like Puamana, Olowalu and Kāʻanapali, which have gently sloping offshore bathymetry as well as relatively uniform alongshore bathymetry and a straight coastline, in comparison to the northern coast of WM. In the northern area of WM the complex alongshore bathymetry with many small bays and shallow reef flats supports resonant IG features. At Oneloa, Nāpili and Kahana the edge wave pattern is complicated by resonant IG modes, which results in a lot of alongshore variability in swash, IG energy and setup.

Supported by the rich spatial variability of the long time series of observations this model methodology can be used to advance the scientific understanding of the phenomena that contribute to wave runup. In collaboration with the PacIOOS CHG the model is employed in operational near-term (6-day) forecasts of wave runup as well as long term projections of wave-driven flooding under changing sea level conditions in twelve separate regions along WM's coastline.

Links to forecast products:

Wave Run-Up Forecast: West Maui, Hawai'i | PacIOOS

West Maui Wave-Driven Flooding With Sea Level Rise | PacIOOS

Table 2.1 Pressure Gauge Deployments

Columns from left to right: site name; deployment ID; latitude (DD); longitude (DD); deployment depth (meters); data start date (yyyy-mm-dd); data end date (yyyy-mm-dd); sampling frequency (Hz).

Site Name	Deployment ID	Latitude (DD)	Longitude (DD)	Depth (m)	Start Date	End Date	Sample Rate (Hz)
Oneloa Bay 01	ON-01-D4	21.005281	-156.661331	8	2019-06-18	2020-05-04	1
Nāpili Bay 02	NB-02-D5	20.994730°	-156.669040°	3.8	2019-11-09	2020-06-07	1
Kahana 01	KH-01-D3	20.9792	-156.6765	1.5	2019-02-24	2019-06-12	1
Kahana 01 Chain	KH-01-D4-C	20.97679	-156.67865	1	2019-06-17	2020-01-06	1
Kahana 02	KH-02-D1	20.97963	-156.67661	2	2018-11-08	2019-01-21	2
Kanana 03	KH-03-D4	20.981189	-156.678969	3	2019-06-15	2020-01-19	1
Kahana 05	KH-05-D4	20.98243	-156.68033	8	2019-06-12	2019-12-30	1
Kahana 06	KH-06-D1	20.9836	-156.6812	13	2018-11-06	2018-11-29	2
Kahana 07	KH-07-D1	20.98058	-156.67638	3	2018-11-08	2019-01-19	2
"	KH-07-D3	"	"	"	2019-01-29	2019-10-04	1
Kahana 08	KH-08-D1	20.98221	-156.67691	4	2018-11-07	2019-01-11	2
Kahana 09	KH-09-D1	20.98172	-156.67496	3	2018-11-08	2019-01-13	2
"	KH-09-D4	"	"	"	2019-06-12	2020-01-14	1
Kahana 11	KH-11-D1	20.97801	-156.67912	3	2018-11-07	2019-01-16	2
"	KH-11-D4	"	"	"	2019-06-12	2020-01-07	1

Kahana 12	KH-12-D1	20.9767	-156.6799	3	2018-11-07	2019-01-13	2
Royal Kahana 01	RK-01-D1	20.96757	-156.68188	2	2018-11-08	2019-01-16	2
Kāʻanapali 02	KA-02-D1	20.9191	-156.6991	8	2018-11-06	2019-01-12	2
"	KA-02-D4	20.91905	-156.699711	12	20-06-15	2020-04-28	1
Kāʻanapali 03	KA-03-D1	20.9191	-156.7002	14	2018-11-06	2019-01-19	2
Kāʻanapali 04	KA-04-D1	20.9108	-156.69205	5	2018-11-09	2019-01-21	2
North Lahaina 01	NL-01-D1	20.89112	-156.68655	4	2018-11-07	2019-01-16	2
Lahaina Harbor 01	LH-01-D1	20.8712	-156.6782	1	2018-11-09	2019-01-20	2
Puamana 52	PU-52-D2	20.85143	-156.662351	2	2019-01-29	2019-09-27	1
Puamana 54	PU-54-D2	20.85074	-156.66301	4.7	2019-01-29	2019-09-18	1
Puamana 55	PU-55-D2	20.85033	-156.66338	9.5	2019-01-31	2019-10-01	1
Puamana 56	PU-56-D4	20.849739	-156.66405	13	2019-06-16	2020-03-23	1
Puamana 57	PU-57-D2	20.85036	-156.66203	4	2019-02-01	2019-09-14	1
Puamana 61	PU-61-D4	20.849989	-156.661189	4	2019-06-15	2019-12-10	1
Puamana 62	PU-62-D4.	20.848911	-156.660031	4	2019-06-15	2020-04-04	1
Launiupoko 01	LP-01-D1	20.84479	-156.65533	2	2018-11-10	2018-12-15	2
Olowalu 02	OL-02-D2	20.80346	-156.5979	2	2019-02-01	2019-10-28	1

Table 2.2 Timeline of Instrument Deployments in West Maui.

	Date:	2018		2019												2020					
Instrument type:	Site:	Nov.	Dec.	Jan.	Feb	Mar.	Apr.	May	Jun.	Jul.	Aug.	Sep.	Oct.	Nov.	Dec.	Jan.	Feb.	Mar.	Apr.	May	Jun.
Pressure Gauge	Oneloa Bay 01																				
	Nāpili Bay 02																				
	Kahana 01																				
	Kahana 01 C																				
	Kahana 02																				
	Kanana 03																				
	Kahana 05																				
	Kahana 06																				
	Kahana 07																				
	Kahana 08																				
	Kahana 09																				
	Kahana 11																				
	Kahana 12																				
	Royal Kahana 01																				
	Kā‘anapali 02																				
	Kā‘anapali 03																				
	Kā‘anapali 04																				
	North Lahaina 01																				
	Lahaina Harbor 01																				

	Puamana 52																				
	Puamana 54																				
	Puamana 55																				
	Puamana 56																				
	Puamana 57																				
	Puamana 61																				
	Puamana 62																				
	Launiupoko 01																				
	Olowalu 02																				
Current Meter	Kāʻanapali 02																				
AWAC	Kahana 06																				
	Puamana 56																				

Table 2.3 Wave events

Columns from left to right: Event code (N# for events from the north, S# for events from the south, E# for periods of weak SS energy); Start time of event (YYYY-MM-DD HH:MM UTC); Dir. @ buoy (direction at the buoy, Pauwela for swells from the north and Lāna‘i Southwest for swells from the south in Decimal Degrees); 32 point compass direction; Hs @ Kahana 5 (max Hs in meters, at Kahana 5); Hs @ Puamana 56 (max Hs in meters), Hs from Puamana 55 for N1 event only; Tp @ Kahana 5 (seconds); Tp @ Puamana 56 (seconds), Tp from Puamana 55 for N1 only.

Event code	Start of event	Dir. @ buoy (DD)	32 point compass	Hs @ Kahana (m)	Hs @ Puamana (m)	Tp @ Kahana (s)	Tp @ Puamana (s)
S1	2019-06-30 12:00	192	SSW	0.8	0.9	18	19
S2	2019-07-14 0:00	192	SSW	0.8	1.0	19	17
S3	2019-08-20 0:00	193	SSW	0.7	0.8	17	17
S4	2019-09-26 0:00	196	SSW	0.6	0.8	18	18
N1	2019-02-10 0:00	327	NNW	-	0.6	-	16
N2	2019-11-15 0:00	344	NNW	1.0	0.4	17	17
N3	2019-12-01 0:00	2	N	1.5	0.6	16	17
N4	2019-12-07 0:00	16	NNE	1.4	0.5	16	15
N5	2019-12-12 0:00	324	NW	1.1	0.4	17	17
N6	2019-12-21 0:00	54	NE	0.7	0.2	10	13
E1	2019-06-23 0:00	173	S	0.2	0.2	11	10
E2	2019-08-26 12:00	162	SSE	0.2	0.3	11	18

E3	2019-10-15 11:00	182	S	0.3	0.3	15	15
E4	2019-11-02 4:00	167	SSE	0.3	0.3	11	14

Table 4.1 Modeled Events

Columns from left to right: simulation run number; date and time of simulated event (UTC); time of SWAN forecast directional spectra input (UTC) (note: this is shifted in time for some simulations to match the time of arrival of the swell); significant wave heights (meters), peak period (seconds) and direction (degrees) as forecast by SWAN (values taken Near the Pauwela buoy for swells from the north, and near the Lānaʻi Southwest Buoy for swells from the south, from PacIOOS Voyager); the water level (WL) is the verified tide level relative to MSL from tide gauge observations at Kahului Harbor (via NOAA's Tides & Currents website); using the max WL for that day or the actual WL at the time of the event; BOSZ computational domain (1 = north, 2 = south); grid resolution (Δ x meters, Δ y meters); average duration time of the computation, per domain.

Simulation Run #	Time of Event [UTC]	Time of SWAN Input [UTC]	Hs / Tp/ Dir SWAN @ Pauwela (N) /Lānaʻi (S)	WL [m]	Max/actual Water Level	Domain	Grid Resolution [m x m]	Computation duration per domain
1	2019-01-09 23:00	2019-01-09 23:00	2.6 m/ 16 s/ 25°	0.512	max	1	8 x 12	12 hours
2	2019-01-09 23:00	2019-01-09 23:00	"	-0.03	actual	1	10 x 10	12 hours
3	2019-01-09 23:00	2019-01-09 23:00	"	0.512	max	1	5 x 5	2 days
4	2019-01-09 23:00	2019-01-09 23:00	"	-0.03	actual	1	5 x 5	2 days
5	2019-01-09 23:00	2019-01-09 23:00	"	-0.03	atual	1	3 x 3	< 1 week

6.1	2019-07-14 22:00	2019-07-14 12:00	1.4 m/ 18 s/ 195°	0.415	actual	1 & 2	5 x 5	2 days
6.2	2019-07-14 23:00	2019-07-14 13:00	"	0.478	"	"	"	"
6.3	2019-07-15 0:00	2019-07-14 14:00	"	0.54	"	"	"	"
6.4	2019-07-15 1:00	2019-07-14 15:00	"	0.501	"	"	"	"
6.5	2019-07-15 2:00	2019-07-14 16:00	"	0.435	"	"	"	"
7.1	2019-12-07 19:00	2019-12-08 0:00	2.7 m/ 15 s/ 25°	0.275	actual	1 & 2	5 x 5	2 days
7.2	2019-12-07 20:00	2019-12-08 1:00	"	0.269	"	"	"	"
7.3	2019-12-07 21:00	2019-12-08 2:00	"	0.347	"	"	"	"
7.4	2019-12-07 22:00	2019-12-08 3:00	"	0.31	"	"	"	"
7.5	2019-12-07 23:00	2019-12-08 4:00	"	0.205	"	"	"	"

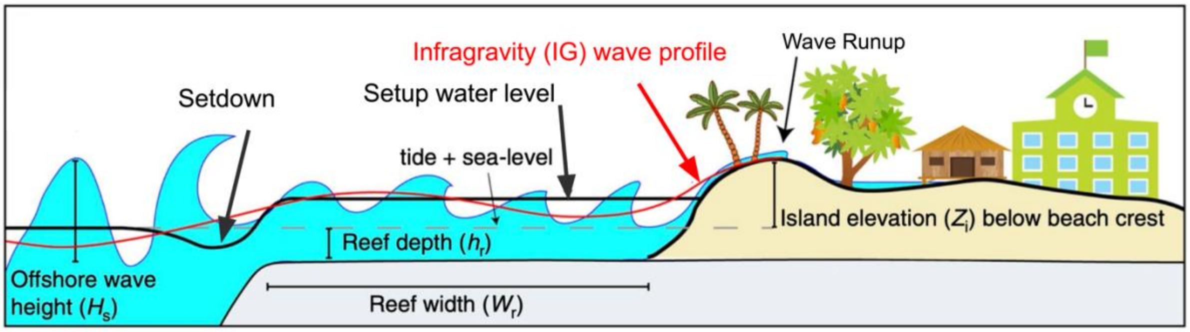

Figure 1.1 Summary of wave interactions with reef flats.
Figure modified from Beetham & Kench., 2018.

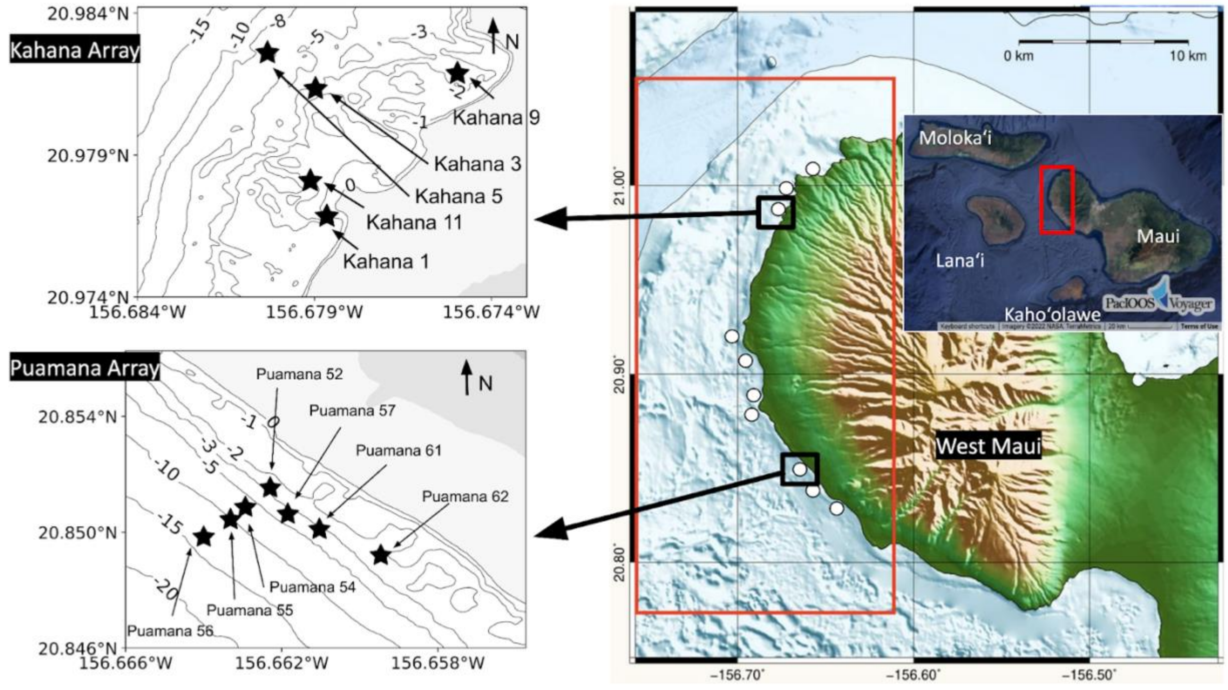

Figure 1.2 Study Site. Maps of Kahana array (top left , Puamana array (bottom left), WM (center) and the Maui Nui island group (top right).

The stars in the maps for the Kahana and Puamana arrays are the locations of the pressure gauges (not all are shown here), contour depths are in meters. The circles on the map of WM are the locations of deployments. Map of Maui Nui from PacIOOS Voyager (http://www.pacioos.hawaii.edu/voyager/, 2022).

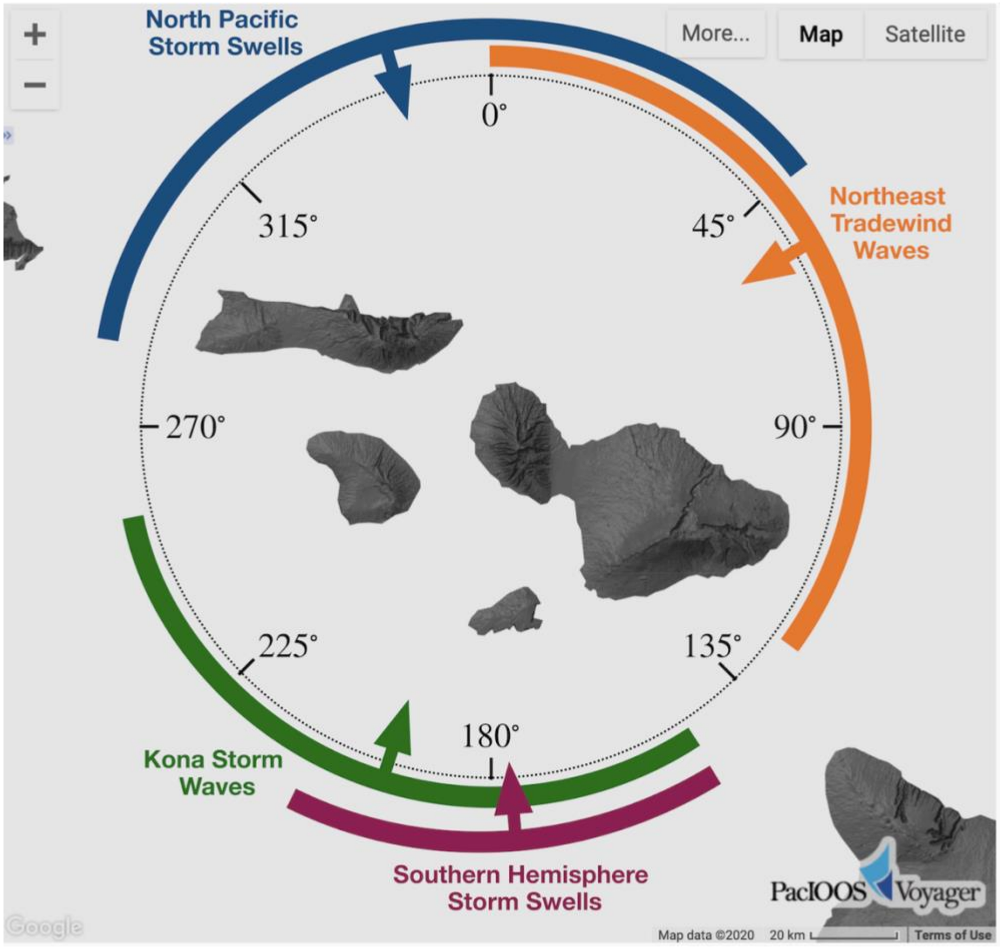

Figure 1.3 Map showing the main swells impacting the Maui Nui island group.
Figure from PacIOOS Voyager, 2022. http://www.pacioos.hawaii.edu/shoreline-category/runup-westmaui/#details

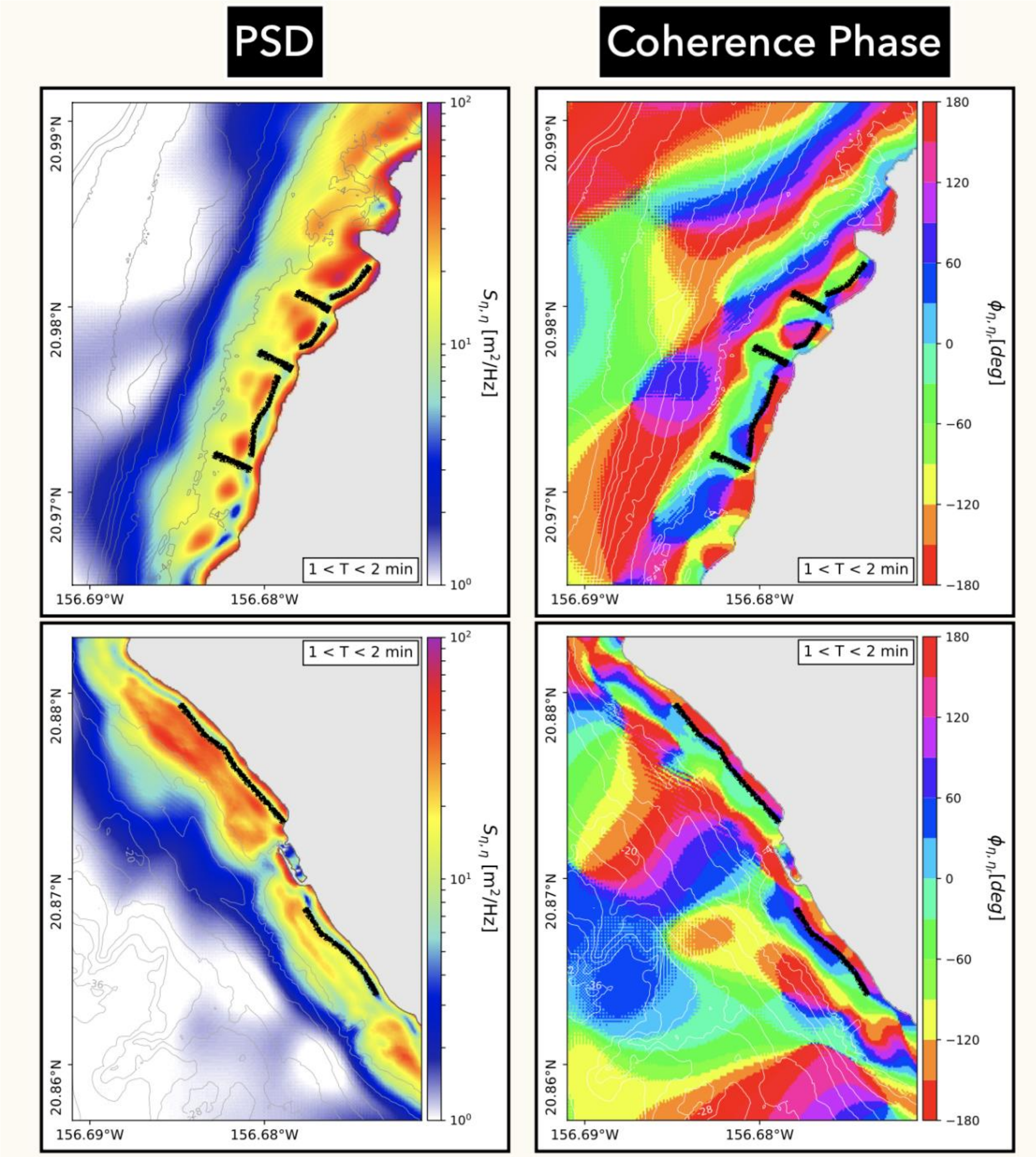

Figure 1.4 BOSZ Model Maps of Power Spectral Density (PSD) and Coherence Phase for WM in the period band of 1-2 minutes.

Note the complex coherence phase pattern and the distinctive 8 maxima in PSD very near shore in the Kahana region at these periods (indicating dominance of a longshore mode) compared to the smoother alongshore phase and PSD in the Lahaina area (indicating un-phase-locked alongshore propagation). Taken from Azouri et al., 2018.

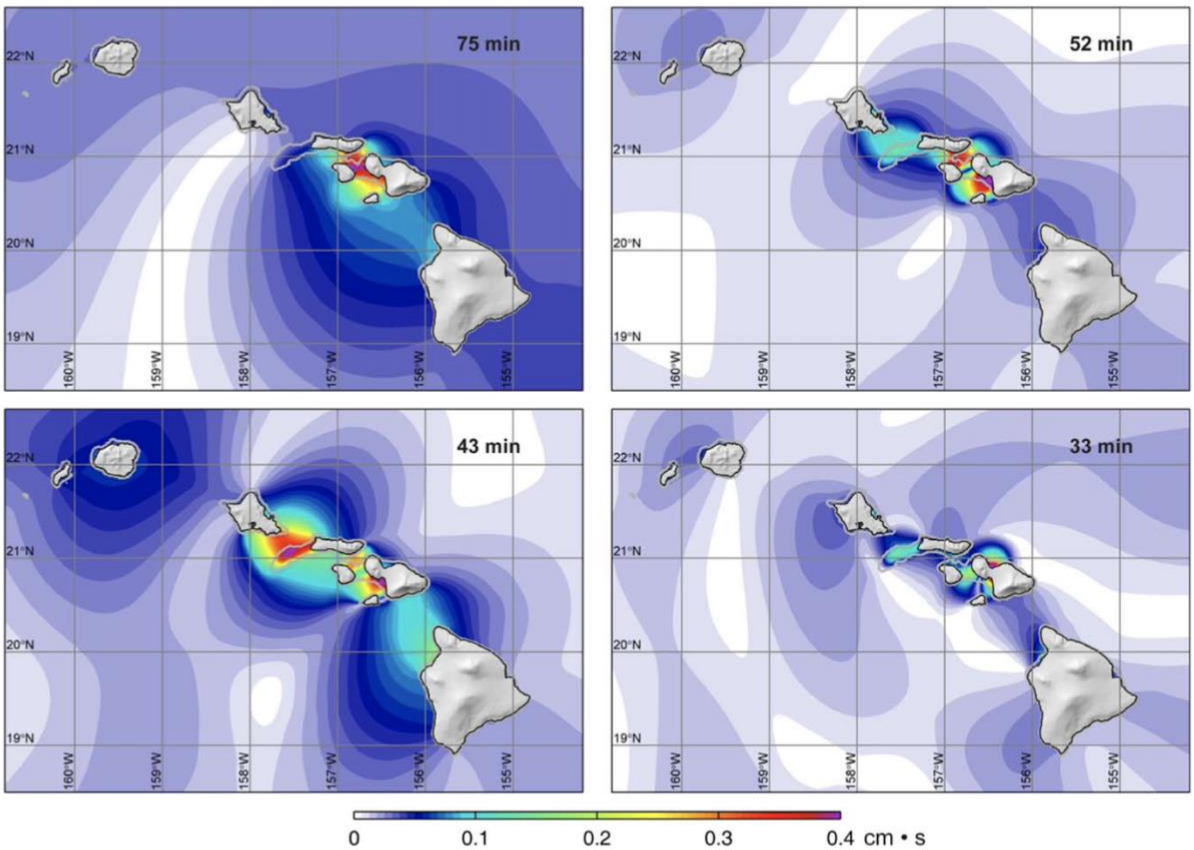

Figure 5. Spectral amplitude of surface-elevation time series around the Hawaiian Islands. Gray lines are 100 m depth contours delineating the approximate extent of insular shelves.

Figure 1.5 Figure 5 from Cheung et al., 2013, showing long-period infragravity modes around the Hawaiian Islands that were excited in response to the 2011 Tohoku tsunami.

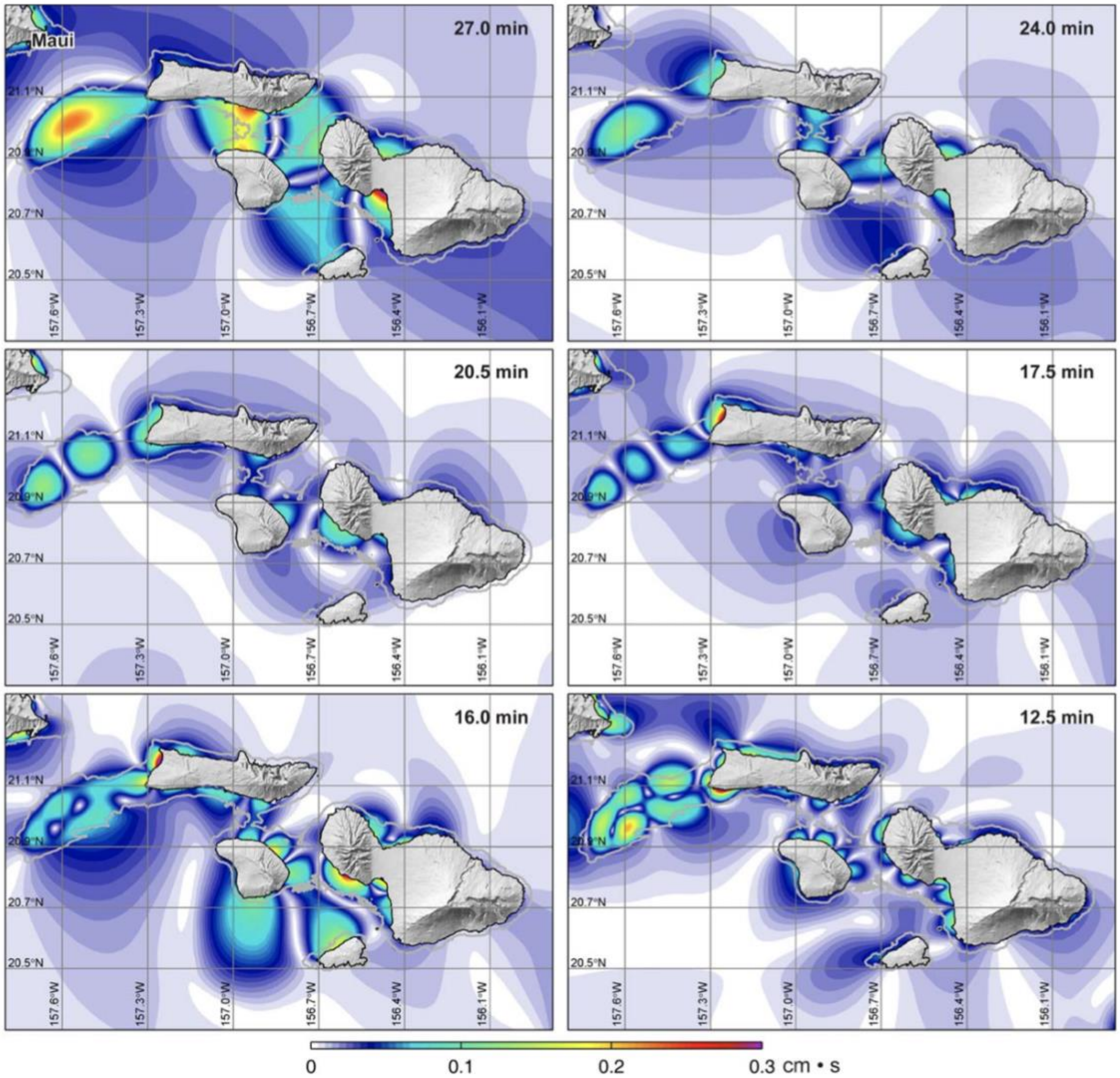

Figure 9. Spectral amplitude of surface-elevation time series around Maui Nui. Gray lines are 100 m depth contours delineating the approximate extent of insular shelves.

Figure 1.6 Figure 9 from Cheung et al., 2013, showing more long-period infragravity modes around the Hawaiian Islands that were excited in response to the 2011 Tohoku tsunami.

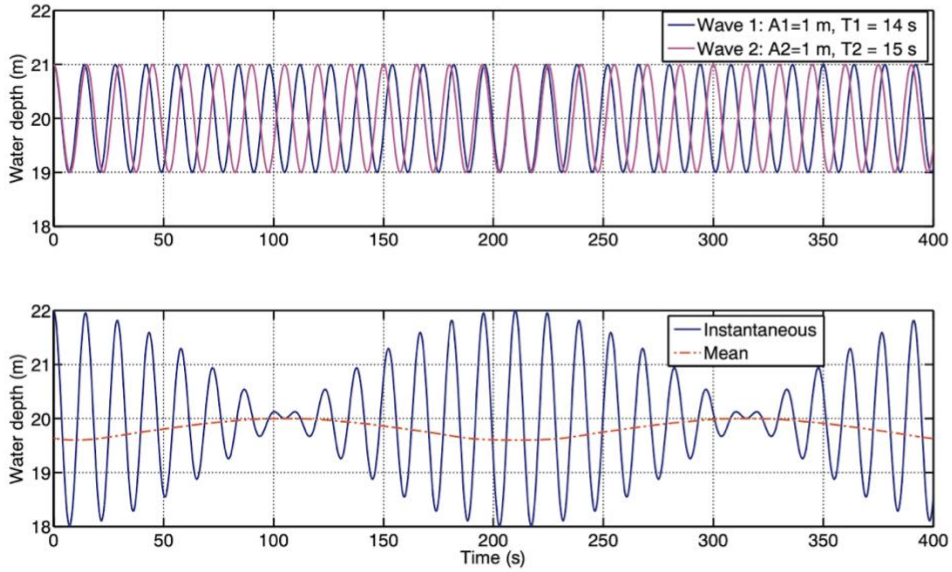

Fig. 2. (A) Time series of two sinusoidal waves with periods of 14 s (blue) and 15 s (pink) travelling over a flat bottom by 20 m water depth. (B) Resulting free surface elevation (blue) and bound wave (red) as computed according to Longuet-Higgins and Stewart (1962).

Figure 1.7 Figure 2 from Bertin et al. 2018.

The caption reads: (A) Time series of two sinusoidal waves with periods of 14 s (blue) and 15 s (pink) travelling over a flat bottom by 20 m water depth. (B) Resulting free surface elevation (blue) and bound wave (red) as computed according to Longuet-Higgins and Stewart (1962).

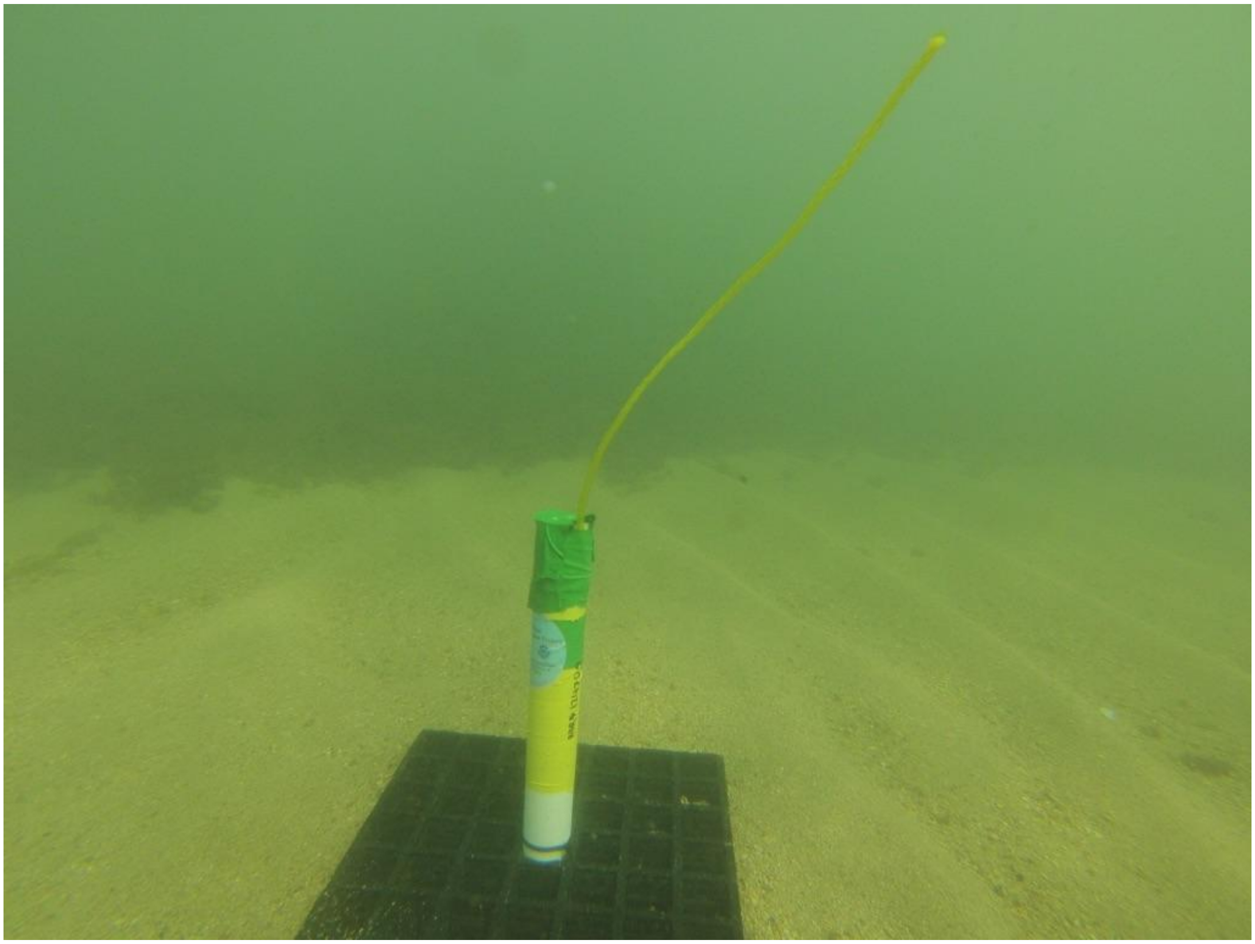

Figure 2.1 Pressure gauge deployment at Kahana 11 (D1) in 3 meters depth.

Figure 2.2 Deployment package.

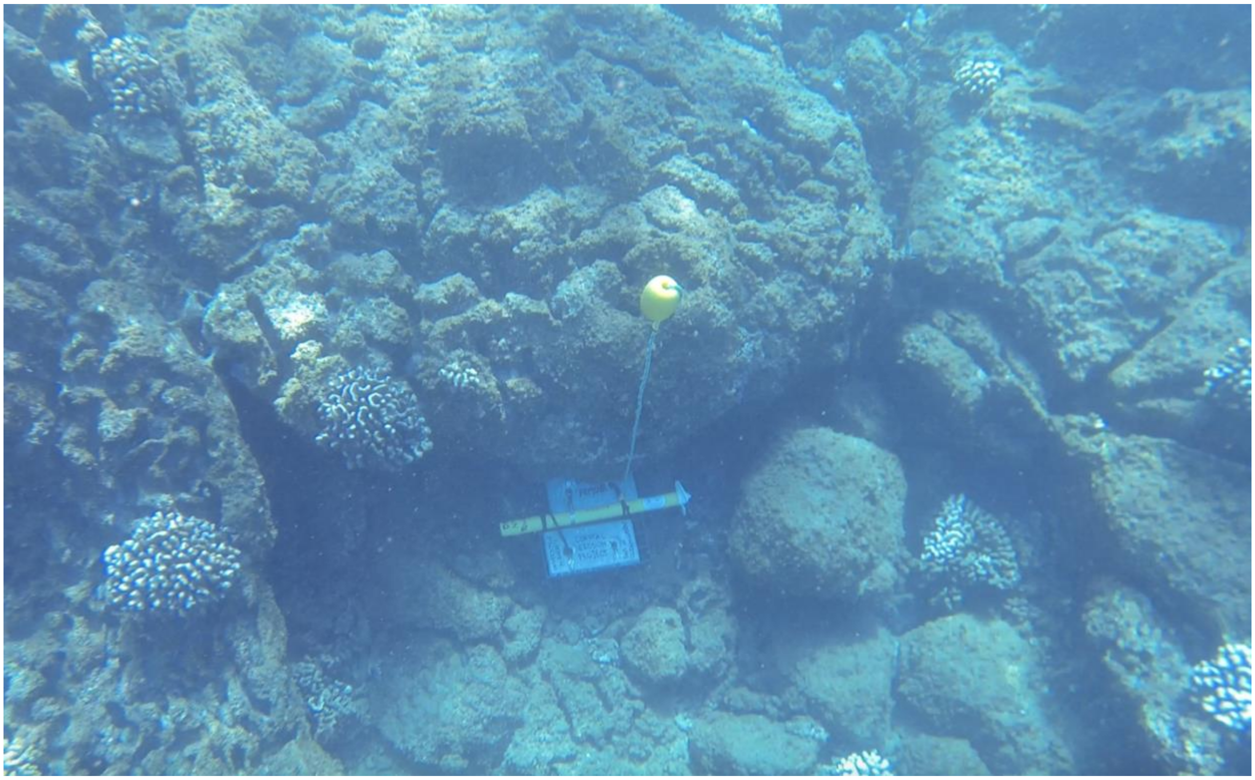

Figure 2.3 Pressure gauge deployment at Nāpili Bay 02 in 3 meters depth.

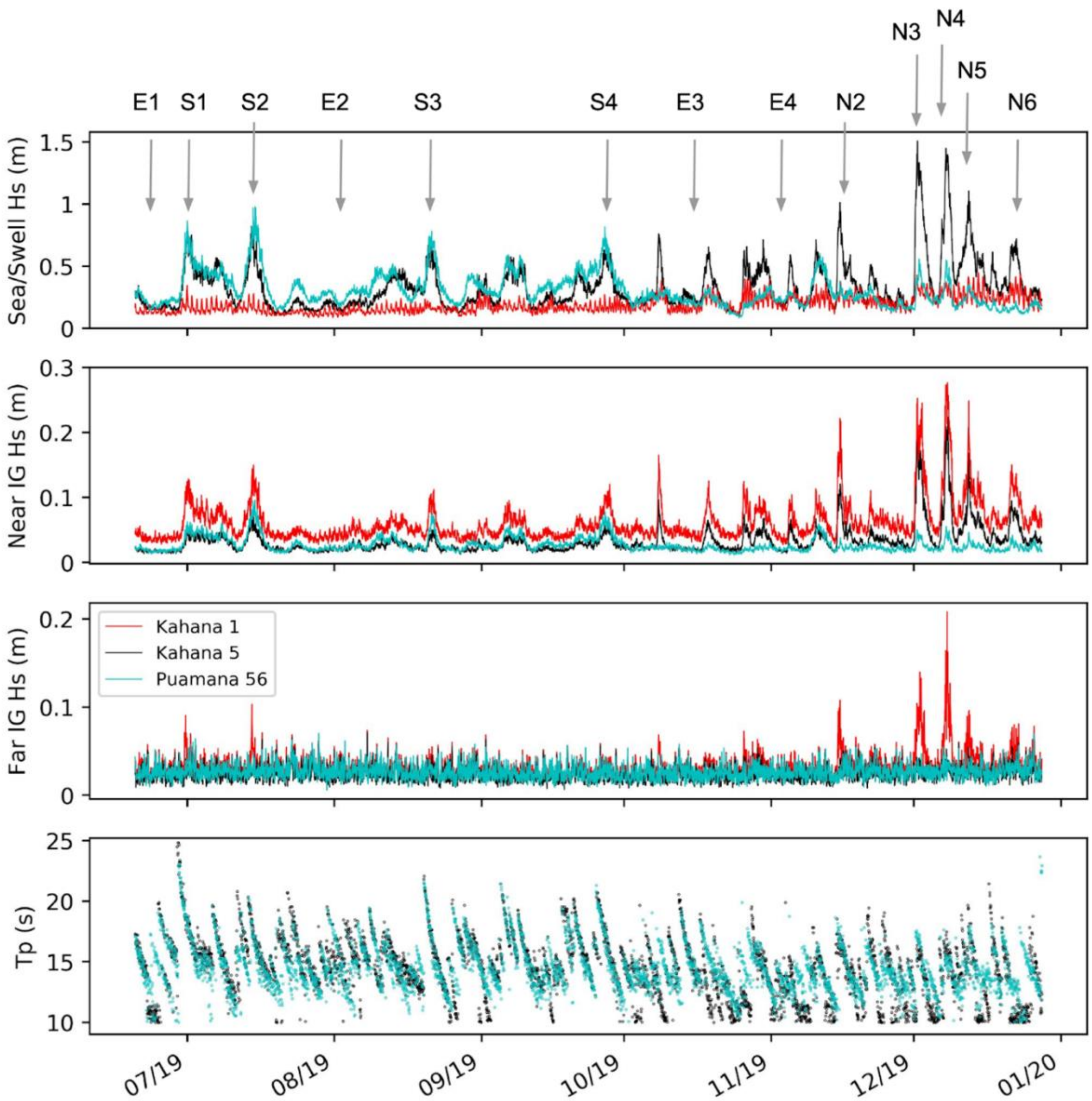

Figure 2.4 Time series of SS Hs (5-25 sec), Near IG Hs (25-250 sec), Far IG Hs (250 sec – 90 min) and SS peak period, Tp, for June 20 - Dec. 30, 2019.

Puamana 56 is cyan, Kahana 5 is black and Kahana 1 is red. Puamana 56 and Kahana 5 are the deepest sensors in their respective arrays; Kahana 1 is the shallowest Kahana Array sensor. Details for the events marked by the arrows can be found in Table 2.3.

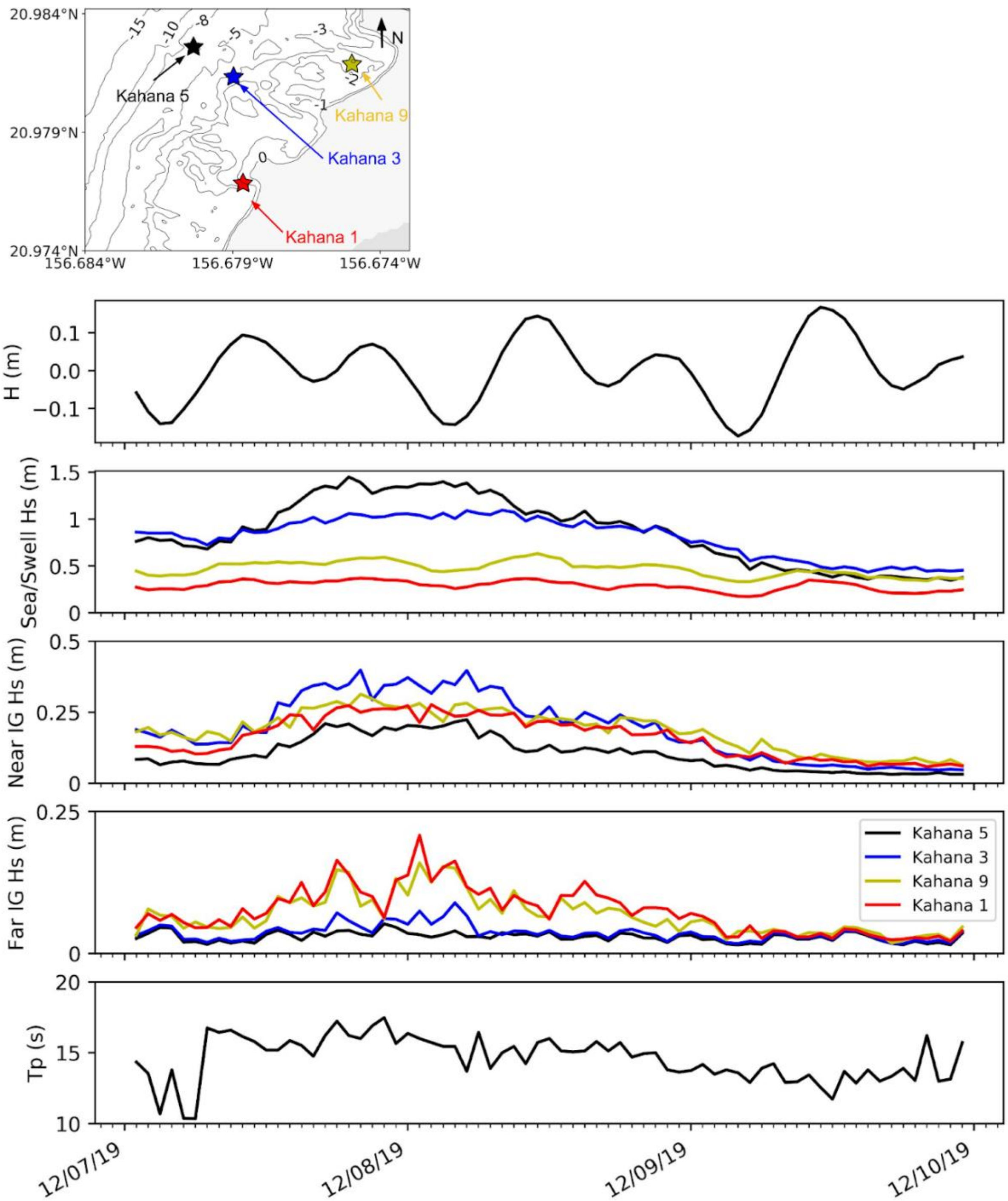

20.984°N
20.979°N
20.974°N
156.684°W
156.679°W
156.674°W
-15
-10
-8
-5
-3
-2
-1
0
N
Kahana 5
Kahana 3
Kahana 9
Kahana 1
H (m)
Sea/Swell Hs (m)
Near IG Hs (m)
Far IG Hs (m)
Tp (s)
12/07/19
12/08/19
12/09/19
12/10/19

Figure 2.5 Kahana Array time series, December 7-10, 2019 (N4 event).

Panels from top to bottom: low pass filter, H; Sea/Swell Hs (5-25 sec), Near IG Hs (25-250 sec), Far IG Hs (250 sec – 90 minutes) and peak period, Tp. Kahana 5 is black, Kahana 3 is blue, Kahana 9 is yellow and Kahana 1 is red.

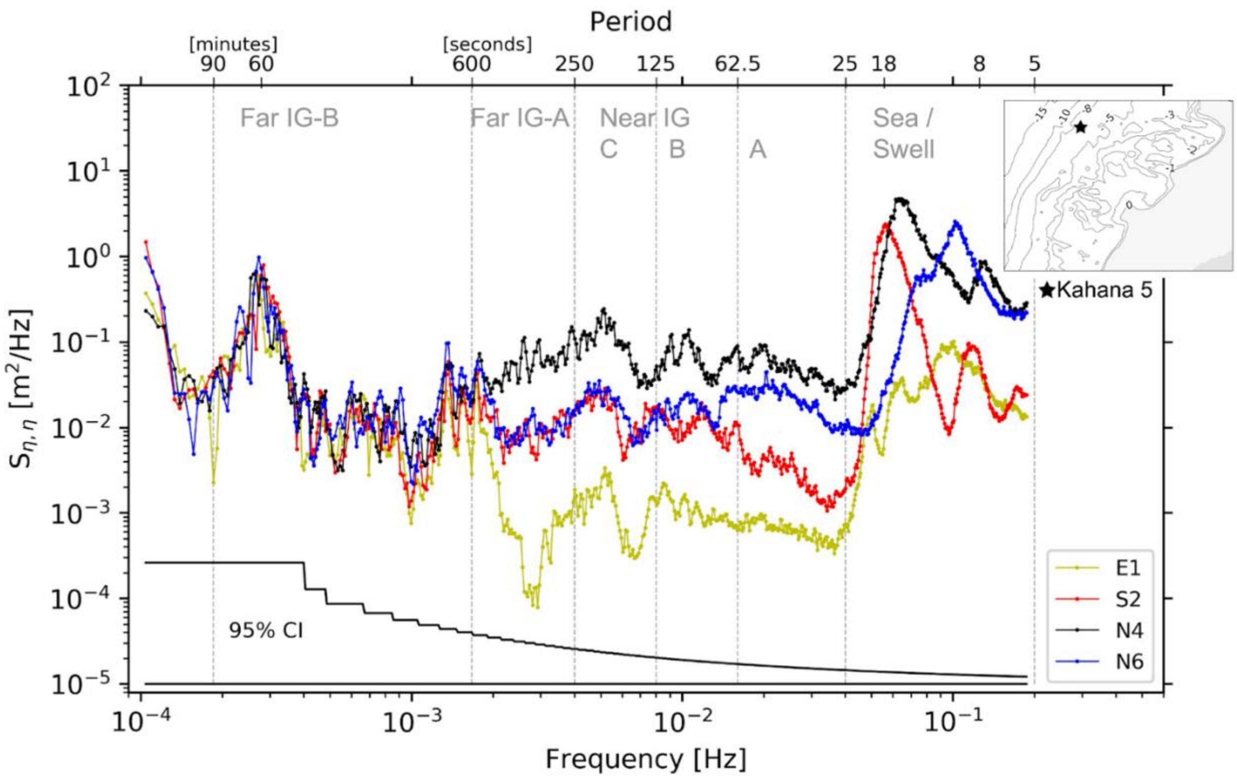

Figure 2.6 PSD generated using two-day long segments of sea level observations for different wave events at Kahana 5.
Details for the events in Table 2.3. The 95% confidence interval for each independent spectral estimate is plotted at the bottom. Every other point plotted is independent due to the 50% overlap of the frequency band averaging intervals.

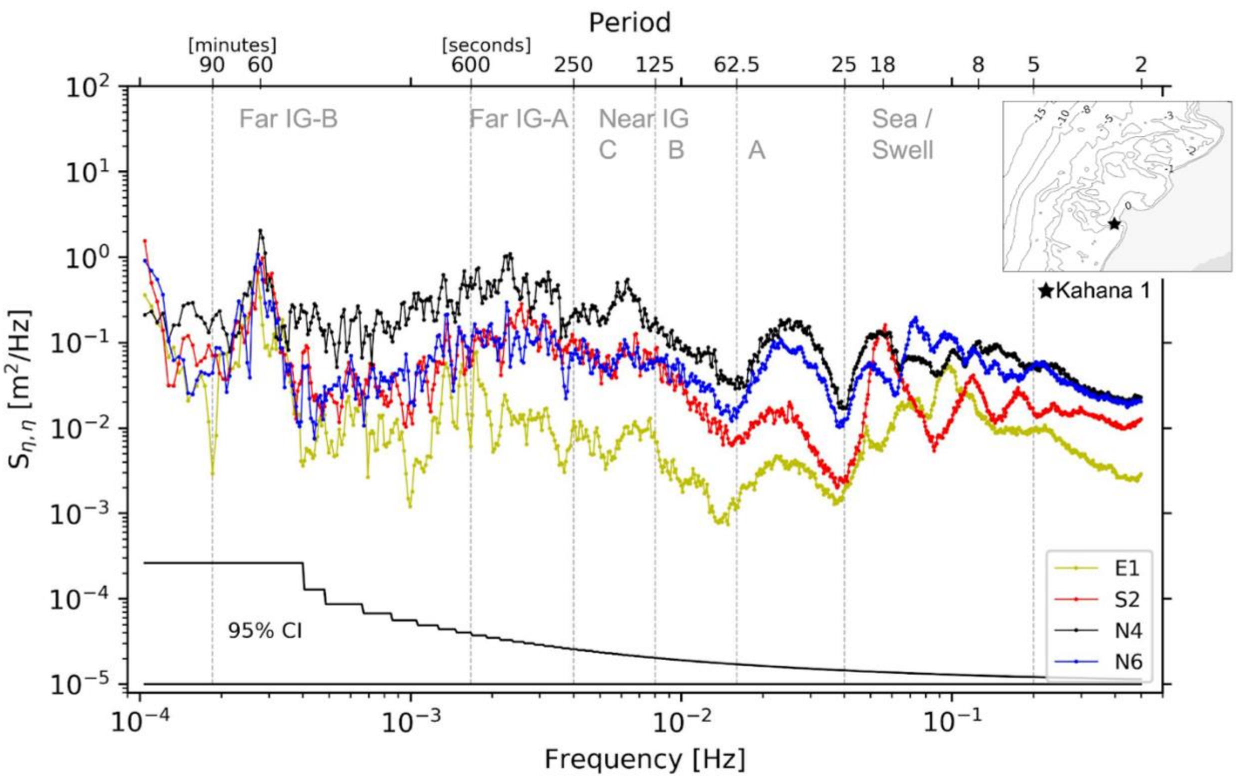

Figure 2.7 PSD generated using two-day long segments of sea level observations for different wave events at Kahana 1.

Details for the events in Table 2.3. The 95% confidence interval for each independent spectral estimate is plotted at the bottom. Every other point plotted is independent due to the 50% overlap of frequency band averaging intervals.

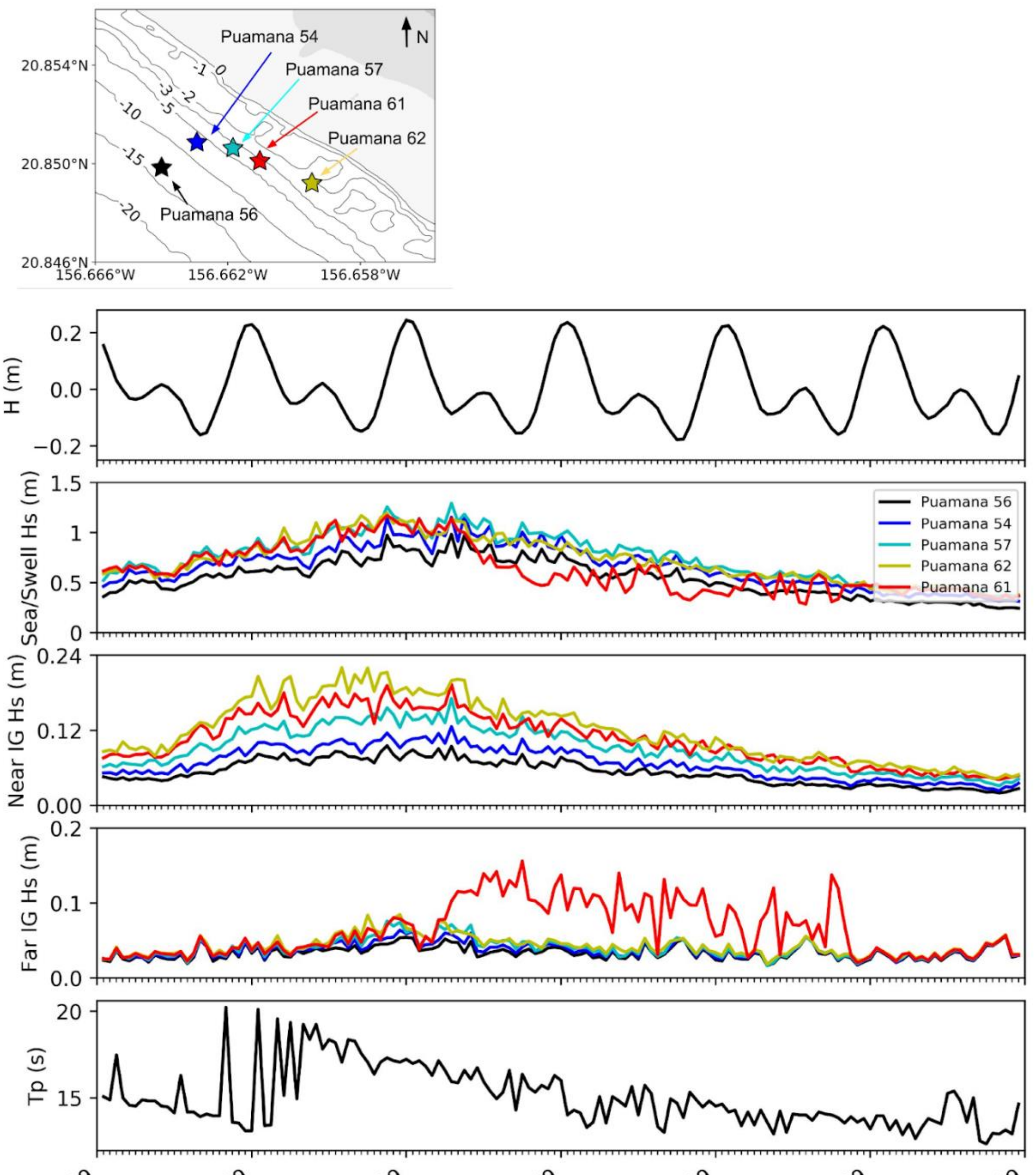

Puamana 54
N
20.854°N
-1
0
Puamana 57
-2
-3.5
-10
Puamana 61
Puamana 62
20.850°N
-15
-20
Puamana 56
20.846°N
156.666°W
156.662°W
156.658°W
H (m)
Sea/Swell Hs (m)
Puamana 56
Puamana 54
Puamana 57
Puamana 62
Puamana 61
Near IG Hs (m)
Far IG Hs (m)
Tp (s)
07/13/19
07/14/19
07/15/19
07/16/19
07/17/19
07/18/19
07/19/19

Figure 2.8 Puamana Array time series, July 13 - 19 2019 (S2 event).

Panels from top to bottom: low pass filter, H; Sea/Swell Hs (5-25 sec), Near IG Hs (25-250 sec), Far IG Hs (250 sec – 90 minutes) and peak period, Tp. Puamana 56 is black, Puamana 54 is blue, Puamana 57 is cyan, Puamana 62 is yellow and Puamana 61 is in red .

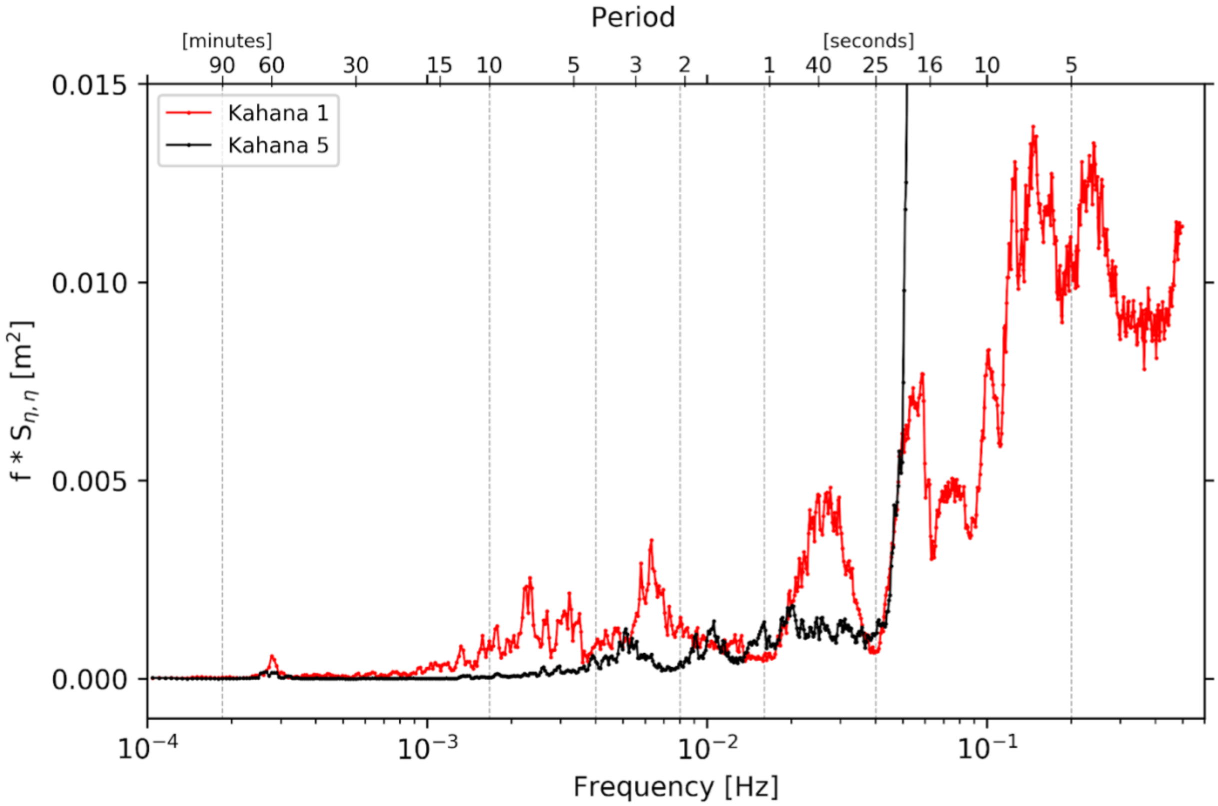

Figure 2.9 Variance preserving spectra of two-day segments of sea level observations from Kahana 1 and Kahana 5 for event N4 (December 7-10, 2019).

The figure is cropped to focus on the nearshore gauge, Kahana 1.

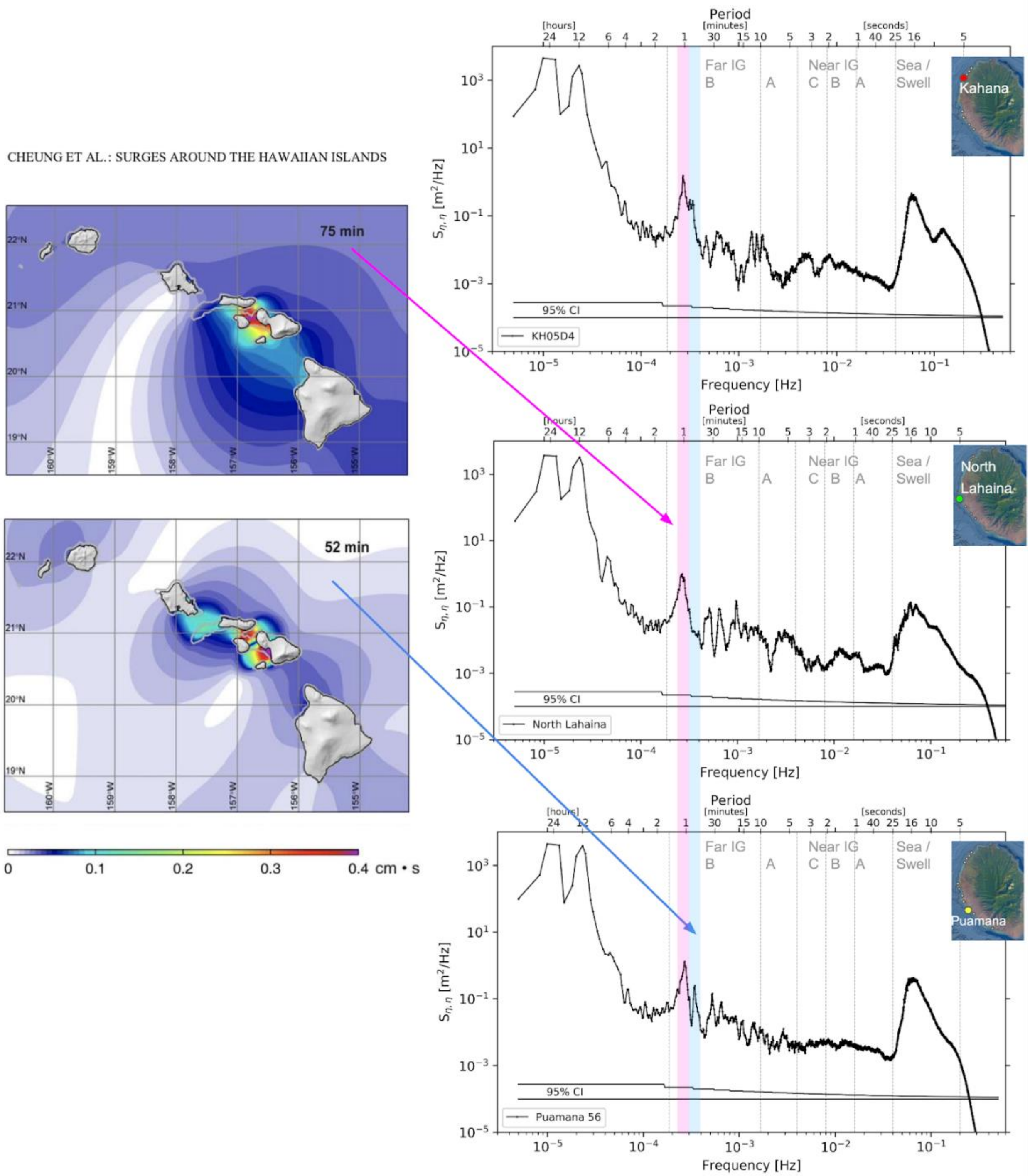

Figure 2.10 Spectra from different locations around WM compared to figures from Cheung et al. 2013.

Left: PSD of surface elevation time series from Maui Nui for mode periods of 75 and 52 minutes (Cheung et al., 2013). Right: PSD generated using five one-week long segments of sea level observations from: Kahana 5 (7/1 - 8/4, 2019), North Lahaina 1 (11/14 - 12/19, 2018) and

Puamana 56 (7/1 - 8/4, 2019). The 95% confidence interval for each independent spectral estimate is plotted at the bottom. Every other point plotted is independent due to the 50% overlap of frequency band averaging intervals. The peaks in the spectra corresponding to the periods in the maps are highlighted and marked by the arrows.

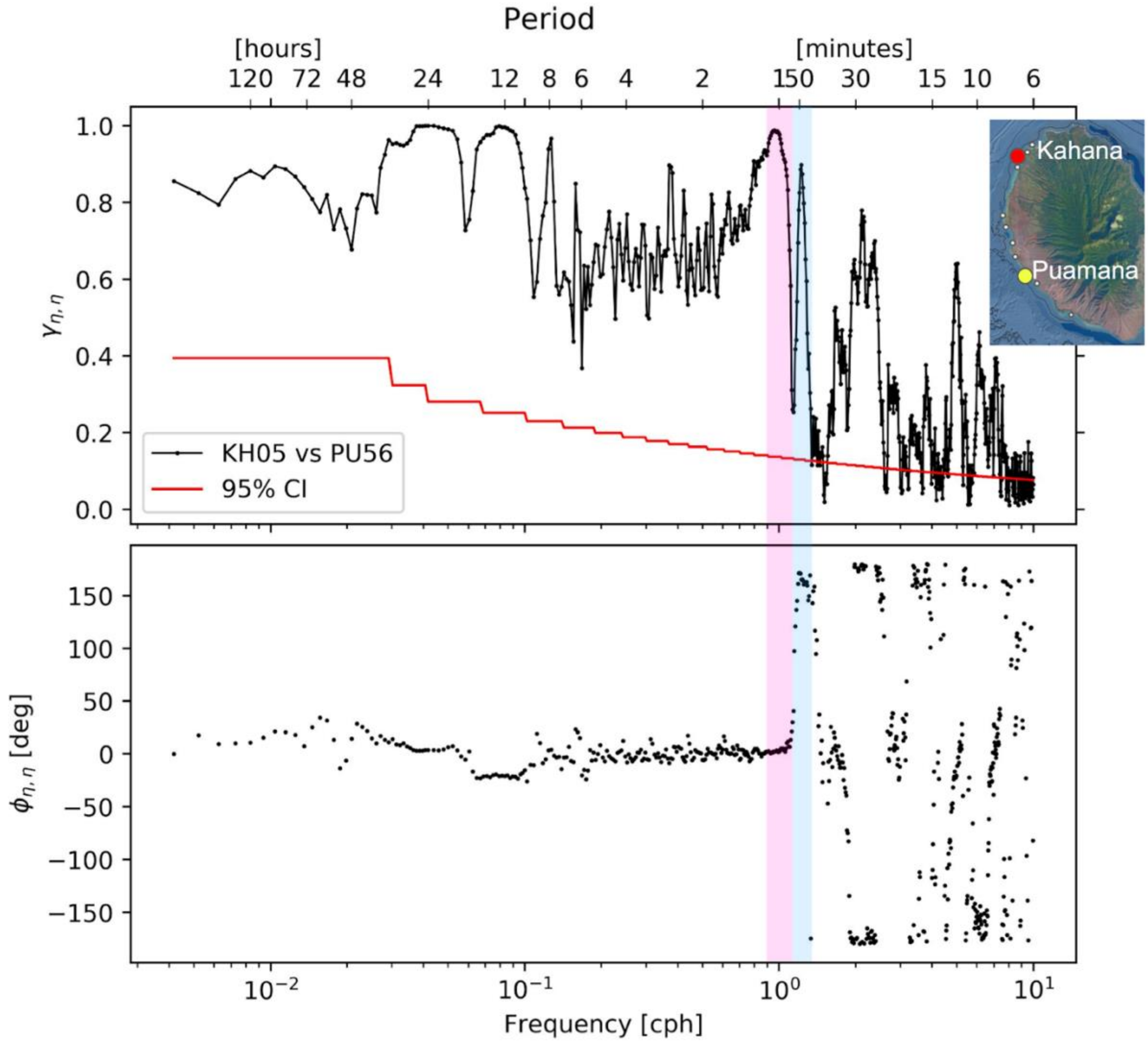

Figure 2.11 Coherence amplitude and phase of sea level observations from Kahana 5 and Puamana 56.

Using five forty-day long segments of data (6/17 - 12/25, 2019). The 95% level of no confidence for the coherence amplitude is plotted in red. Positive values of the coherence phase indicate propagation from south to north, with the first station leading the second. The periods highlighted correspond to the periods highlighted in Figure 2.10.

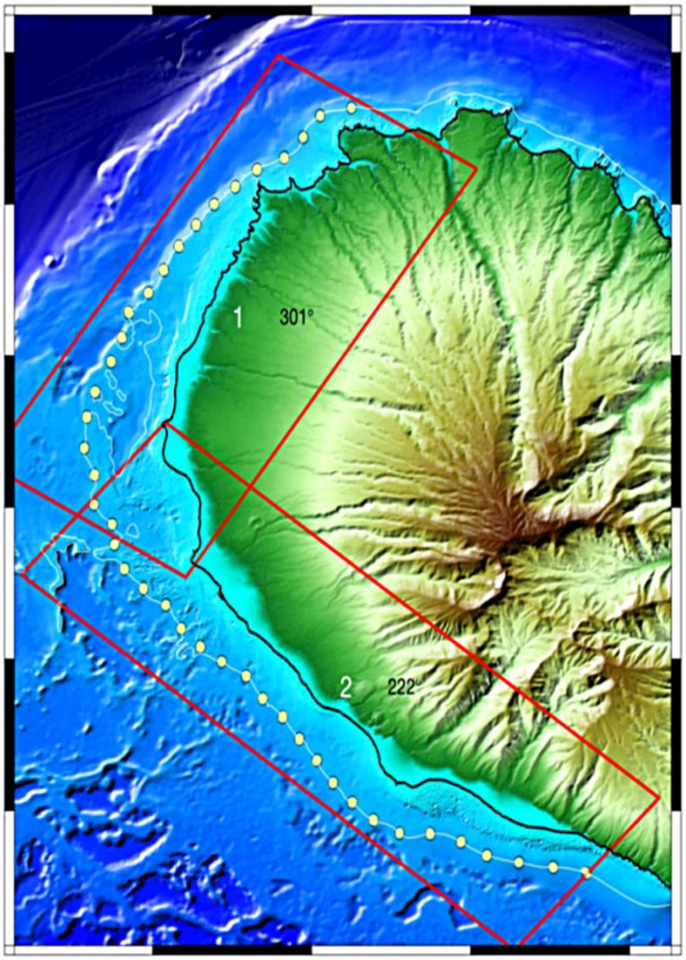

Figure 3.1 Map of the 2-domain BOSZ setup for modeling gravity wave energy transformations near the shore along the West Maui coastline.

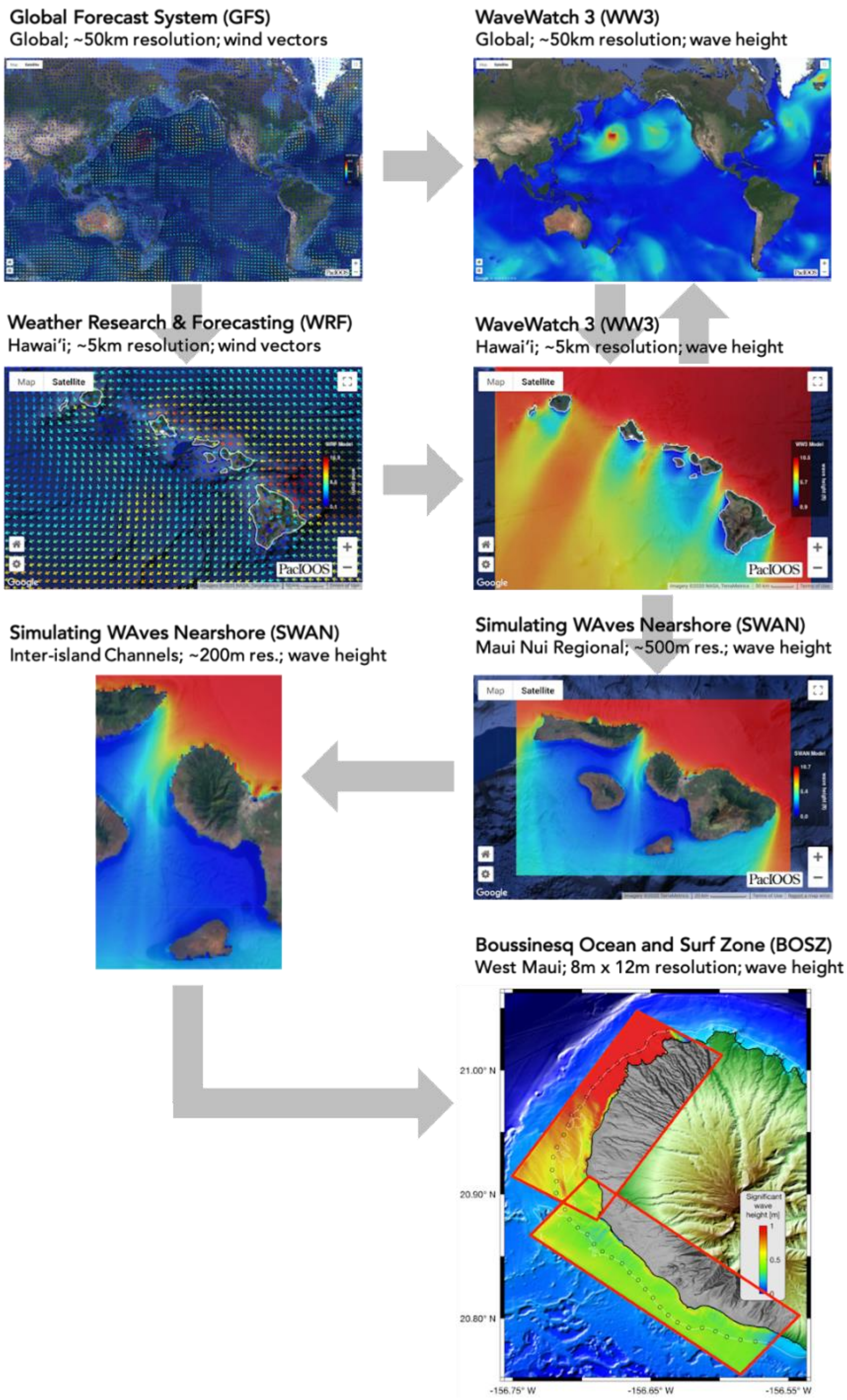

Figure 3.2 Hierarchy of the wind and wave numerical models that are used for creating the West Maui Run-up Forecasts.

The direction of data flow among the models is indicated with the arrows. The model names, scale of computational domains, spatial grid resolutions, and the environmental variable plotted in color are shown next to each panel. These particular examples show wind or wave amplitudes from each model for January 9, 2019, 17:00 HST. Note that the color scales differ from model to model. Image and caption taken from PacIOOS Voyager (Note: this example shows BOSZ with an 8 x 12 meter grid; we use various grid sizes for BOSZ in this study).

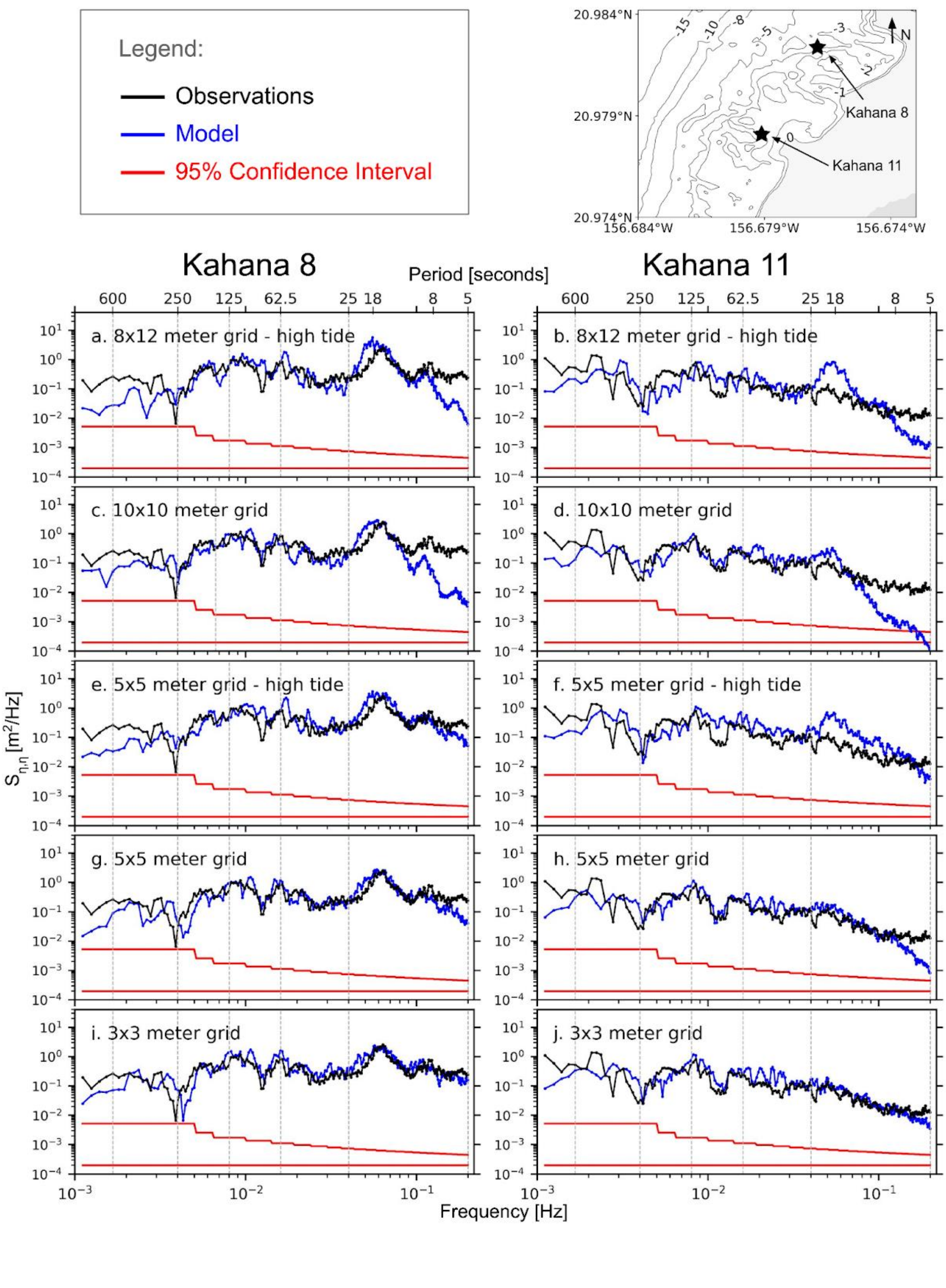

Legend:
Observations
Model
95% Confidence Interval
Kahana 8
Kahana 11
Period [seconds]
a. 8x12 meter grid - high tide
b. 8x12 meter grid - high tide
c. 10x10 meter grid
d. 10x10 meter grid
e. 5x5 meter grid - high tide
f. 5x5 meter grid - high tide
g. 5x5 meter grid
h. 5x5 meter grid
i. 3x3 meter grid
j. 3x3 meter grid
$S_{\eta,\eta}$ [m²/Hz]
Frequency [Hz]

Figure 4.1 PSD of sea level model simulations and observations from the Kahana array.

January 9, 2019 at 23:00 UTC (runs # 1-5, table 4.1). Spectra of two hours of sea level observations from the pressure gauge at Kahana 8 are shown on the left side (black curves). Spectra of two hours of sea level data at the time of the event from the pressure gauge at Kahana 11 are shown on the right side (black curves). Spectra generated using model output with different grid sizes and water levels are shown in the blue curves for: (a & b) simulation 1 with an 8 x 12 meter grid and the max WL, (c & d) simulation 2 with a 10 x 10 meter grid and the actual WL, (e & f) simulation 3 with a 5 x 5 meter grid and the max WL, (g & h) simulation 4 with a 5 x 5 meter grid and the actual WL, (i & j) simulation 5 with a 3 x 3 meter grid and the actual WL. The 95% confidence interval for each independent spectral estimate is plotted in red. Every other point plotted is independent due to the 50% overlap of frequency band averaging intervals.

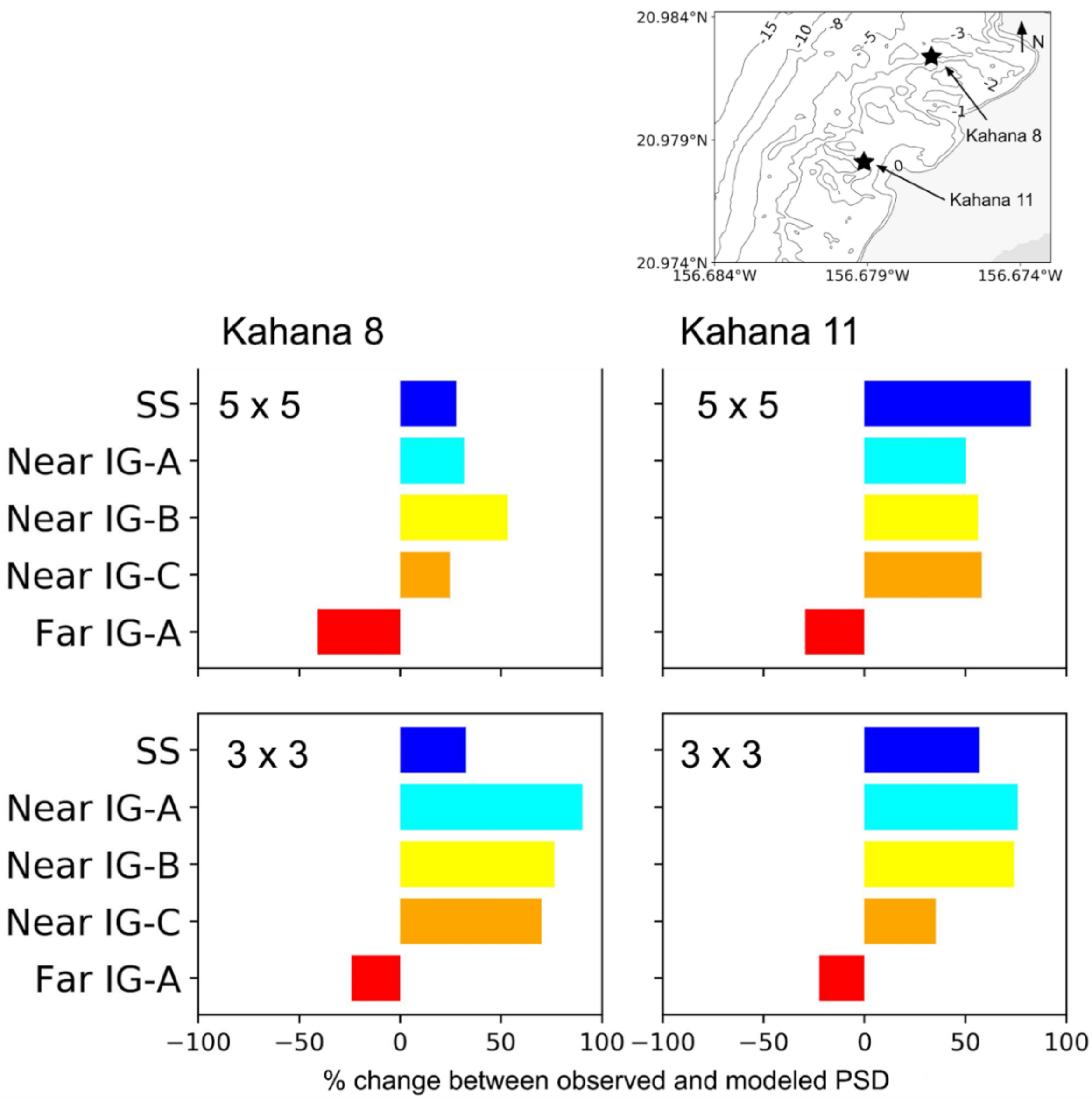

Figure 4.2 Percent difference between observed and modeled PSD (runs # 1-5, table 4.1).

Left side: Kahana 8 with a 5x5 meter grid (top left), and with a 3x3 meter grid (bottom left). Right side: Kahana 11 with a 5x5 meter grid (top right), and with a 3x3 meter grid (bottom right). The colors are blue for the Sea/Swell period band (5 - 25 seconds), cyan for the Near IG-A period band (25 - 62.5 seconds), yellow for the Near IG-B period band (62.5 - 125 seconds), orange for the Near IG-C period band (125 - 250 seconds), and red for the Far IG-A period band (250 - 600 seconds).

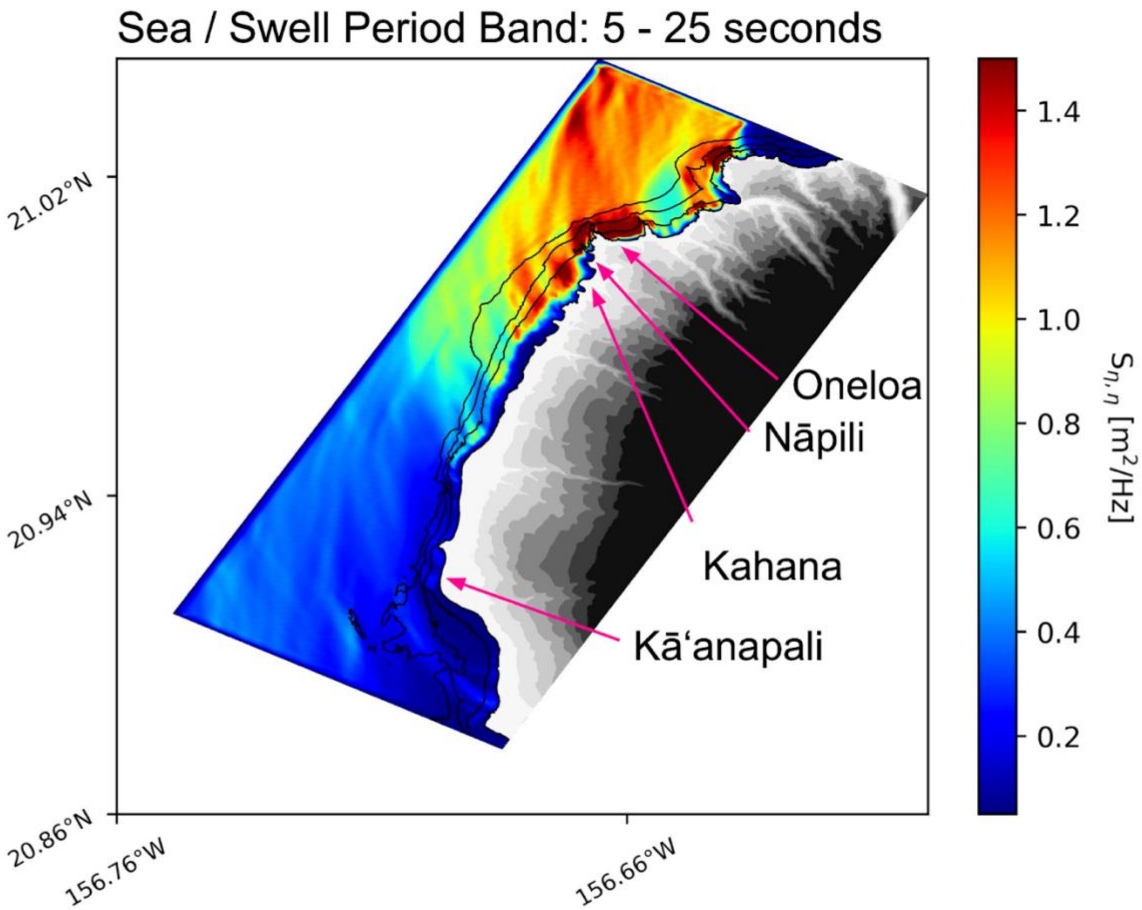

Figure 4.3 Map of model domain 1 (Lahaina to Honolua), showing band averaged PSD in the Sea/Swell period band generated using model output for the N4 event (run # 7.1, Table 4.1). Black contour lines show depths of 10, 20 and 30 meters.

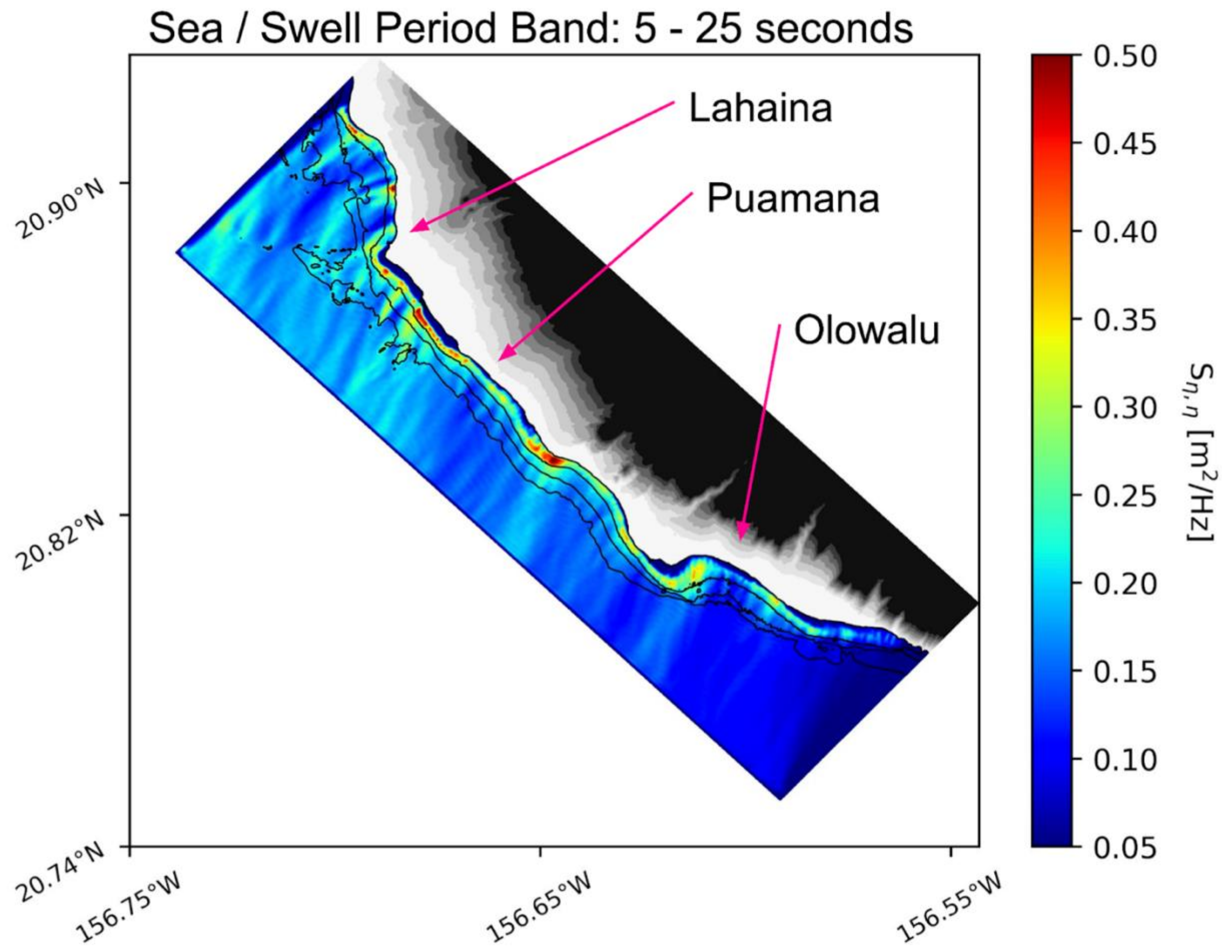

Figure 4.4 Map of model domain 2 (Ukumehame to Lahaina), showing band averaged PSD in the Sea/Swell period band generated using model output for the S2 event (run # 6.1, Table 4.1). Black contour lines show depths of 10, 20 and 30 meters.

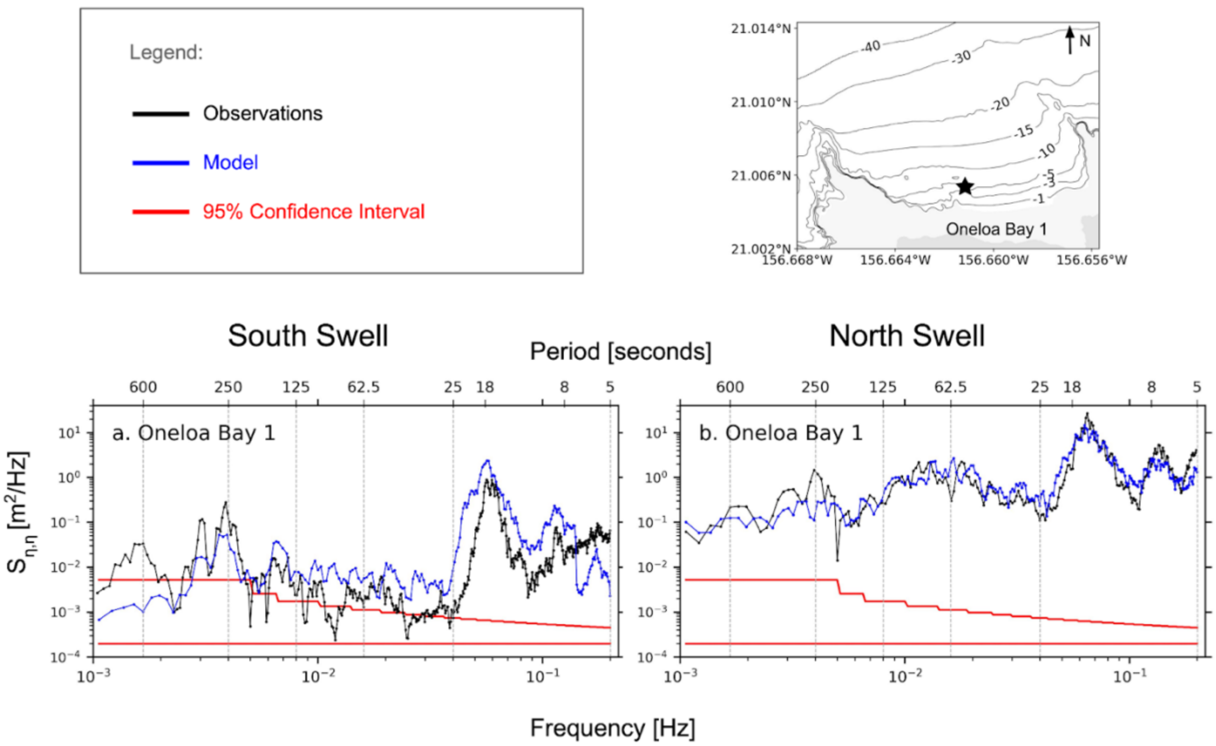

Figure 4.5 PSD of sea level model simulations and observations from Oneloa Bay.
(a) the S2 event and (b) the N4 event (runs # 6.1 & 7.1, table 4.1). Spectra of two hours of sea level data from the pressure gauge are shown in the black curves. Spectra generated using model output are shown in the blue curves. The 95% confidence interval for each independent spectrum estimate is plotted in red. Every other point plotted is independent due to the 50% overlap of frequency band averaging intervals.

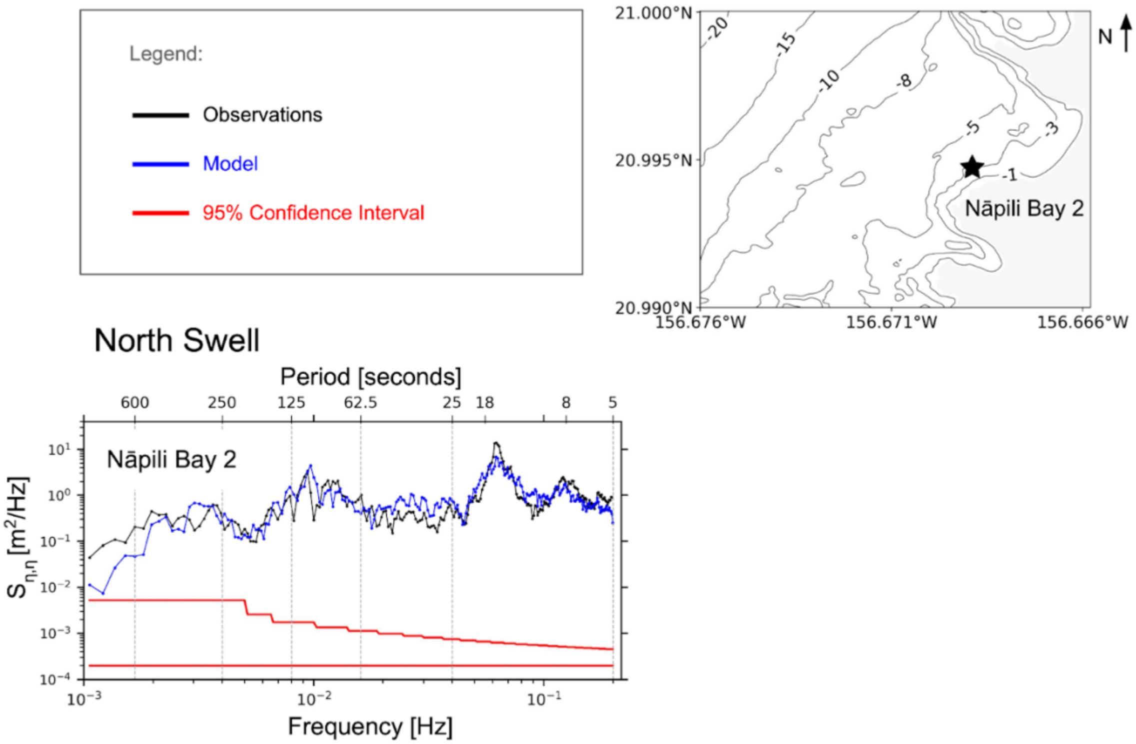

Figure 4.6 PSD of sea level model simulations and observations from Nāpili Bay.

N4 event, (run # 7.1, table 4.1). Spectra of two hours of sea level data from the pressure gauge are shown in the black curves. Spectra generated using model output is shown in the blue curve. The 95% confidence interval for each independent spectral estimate is plotted in red. Every other point plotted is independent due to the 50% overlap of frequency band averaging intervals.

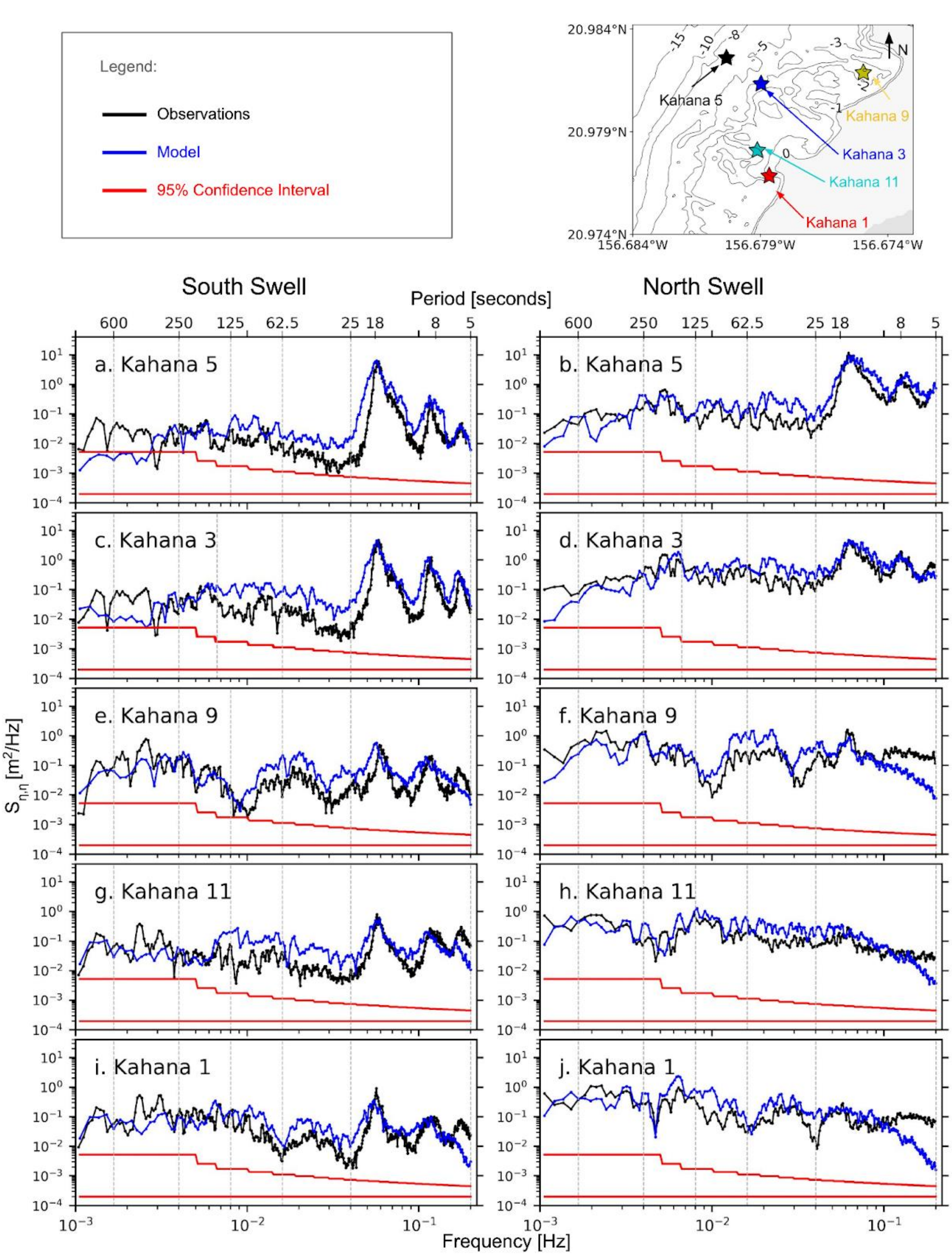
Legend:
Observations
Model
95% Confidence Interval
20.984°N
20.979°N
20.974°N
156.684°W
156.679°W
156.674°W
N
Kahana 5
Kahana 3
Kahana 9
Kahana 11
Kahana 1
South Swell
North Swell
Period [seconds]
a. Kahana 5
b. Kahana 5
c. Kahana 3
d. Kahana 3
e. Kahana 9
f. Kahana 9
g. Kahana 11
h. Kahana 11
i. Kahana 1
j. Kahana 1
$S_{\eta,\eta}$ [m^2/Hz]
Frequency [Hz]

Figure 4.7 PSD of sea level model simulations and observations from the Kahana array.

Left side: S2 event, and right side: N4 event, (runs # 6.1 & 7.1, table 4.1). Spectra of two hours of sea level data at the time of the events are shown in the black curves from the pressure gauges. Spectra generated using model output are shown in the blue curves. The 95% confidence interval for each independent spectral estimate is plotted in red. Every other point plotted is independent due to the 50% overlap of frequency band averaging intervals.

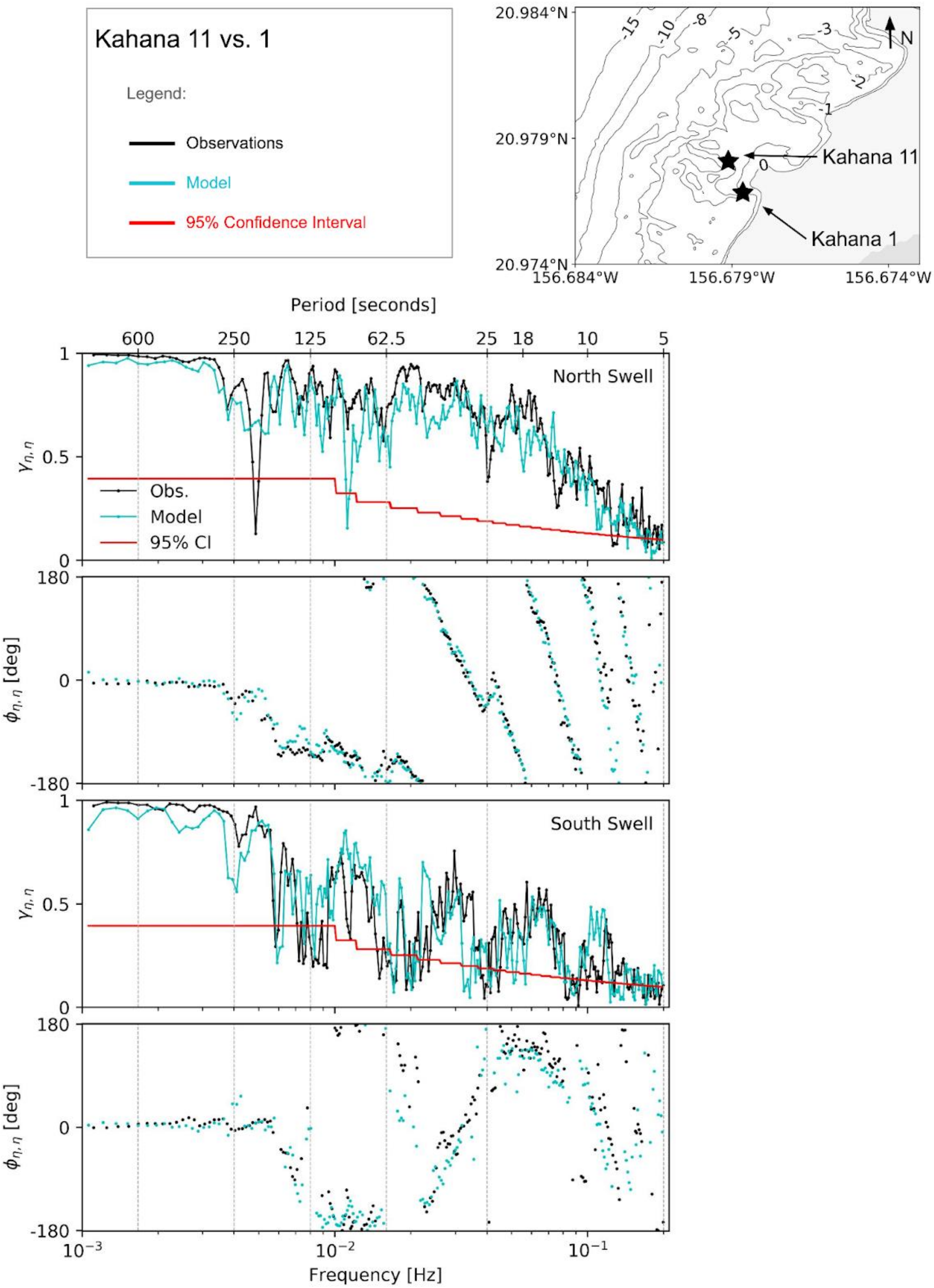

Kahana 11 vs. 1
Legend:
Observations
Model
95% Confidence Interval
20.984°N
20.979°N
20.974°N
156.684°W
156.679°W
156.674°W
N
-15
-10
-8
-5
-3
-2
-1
0
Kahana 11
Kahana 1
Period [seconds]
600
250
125
62.5
25
18
10
5
North Swell
Obs.
Model
95% CI
South Swell
$\gamma_{\eta,\eta}$
$\phi_{\eta,\eta}$ [deg]
Frequency [Hz]

Figure 4.8 Coherence amplitude and phase of sea level model simulations and observations generated using five two-hour long segments of data from Kahana 11 and Kahana 1.

Top two panels: N4 event, (runs # 6.1-6.5, table 4.1). Bottom two panels: S2 event, (runs # 7.1-7.5, table 4.1). The 95% level of no confidence for the coherence amplitude is plotted in red. Positive values of the coherence phase indicate propagation from south to north, with the first station leading the second.

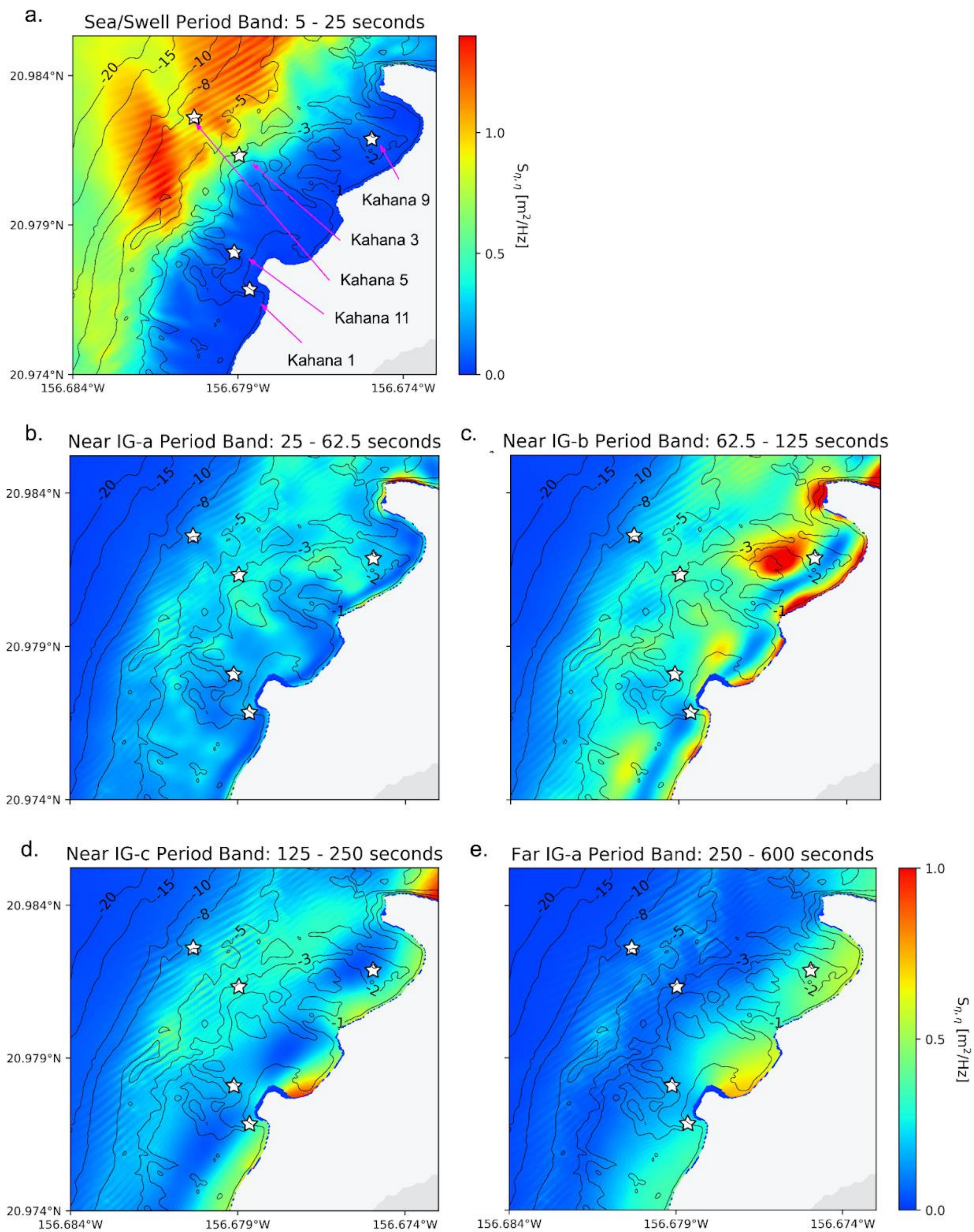
a.
Sea/Swell Period Band: 5 - 25 seconds
Kahana 9
Kahana 3
Kahana 5
Kahana 11
Kahana 1
b.
Near IG-a Period Band: 25 - 62.5 seconds
c.
Near IG-b Period Band: 62.5 - 125 seconds
d.
Near IG-c Period Band: 125 - 250 seconds
e.
Far IG-a Period Band: 250 - 600 seconds
20.984°N
20.979°N
20.974°N
156.684°W
156.679°W
156.674°W
$S_{\eta,\eta}$ [m^2/Hz]

Figure 4.9 Kahana array showing band averaged PSD generated using model output.

N4 event (run # 7.1, table 4.1). Panels show (a) the Sea/Swell period band (5 - 25 seconds), (b) the Near IG-A period band (25 - 62.5 seconds), (c) the Near IG-B period band (62.5 - 125 seconds), (d) the Near IG-C period band (125 - 250 seconds), and (e) the Far IG-A period band (250 - 600 seconds). Black contour lines show depths in meters. The white stars indicate the location of pressure gauge deployments at Kahana 5, Kahana 3, Kahana 9, Kahana 11, and Kahana 1.

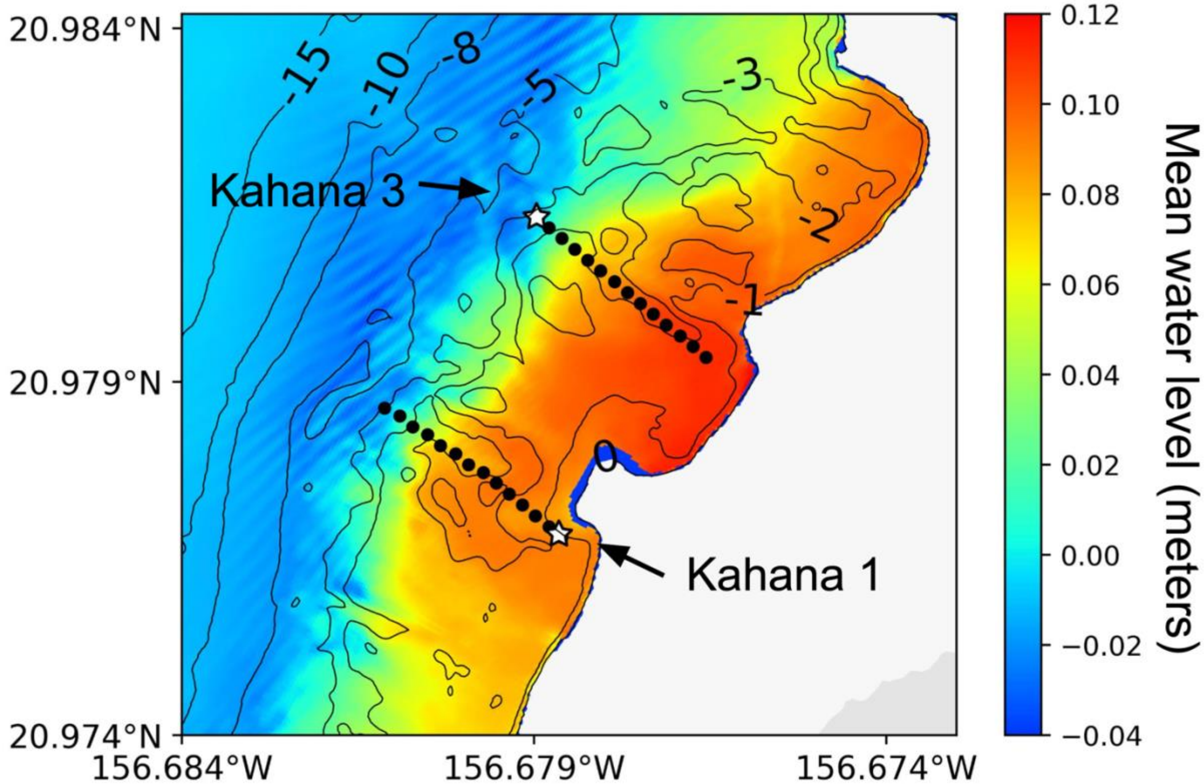

Figure 4.10 Spatial distribution of modeled mean water level (meters) for the N4 event (run # 7.1, table 4.1).

The white stars are the locations of the pressure sensors Kahana 3 and Kahana 1. The model output is taken from virtual gauges marked by the dots and at the location of the pressure sensors and presented in Fig. 4.11.

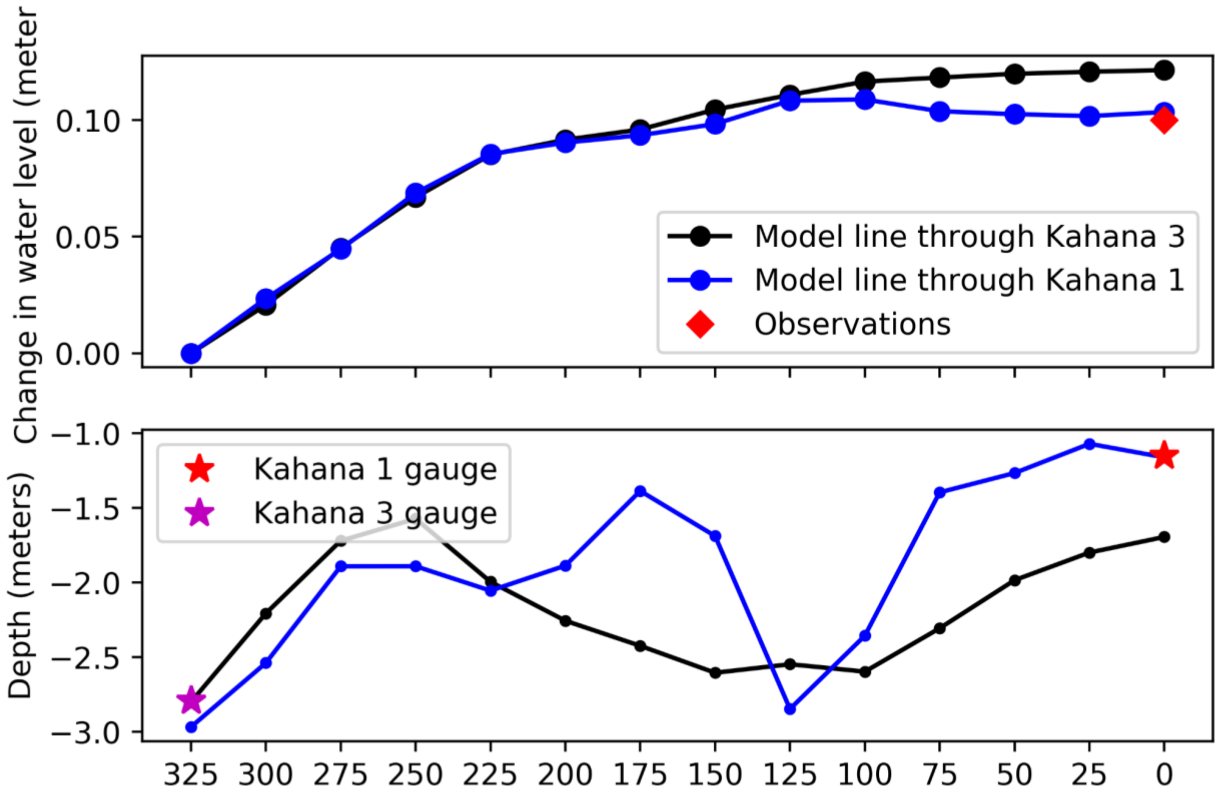

Figure 4.11 Modeled and observed wave driven change in water level for two cross shore lines of the Kahana array.

The abscissa shows distance from the nearshore gauge in meters.

Top panel: the black dots are the modeled change in water level, which is the difference between the nearshore virtual gauge and each point along the model line through Kahana 3. The blue dots are the modeled change in water level, which is the difference between the nearshore virtual gauge and each point along the model line through Kahana 1 (Fig.4.10). The observed change in water level at Kahana 1 is marked by the red diamond and is calculated as the difference in water level between Kahana 1 and Kahana 3, with the assumption the set-down at Kahana 3 is small (following Vetter et al., 2010).

Bottom panel: shows the bathymetry depth profile along the two cross shore lines in the model with the locations of the sensors marked by the stars.

Observations and model show Kahana 1 is located in the area of high setup. The model shows the setup is variable along shore (see also Fig. 4.10). The differences in setup are likely due to the high variability of the bathymetry. The setup of the observations should be calculated with observations from sensors located along the same cross shore line. This is possible for a future model simulation of a different swell event during which a cross shore array was deployed at Kahana (D1 deployments, Table 2.1).

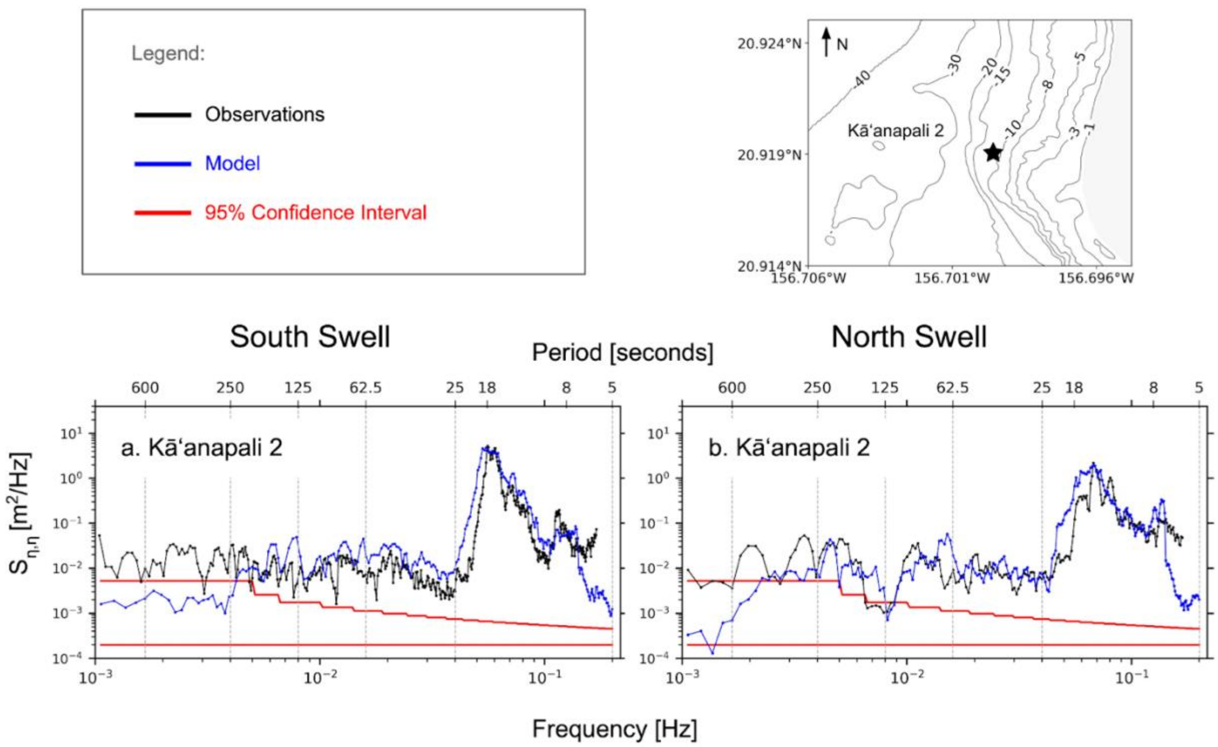

Figure 4.12 PSD of sea level model simulations and observations from Kāʻanapali.

(a) the S2 event, and (b) the N4 event (runs # 6.1 & 7.1, table 4.1). Spectra of two hours of sea level data are shown in the black curves. Spectra generated using model output are shown in the blue curves. The 95% confidence interval for each independent spectral estimate is plotted in red. Every other point plotted is independent due to the 50% overlap of frequency band averaging intervals.

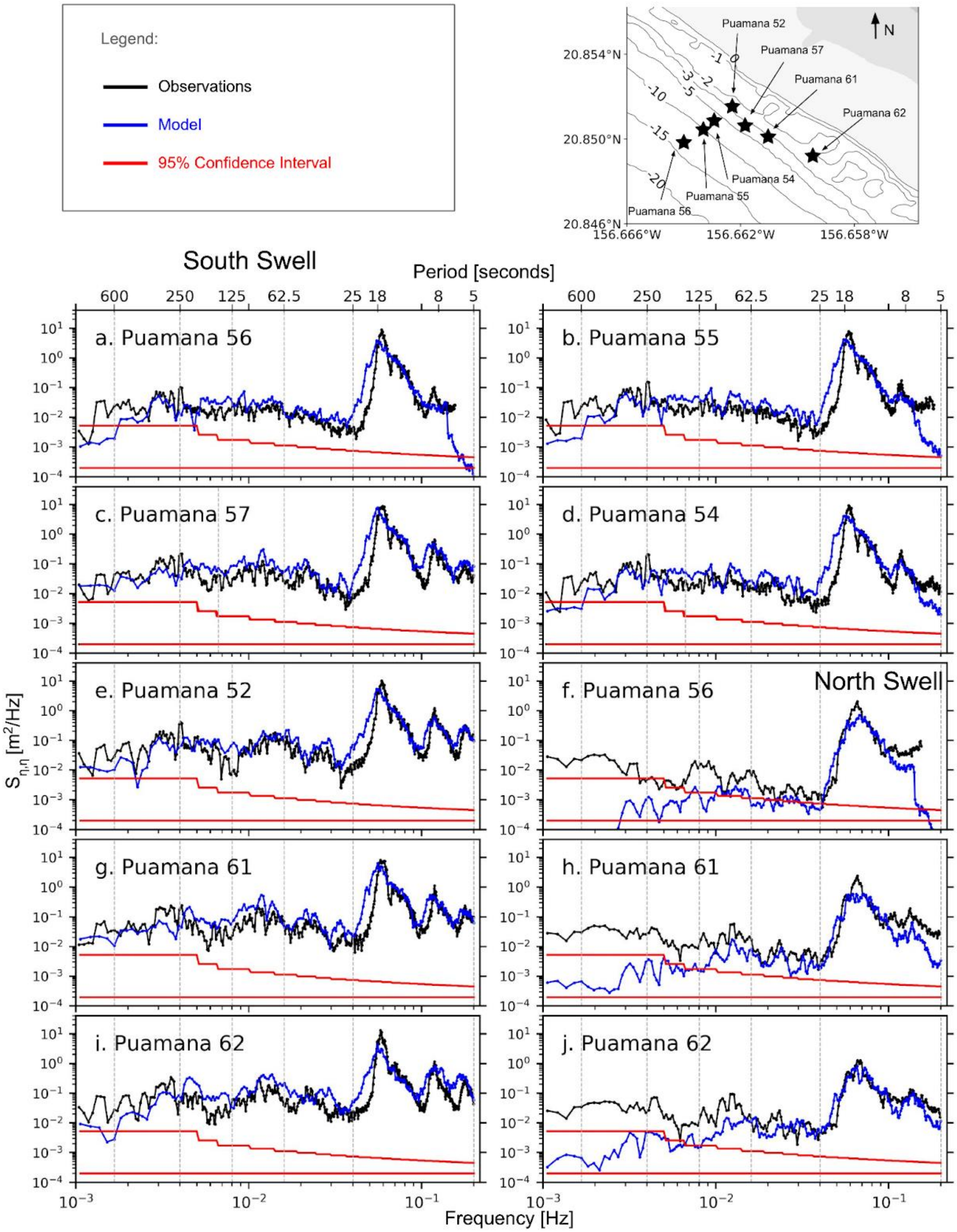
Legend:
Observations
Model
95% Confidence Interval
Puamana 52
Puamana 57
Puamana 61
Puamana 62
Puamana 54
Puamana 55
Puamana 56
N
20.854°N
20.850°N
20.846°N
156.666°W
156.662°W
156.658°W
South Swell
North Swell
Period [seconds]
Frequency [Hz]
$S_{\eta,\eta}$ [m^2/Hz]
a. Puamana 56
b. Puamana 55
c. Puamana 57
d. Puamana 54
e. Puamana 52
f. Puamana 56
g. Puamana 61
h. Puamana 61
i. Puamana 62
j. Puamana 62

Figure 4.13 PSD of sea level model simulations and observations from the Puamana array.

S2 event (panels a, b, c, d, e, f, g and i) and the N4 (panels f, h and j)) (runs # 6.1 & 7.1, table 4.1). Spectra of two hours of sea level data at the time of the events are shown in the black curves. Spectra generated using model output are shown in the blue curves. The 95% confidence interval for each independent spectral estimate is plotted in red. Every other point plotted is independent due to the 50% overlap of frequency band averaging intervals.

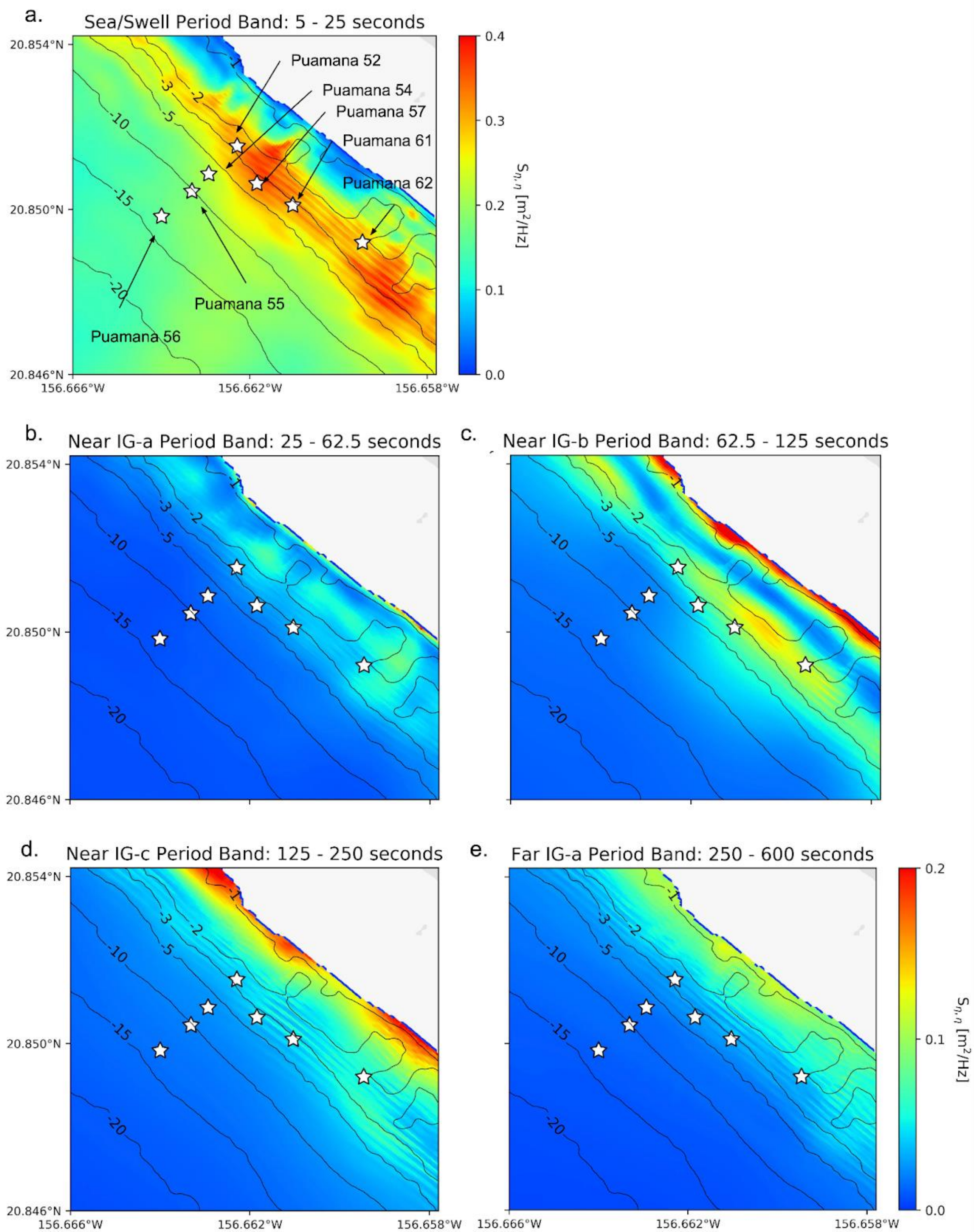
a.
Sea/Swell Period Band: 5 - 25 seconds
Puamana 52
Puamana 54
Puamana 57
Puamana 61
Puamana 62
Puamana 55
Puamana 56
20.854°N
20.850°N
20.846°N
156.666°W
156.662°W
156.658°W
$S_{\eta,\eta}$ [m^2/Hz]
b.
Near IG-a Period Band: 25 - 62.5 seconds
c.
Near IG-b Period Band: 62.5 - 125 seconds
d.
Near IG-c Period Band: 125 - 250 seconds
e.
Far IG-a Period Band: 250 - 600 seconds

Figure 4.14 Puamana array showing band averaged PSD generated using model output.

S2 event (run # 6.1, table 4.1). Panels show (a) the SS period band (5 - 25 seconds), (b) the Near IG-A period band (25 - 62.5 seconds), (c) the Near IG-B period band (62.5 - 125 seconds), (d) the Near IG-C period band (125 - 250 seconds), and (e) the Far IG-A period band (250 - 600 seconds). Black contour lines show depths in meters. The white stars indicate the locations of pressure gauge deployments.

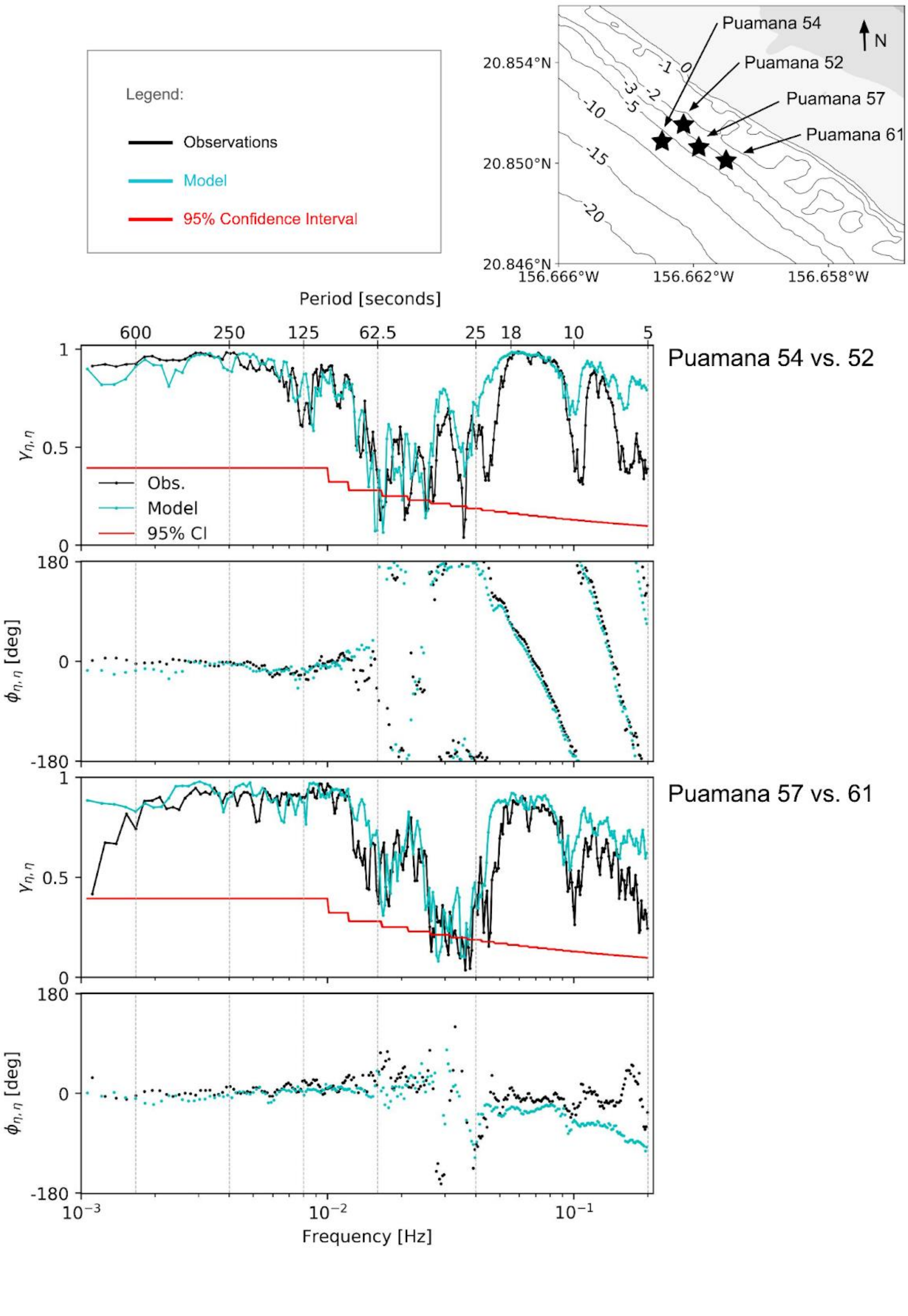

Legend:
Observations
Model
95% Confidence Interval
Puamana 54
Puamana 52
Puamana 57
Puamana 61
N
20.854°N
20.850°N
20.846°N
156.666°W
156.662°W
156.658°W
Period [seconds]
Puamana 54 vs. 52
Puamana 57 vs. 61
Obs.
Model
95% CI
Frequency [Hz]

Figure 4.15 Coherence amplitude and phase of sea level model simulations and observations generated using five two-hour long segments of data for the Puamana array.

S2 event (runs # 6.1-6.5, table 4.1). Top two panels: Sites Puamana 54 and Puamana 52 are separated by a distance of 100 meters. Bottom two panels: Sites Puamana 61 and Puamana 62 are separated by a distance of 140 meters. The 95% level of no confidence for the coherence amplitude is plotted in red. Positive values of the coherence phase indicate propagation from north to south, with the first station leading the second.

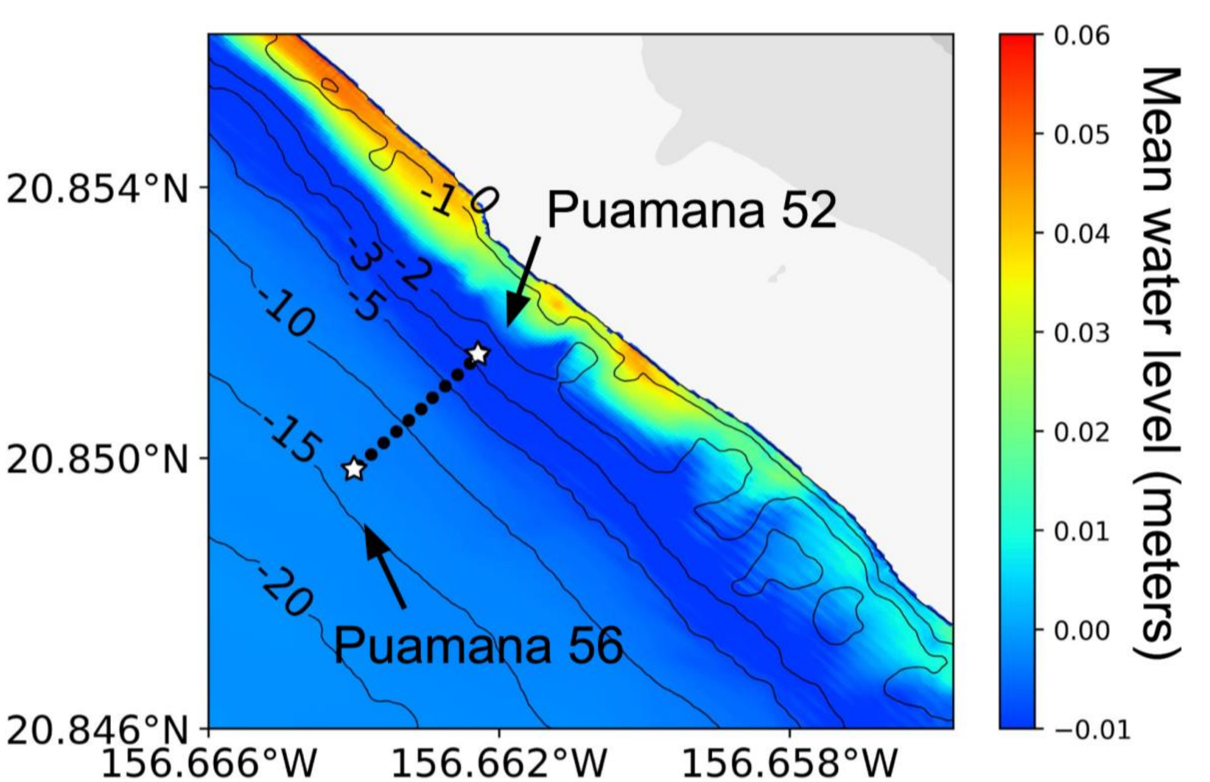

Figure 4.16 Spatial distribution of modeled mean water level (meters) for the S2 event (run # 6.1, table 4.1).

The white stars are the locations of the pressure sensors at Puamana 56 and Puamana 52. The model output is taken from virtual gauges marked by the dots and at the location of the pressure sensors and presented in Fig. 4.17.

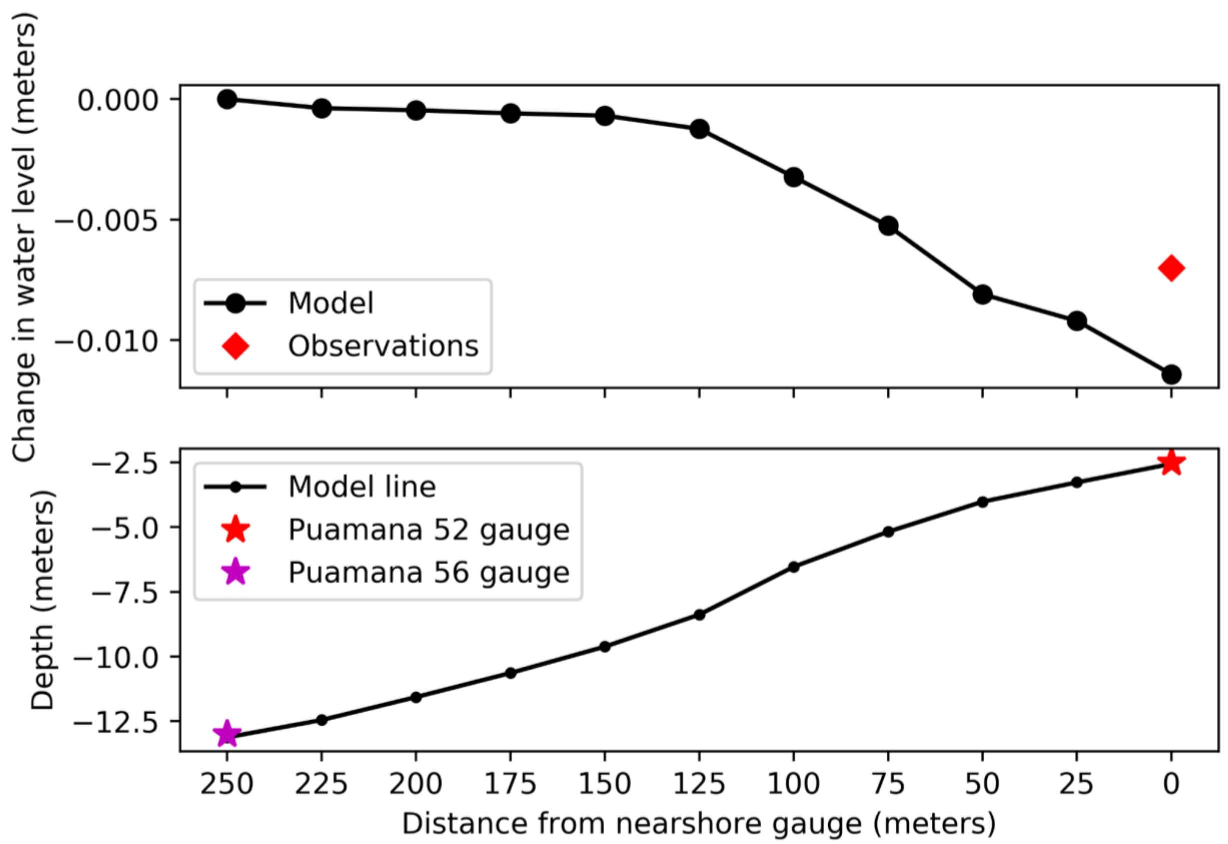

Figure 4.17 Modeled and observed wave driven change in water level for a cross shore line of the Puamana array.

The abscissa shows distance from the location of the Puamana 52 sensor in meters.

Top panel: the black dots are the modeled change in water level, which is the difference between the nearshore virtual gauge at Puamana 52 and each point along the model line through the location of the Puamana 56 (Fig.4.16). The observed change in water level at Puamana 52 is marked by the red diamond and is calculated as the difference in water level between Puamana 52 and Puamana 56, with the assumption the set-down at Puamana 56 is small.

Bottom panel: shows the bathymetry depth profile along a cross shore line in the model connecting the locations of the sensors which are marked by the stars.

Observations and model both show Puamana 52 is located where the mean water level is lower than further offshore at Puamana 56. This indicates Puamana 52 is located where the water level is set-down, which corresponds to where the waves are shoaling (for example Vetter et al., 2010).

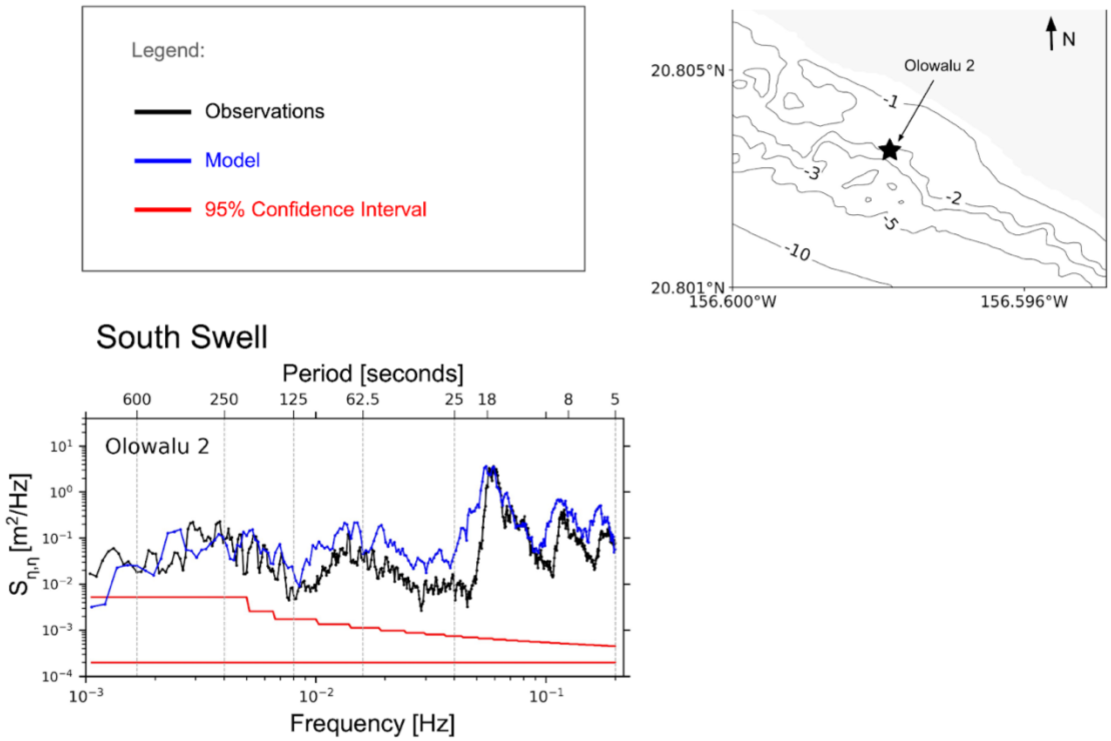

Figure 4.18 PSD of sea level model simulations and observations from Olowalu.

S2 event (run # 6.1, Table 4.1). Spectra of two hours of sea level data are shown in the black curves. Spectra generated using model output is shown in the blue curve. The 95% confidence interval for each independent spectral estimate is plotted in red. Every other point plotted is independent due to the 50% overlap of frequency band averaging intervals.

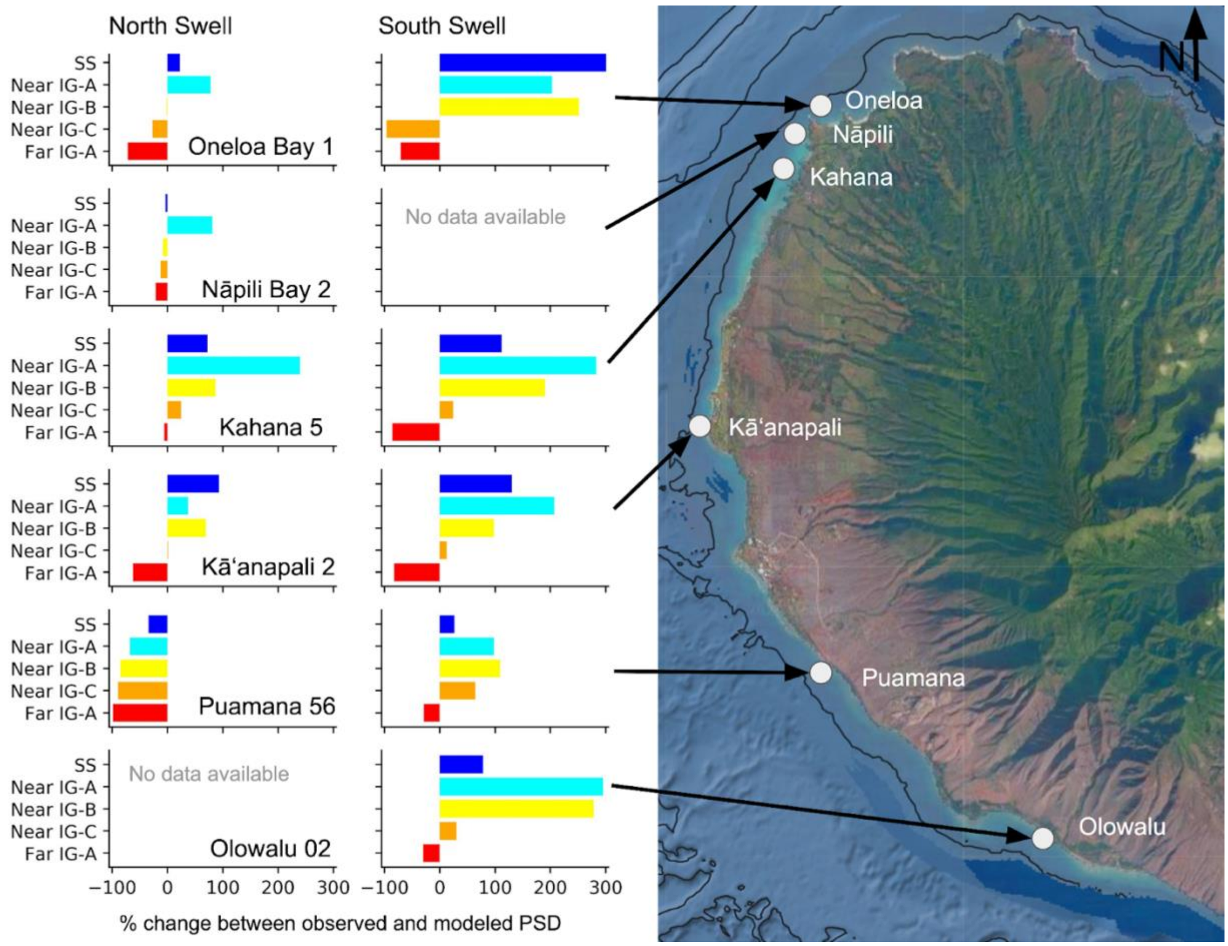

Figure 4.19 Percent difference between observed and modeled PSD at different locations in WM. Left side: N4 event and right side: S2 event. The colors are blue for the Sea/Swell period band (5 - 25 seconds), cyan for the Near IG-A period band (25 - 62.5 seconds), yellow for the Near IG-B period band (62.5 - 125 seconds), orange for the Near IG-C period band (125 - 250 seconds), and red for the Far IG-A period band (250 - 600 seconds).

References

Azouri, A. (2016). Observations, Forecast, and Modeling of 0.5-200 Min Infragravity Oscillations in Hale'iwa Harbor Region, Hawai'i. PhD thesis, Honolulu, University of Hawaiʻi at Mānoa.

Azouri, A., Luther, D., & Roeber, V. (2018). Observations and modeling of coastal infragravity waves. Department of Oceanography Seminar, University of Hawaiʻiat Mānoa

Azouri, A., Roeber, V., Luther, D., Guiles, M., Iwamoto, M., Owens, T., Merrifield, M., and Becker, J. Comparison of three phase-resolving models simulating nearshore gravity wave transformations. *Manuscript in preparation*.

Battjes, J. A., Bakkenes, H. J., Janssen, T. T., & van Dongeren, A. R. (2004). Shoaling of subharmonic gravity waves. *Journal of Geophysical Research: Oceans*, *109*(C2).

Becker, J. M., Merrifield, M. A., & Ford, M. (2014). Water level effects on breaking wave setup for Pacific Island fringing reefs. *Journal of Geophysical Research: Oceans*, *119*(2), 914-932.

Beetham, E., & Kench, P. S. (2018). Predicting wave overtopping thresholds on coral reef-island shorelines with future sea-level rise. *Nature communications*, *9*(1), 3997.

Bertin, X., de Bakker, A., Van Dongeren, A., Coco, G., André, G., Ardhuin, F., ... & Tissier, M. (2018). Infragravity waves: From driving mechanisms to impacts. *Earth-Science Reviews*, *177*, 774-799.

Booij, N., Ris, R.C. , and Holthuijsen, L.H. (1999). A third-generation wave model for coastal regions: 1. Model description and validation. *Journal of Geophysical Research: Oceans*, 104(C4), 7649-7666.

Bretschneider, C. L., Krock, H., Nakazaki, E., and Casciano, F. (1986). Roughness of typical Hawaiian terrain for tsunami run-up calculations: A user's manual, JKK Look Laboratory Report, University of Hawaii, Honolulu.

Bruch, W., Cordier, E., Floc'h, F., & Pearson, S. G. (2022). Water level modulation of wave transformation, setup and runup over La Saline fringing reef. *Journal of Geophysical Research: Oceans*, *127*(7), e2022JC018570.

Cheriton, O. M., Storlazzi, C. D., & Rosenberger, K. J. (2016). Observations of wave transformation over a fringing coral reef and the importance of low-frequency waves and offshore water levels to runup, overwash, and coastal flooding. *Journal of Geophysical*

Research: Oceans, *121*(5), 3121-3140

Cheung, K. F., Bai Y., and Yamazaki Y., 2013: Surges around the Hawaiian Islands from the 2011 Tohoku tsunami. *Journal of Geophysical Research: Oceans*, 118 (10), 5703-5719.

Coastal Engineering Manual (2002). Washington, D.C.: U.S. Army Corps of Engineers.

Elgar, S., Herbers, T. H. C., Okihiro, M., Oltman-Shay, J., & Guza, R. T. (1992). Observations of infragravity waves. *Journal of Geophysical Research: Oceans*, *97*(C10), 15573-15577.

Environmental Modeling Center (2003). The GFS Atmospheric Model. NOAA/ NCEP/ Environmental Modeling Center Office Note 442, 14 pp.

Fiedler, J. W., Young, A. P., Ludka, B. C., O'Reilly, W. C., Henderson, C., Merrifield, M. A., & Guza, R. T. (2020). Predicting site-specific storm wave run-up. *Natural Hazards*, *104*(1), 493-517.

Guiles M, Azouri A, Roeber V, Iwamoto MM, Langenberger F., and Luther D.S. (2019). Forecasts of Wave-Induced Coastal Hazards in the United States Pacific Islands: Past, Present, and the Future. *Front. Mar. Sci*. 6:170.

Guza, R. T., & Thornton, E. B. (1981). Wave set-up on a natural beach. *Journal of Geophysical Research: Oceans*, *86*(C5), 4133-4137.

Guza, R.T., Thornton, E.B., 1982. Swash oscillations on a natural beach. *J. Geophys. Res*.87, 483–491.

Guza, R.T., Thornton, E.B., 1985. Observations of surf beat. *J. Geophys. Res*. 87, 483–491.

Harris, C.R., Millman, K.J., van der Walt, S.J. et al. (2020). Array programming with NumPy. *Nature* 585, 357–362.

Hawaiʻi Ocean Time-series HOT-DOGS application; University of Hawai'i at Mānoa. National Science Foundation Award # 1756517. https://hahana.soest.hawaii.edu/hot/hot-dogs/interface.html

Hunter, J. D., "Matplotlib: A 2D Graphics Environment", Computing in Science & Engineering, vol. 9, no. 3, pp. 90-95, 2007.

Kench, P. S., Beetham, E. P., Turner, T., Morgan, K. M., Owen, S. D., & McLean, R. (2022). Sustained coral reef growth in the critical wave dissipation zone of a Maldivian atoll. *Communications Earth & Environment*, *3*(1), 1-12.

Longuet-Higgins, M. S., & Stewart, R. (1962). Radiation stress and mass transport in gravity waves, with application to surf beats, *Journal of Fluid Mechanics*, 13(04), 481– 504.

Merrifield, M.A., J.M. Becker, M. Ford, and Y. Yao (2014). Observations and estimates of wave-driven water level extremes at the Marshall Islands. *Geophysical Research Letters*, 41(20), 7245-7253.

Munk, W. (1949). Surf beats, Transactions, *American Geophysical Union*, 30, 849–854.

NOAA Tides and Currents, Kahului Harbor, HI; https://tidesandcurrents.noaa.gov/waterlevels.html?id=1615680

Nwogu, O. (1993). Alternative form of Boussinesq equations for nearshore wave propagation. *Journal of waterway, port, coastal, and ocean engineering*, 119(6), 618–638.

OCM Partners, 2022: 2013 USACE NCMP Topobathy Lidar: Maui (HI). https://www.fisheries.noaa.gov/inport/item/49751.

Okihiro, M., Guza, R. T., & Seymour, R. J. (1992). Bound infragravity waves. *Journal of Geophysical Research: Oceans*, *97*(C7), 11453-11469.

Oltman-Shay, J., & Guza, R. (1987). Infragravity edge wave observations on two California beaches, *Journal of Physical Oceanography*, 17(5), 644–663.

Péquignet, A. C. N., Becker, J. M., Merrifield M. A., & Aucan, J. (2009). Forcing of resonant modes on a fringing reef during tropical storm Man-Yi, *Geophys. Res. Lett*., 36, L03607, doi:10.1029/2008GL036259.

Pomeroy, A., Lowe, R., Symonds, G., Van Dongeren, A., & Moore, C. (2012). The dynamics of infragravity wave transformation over a fringing reef. *Journal of Geophysical Research: Oceans, 117*(C11).

RBR Instrument Guide (2022). https://rbr-global.com/wp-content/uploads/2021/12/0008814revA-Compact-Loggers-Instrument-Guide.pdf

Roeber, V., & Cheung K.F. (2012). Boussinesq-type model for energetic breaking waves in fringing reef environments. *Coastal Engineering*, 70, 1-20. https://doi.org/10.1016/j.coastaleng.2012.06.001.

Roeber, V., & Bricker, J. D. (2015) Destructive tsunami-like wave generated by surf beat over a coral reef during Typhoon Haiyan. *Nature communications*, *6*(1), 1-9.

Roeber, V., J. Pinault, Morichon, D., Abadie, S., Azouri, A., Guiles; Luther, D., Delpey, M., Danglade, N. (2019). Improving Wave Run-up Forecasts – Benefits from Phase-resolving Models. In: Goseberg, Nils; Schlurmann, Torsten (Hg.): Coastal Structures 2019. Karlsruhe: Bundesanstalt für Wasserbau. S. 752-761.

Roeber, V., Azouri, A, Guiles, M., Tognacchini, C., Luther, D. West Maui Run-up Forecast. Phase II, Part I: Model set-up, Testing, and Validation. Technical Report, *in preparation.*

Sheremet, A., Guza, R. T., Elgar, S., & Herbers, T. H. C. (2002). Observations of nearshore infragravity waves: Seaward and shoreward propagating components. *Journal of Geophysical Research: Oceans*, *107*(C8), 10-1.

Skamarock, W. C., Klemp, J. B., Dudhia, J., Gill, D. O., Liu, Z., Berner, J., ... & Huang, X. Y. (2019). A description of the advanced research WRF model version 4. *National Center for Atmospheric Research: Boulder, CO, USA*, *145*(145), 550.

Stockdon, H. F., Holman, R. A., Howd, P. A., & Sallenger Jr, A. H. (2006). Empirical parameterization of setup, swash, and runup. *Coastal engineering*, *53*(7), 573-588.

Storlazzi, C. D., Gingerich, S. B., Van Dongeren, A. P., Cheriton, O. M., Swarzenski, P. W., Quataert, E., ... & McCall, R. (2018). Most atolls will be uninhabitable by the mid-21st century because of sea-level rise exacerbating wave-driven flooding. *Science Advances*, *4*(4), eaap9741.

Thompson, R. O. (1979). Coherence significance levels, *Journal of the Atmospheric Sciences*, 36(10), 2020–2021.

Thomson, R. E., & Emery, W. J. (2014). Data analysis methods in physical oceanography, Newnes.

Tolman, H.L. (2014). User manual and system documentation of WAVEWATCH III TM version 4.18. Technical note, MMAB Contribution, 316, 311 pp.

Tucker, M. (1950). Surf beats: sea waves of 1 to 5 min. period, Proceedings of the Royal Society of London. Series A. Mathematical and Physical Sciences, 202 (1071), 565–573.

Vetter, O., Becker, J. M., Merrifield, M. A., Pequignet, A. C., Aucan, J., Boc, S. J., & Pollock, C. E. (2010). Wave setup over a Pacific Island fringing reef. *Journal of Geophysical Research: Oceans*, *115*(C12).

Virtanen, P., R. Gommers, T. E. Oliphant, M. Haberland, T. Reddy, D.Cournapeau, ... P. van Mulbregt, and SciPy 1.0 Contributors. (2020). SciPy 1.0: Fundamental Algorithms for Scientific Computing in Python. *Nature Methods*, 17(3), 261-272.